Studies of Cryogenic Electron Plasmas in Magnetic Mirror Fields

by

Ramesh Gopalan

A.B. (University of California at Berkeley) 1991
M.A. (University of California at Berkeley) 1994

A dissertation submitted in partial satisfaction of the
requirements for the degree of
Doctor of Philosophy

in

Physics

in the

GRADUATE DIVISION
of the
UNIVERSITY of CALIFORNIA at BERKELEY

Committee in charge:

Professor Joel Fajans, Chair
Professor Robert P. Lin
Professor Michael Lieberman

1998

The dissertation of Ramesh Gopalan is approved:

Chair Date

Date

Date

University of California at Berkeley

1998

Studies of Cryogenic Electron Plasmas in Magnetic Mirror Fields

Abstract

Studies of Cryogenic Electron Plasmas in Magnetic Mirror Fields

by

Ramesh Gopalan
Doctor of Philosophy in Physics

University of California at Berkeley

Professor Joel Fajans, Chair

This thesis considers the properties of pure electron plasmas in Penning traps which have an axially varying magnetic field. Our theory of the thermal equilibrium of such plasmas in magnetic mirror fields indicates that their behavior may be characterized by the ratio of their temperature to their central density T/n. For cold, dense plasmas the density along the plasma axis scales linearly with the magnetic field, while for hot, tenuous plasmas, at the opposite limit of the parameter range, the density is constant along the axis, similar to the behavior of a neutral plasma in a magnetic mirror. We are able to conclude from this that the electrostatic potential varies along the field lines, in equilibrium. As the plasma charge and potential distribution must be consistent with the grounded potential on the trap walls, the plasma profile does not follow the geometry of the magnetic field lines; the plasma radius in the high-field region is smaller than would be obtained by mapping the field lines from the radial edge of the low-field region. Another interesting feature of these mirror equilibria is that there are trapped populations of particles *both* in the low-field and high-field regions.

Our experiments on the Cryogenic Electron Trap have confirmed many of these theoretical results over a wide parameter range. We have been able to sample the volume charge density at various points on the axis. We have also measured the line-charge distribution of the plasma. Both these experiments are in general agreement with our theory of the global thermal equilibrium in the mirror-field.

A surprising observation has been the unexpectedly long-life of the $m = 1$ diocotron mode in these traps where the magnetic field varies by $\sim$ 100% across its length. We report these observations, along with plausible explanations for them.

The trap we have constructed is intended for the eventual study of very cold electron plasmas in strong magnetic fields, where the plasma electrons are expected to be in the lowest quantized cyclotron orbits - the Landau levels. In such plasmas the interaction energy of the intrinsic spin-magnetic moment of the electron with the magnetic field becomes comparable with the energy in the Landau levels, suggesting that spin-dependent effects may become noticeable in such plasmas. We have constructed an experiment to observe such effects. Along with the Cryogenic Trap, which can cool electrons down to cryogenic temperatures, this apparatus includes a polarization detection apparatus, and a source of polarized electrons to calibrate the experiment. The physics and construction details for the Spin-Experiment are described in the Appendix.

Professor Joel Fajans
Dissertation Committee Chair

To the memory of my dear grandmother,

Kamala

Contents

List of Figures

List of Tables

Acknowledgements

Well, Ken Starr began his investigation soon after I began mine but has beat me to it by handing in a report earlier. He, of course, had people secretly gathering data for him throughout; it was hard enough for me to do it in the open! My thesis may have far fewer readers but it has also cost much less. And since it is only intended to graduate, not incriminate, I need not prolong it further with missionary zeal!

I am glad to acknowledge many who have helped this thesis reach completion: My advisor, Joel Fajans, of course,whose help has been critical to the work presented here; I also wish to mention some present and former members of the Fajans group: Tony Peurrung, whose enthusiasm for non-neutral plasmas, and many other subjects besides, has been an inspiration; Charlie Hansen, with whom I have enjoyed many lively discussions, and a few games of soccer - he introduced to me to index-funds, and I think I got him hooked on to *The Economist*. Anita Reimann, Erik Gilson, Richa Govil and Katya Backhaus have also been good friends. Bret Beck of LLNL provided feedback on our (often wrong!) plasma physics ideas.

Prof. Allan Kaufman's excellent undergraduate course provided me a good grounding in basic plasma physics.

I owe a debt of gratitude to the members of the Physics Department Machine Shop - foreman George Weber has helped with many good design ideas, and has always shown me ways to improve my own. Tom Pedersen is a great guy. Marco Ambrosini, Scott Bonilla, Steve Butler, and Alex Vaynberg have shown great skill in making the insides of my Cryogenic trap. It is a tribute to Scott Bonilla's skill and dedication that the complicated construction and plumbing of the liquid helium dewar remained leak-free despite being cycled repeatedly between cryogenic temperatures and hot bakeouts. I think I have made some very good friends in the shop. They are truly a great asset for the Department.

I also thank Prof. Barry Dunning of Rice University and Dr. Greg Mulhollan of SLAC for their generous help with the Mott polarimeter, the design of the GaAs photocathode, and permission to use some of their drawings in this thesis.

Also our graduate assistant Anne Takizawa, and Rusty Orr, for help with some

of the drawings.

It is fortunate that I have been immersed in two cultures so fantastically different, yet whenever I have felt like a misunderstood stranger in a strange land, I have had many friends to lend me an ear: Lokesh Duraiappah, who has been a great friend (and my host on the memorable trip to Texas and back!) and Kedar Dave. It has been great hanging out with Steve Ashford , going sailing on the Bay, and having some great dinners over at Hudson house. An (incomplete) list of some of the people who have my time in Berkeley enjoyable : Praveen Murthy, Jyoti Iyer, Amit and Garima Lal, Rukma and Amit Marathe and Marcus Antoninus Strawn.

Frequently, a weekend home, and good South Indian food, were provided by Shekar, Nirmala, Bhaskar and Noel, in San Jose. I am also indebted to Simcha Srebnik for her companionship and support over the past few years.

I cannot sufficiently thank my parents whose patience I may have worn thin, but who have always let me think for myself.

Whatever you do may seem insignificant, but it is most important that you do it
- Mohandas Gandhi

Chapter 1

Introduction & Summary

The properties of pure non-neutral plasmas, plasmas containing only ions or electrons, not both, have been studied for over two decades in Penning-Malmberg traps. These traps have an uniform axial magnetic field for radial confinement of the charged plasma, and axial end potentials which confine it along the axis. The axial magnetic field has always been axisymmetric, since this maximizes the lifetime of the confined plasmas. However, there is no requirement that the magnetic field be axially uniform, and plasmas in traps with axially-varying fields are interesting for several reasons.

Electron plasmas can be cooled through cyclotron radiation to temperatures near that of liquid Helium. This cooling proceeds efficiently in strong trap magnetic fields. In these strong magnetic fields (greater than a Tesla), and low temperatures, we expect that the energy required to flip the electron intrinsic spin magnetic moment in the external magnetic field becomes comparable with the typical thermal energy kT. In such cold plasmas, we expect to see effects related to the electron-spin magnetic moment. In a plasma confined by a magnetic field with an axial gradient, for example, it is suggested that electrons with spin-magnetic moment aligned with the magnetic field will migrate along the field lines to the region of stronger field, while the electrons with spin-magnetic moment aligned anti-parallel to the magnetic field will tend to migrate to the opposite end.

The possibility of studying such effects has led us to describe the equilibrium of a non-neutral plasma in an axially varying magnetic field. We have discovered that this configuration has several interesting features. For cold, dense plasmas (where the plasma potential greatly exceeds the plasma temperature) the density of the plasma in its bulk scales linearly with the magnetic field strength. This is a consequence of the fact that in equilibrium the entire non-neutral plasma rotates around its axis like a rigid-rotor, at a constant angular frequency. This rotation comes about through the combination of the $E \times B$ drift and the diamagnetic drift due to the radial density gradient. We have discovered that the relative variation of the density of a plasma in a 'magnetic-mirror' field can be parametrized by the *ratio* of its temperature to its density. In cold, dense plasmas the $E \times B$ drift dominates, but as we go toward the opposite limit, of hotter plasmas, or of lower density, the diamagnetic drift dominates in the rotation and the density increase with the magnetic field is more gradual. Indeed, in the limit of hot, tenuous plasmas (where the plasma temperature is comparable to the space charge potential) the density is essentially independent of the magnetic field strength, much like the case of a neutral plasma in non-uniform magnetic field.

The density can be expected to follow a Boltzmann distribution along the field lines, so we have concluded that the density variation along the magnetic lines is produced by an equilibrium potential variation along these lines - the field lines are no longer equipotentials. This is in contrast to the neutral plasma case where there is no thermal equilibrium electric field along the magnetic field lines.

The variation of the electrostatic potential in the bulk plasma must be compatible with the boundary conditions on the grounded walls of the plasma trap. In this self-consistent description of the plasma the plasma's radial edge profile does not follow the geometry of the magnetic field lines: the radius of the plasma in the high-field region is *smaller* than would be obtained by mapping the magnetic field lines from the plasma's radial edge in the low field region.

Our theoretical description of a pure electron plasma in a magnetic mirror field reveals another interesting conclusion. Since the field lines are no longer equipotentials we have populations of trapped particles both in the low-field region and the high-field region. The low-field region trapping, of course, is similar to that of a neutral plasma in a magnetic mirror. However, the presence now of an electric field along the magnetic field lines also traps low-energy particles in the high-field region.

We have also studied such mirror equilibria of electron plasmas experimentally. We established an field gradient across the length of our trap by moving it axially to positions in the bore of a superconducting solenoid magnet where the magnetic field varied along the axis. By sampling through a pin-hole plasma charge from different points along its axis we were able to measure the density variation along the axis. These measurements were found to be in general agreement with the theoretical expectations.

We were also able to measure the line-charge density of the plasma at points along its length and these too matched the trends predicted in the theory.

The plasmas we studied included a wide range in the relevant parameter - the ratio of the temperature to the density, and we noticed that this single parameter adequately characterized the experimental plasmas.

The simplest and most commonly studied mode in pure electron plasmas is the $m = 1$ diocotron mode which is excited by the radial displacement of the plasma cylinder from the trap axis. Although this mode, due to $E \times B$ drift, is remarkably stable in traps with uniform axial B field, we have also observed similar long-lived oscillations in our trap with an axial gradient present. The details of our observations, and possible reasons for the long-life of this mode in gradient magnetic fields are described in Chapter 5.

Pure electron plasmas have been cooled at UCSD to cryogenic temperatures through cyclotron radiation. The trap we have constructed for the experiments on the mirror equilibria is enclosed by a liquid Helium dewar allowing it to be cooled to cryogenic temperatures when we need to produce cold plasmas.

At low temperatures, and strong magnetic fields, the plasmas become ‘strongly-magnetized’ - the typical distance of closest approach between colliding particles becomes larger than the Larmor radius. The most significant consequence of this is the sharp drop in the anisotropic temperature equilibration rate in these plasmas. This exponential decrease in the collisional equilibration has been observed at UCSD.

The intrinsic spin-moment of the plasma particles has been irrelevant to the study of plasmas in general, with a few exceptions. It has been suggested, for instance, that the nuclear reaction rates in fusion plasmas may be enhanced (by $\sim 50\%$) by aligning the (nuclear)spins of the colliding tritium and deuterium nuclei parallel to the confining magnetic field [7]. The electron-spin moments were not included in this analysis because they do not affect the reaction rate in these hot, quasi-neutral plasmas.

However, as mentioned earlier, effects related to the intrinsic electron-spin moment may become observable in cold electron plasmas, in strong magnetic fields. I describe some of these effects and the experiment we have set up to study them in cold plasmas confined in axially varying fields.

This thesis is organized in the following fashion. Chapter 2 describes our theory of the equilibria of non-neutral plasmas in Penning traps with axially varying fields. Chapter 3 details the considerations that went into the design and construction of the Cryogenic Electron Trap which was used for the experiments. Our experimental observations of these mirror equilibria are described in Chapter 4, along with comparisons with the theory. Chapter 5 is on the diocotron oscillations observed in the axial field gradient.

The possibilities for further research on such plasmas are covered in Chapter 6, including a description of spin-related experiments. We have set up an experiment to study the spin-polarized electron plasmas; the details on the design and construction of this experiment are given in Appendix A.

Chapter 2

Theory of Non-neutral Plasma Equilibria in Magnetic Mirrors

2.1 Introduction

The radial confinement of a pure electron plasma in a cylindrical Penning-Malmberg trap is assured to the extent that its canonical angular momentum in the axial magnetic field is conserved. The plasma's angular momentum is conserved when the electric and magnetic fields imposed on the plasma are axisymmetric [8]. While the magnetic field has to be axisymmetric to ensure long plasma lifetimes, there is no requirement on uniformity along the field axis and pure electron plasmas can be studied in traps with an arbitrary gradient along the magnetic field axis z. All practical Penning traps have some axial non-uniformity in their magnetic fields, and the properties of plasmas in traps with substantial gradients are interesting for several reasons. Many of the electron-spin dependent effects in cold electron plasmas described in Chapter 6 require a magnetic field gradient. However, the equilibria of non-neutral plasmas in magnetic mirrors, or similar axial gradients have, so far, not been described in detail. The special case of the equilibrium of a low-density electron gas with a 'loss-cone' distribution in a magnetic-mirror field was described by Davidson [9]. However, the space charge potential was assumed to be much smaller than the electron temperature, and the case of a dense plasma which is confined axially by negative potentials was not considered.

The 'rigid-rotor' Vlasov equilibrium of an electron beam propagating through a periodic axial magnetic field is treated in [10], yet this does not cover the case of a trapped plasma where the axial fluid momentum is zero.

The study of neutral plasmas in 'magnetic-mirror' field configurations is almost as old as plasma physics itself; magnetic mirror configurations have been implemented as possible routes to achieving magnetic-confinement fusion in deuterium plasmas. A 'magnetic mirror' is, of course, a cylindrically symmetric field configuration where the axial field strength is a minimum between two regions of greater strength. See Fig. 2.1. All charged particles, performing cyclotron motion in this field, have magnetic moments which point anti-parallel to the local direction of the magnetic field. Plasma ions and electrons are trapped in the low-field region to the extent that their kinetic energies parallel to the magnetic field are unable to overcome the force repelling their magnetic moments from the high-field regions at either end of the 'mirror'. The magnetic moment of each particle is, of course, proportional to the ratio of its perpendicular kinetic energy and the local magnetic field strength, and is an adiabatic invariant. The confining force on each particle is then proportional to the perpendicular kinetic energy of the particle and the local (relative) gradient in

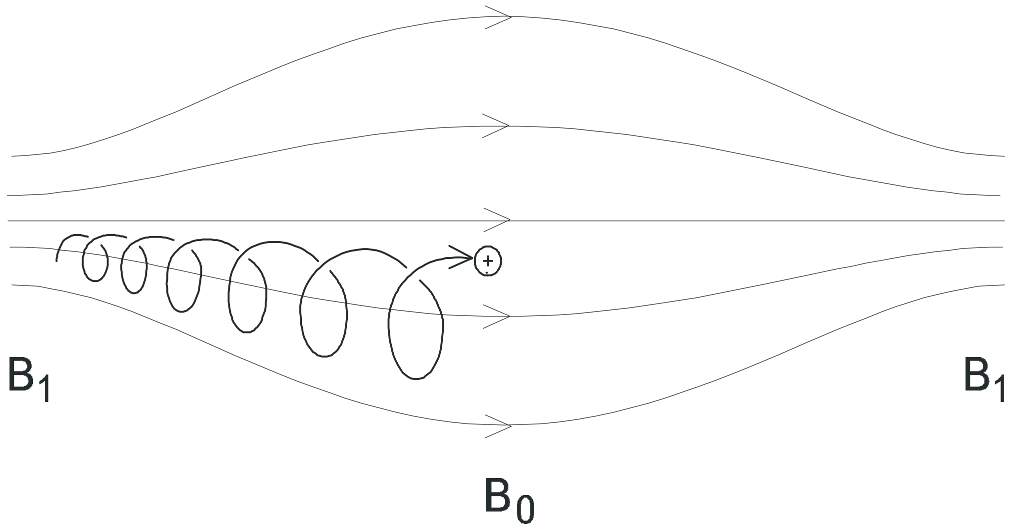

Figure 2.1: A Particle in a Magnetic Mirror

the magnetic field. Thus, particles with a combination of small perpendicular kinetic energy and large parallel kinetic energy will not be confined by this mechanism and this leads to a 'loss cone' in velocity space, whose apex angle is determined by the magnetic mirror ratio [11].

There are various methods of 'plugging' the 'loss-cone', such as by using an radiofrequency signal to pump up the perpendicular kinetic energy of the electrons to keep them to the exterior of the 'loss-cone'. When the loss of particles with large parallel kinetic energy is reduced or eliminated, the plasma in the mirror may be described by a thermal equilibrium distribution, with a Maxwellian velocity distribution everywhere in the plasma. Usually, of course, the ions and electrons have different temperatures. Yet, it is characteristic of such neutral plasmas in Boltzmann equilibrium that the density in the plasma interior is independent of the magnetic field strength; the magnetic field makes no contribution to the total energy of the particles. Also the electrostatic potential along the magnetic field lines is a constant; there are no equilibrium electric fields in a neutral plasma in a magnetic mirror.

Pure electron (and pure ion) plasmas in uniform magnetic fields have been studied through theory and experiment for over twenty years. Thermal equilibria of cylindrical electron plasmas in uniform magnetic fields have been described theoretically [12, 13] and observation of transport to global thermal equilibrium has been observed experimentally [14]. It is characteristic of the plasmas in these investigations that the electrostatic potential is constant along the magnetic field lines, in the interior of the plasma, away from the axial ends. Similarily, the density is also constant throughout the bulk of the plasma, away from the axial and radial edges.

We have considered the thermal equilibrium of a non-neutral plasma in a magnetic-mirror and have drawn some conclusions that distinguish it from the case of a neutral plasma in a magnetic mirror, and the case of a non-neutral plasma in uniform-field Penning-Malmberg trap, as described above. Since the non-neutral plasma typically has space-charge potential that exceeds its temperature, it is most often confined at the axial ends by large electrostatic potentials. This naturally eliminates the 'loss-cone', trapping all particles, regardless of their velocities.

We have found that in non-neutral plasmas where the temperature is much less than the space-charge potential, density scales linearly with the magnetic field strength. Since this means that the thermal equilibrium density varies along any magnetic field line in the bulk of the plasma, the electrostatic potential varies along the field line to make this density change possible. This situation is, of course, different from the case of the neutral plasma in a magnetic mirror, or a non-neutral plasma in a uniform-field.

As temperature is increased in the non-neutral plasma, the density increase with magnetic field becomes slower, and when the temperature becomes comparable or greater than the space charge potential of the plasma, the density is very nearly constant. Of course, this is the limit in which the plasma particles act almost independently of each other, and simulates the behavior of a neutral plasma in a varying magnetic field.

Another consequence of our theory is that the plasma's radial profile does not follow the geometry of the field lines. The plasma radius in the high-field region is smaller than would be obtained by following the magnetic field lines from the plasma's radial edge in the low-field region into the high-field.

A neutral plasma in a magnetic mirror has particles trapped in the low-field region and particles are similarily confined in the low-field region of a non-neutral plasma. An unique feature of non-neutral plasmas is that there are also trapped particles in the high-field region. I will discuss the reason and consequences of this later in the chapter.

In the following sections, I will first describe the essential features of the uniform-B field non-neutral plasma equilibrium since an understanding of this theory is essential to the treatment of the case where the field varies along the axis of the trap. Then, I will describe our theory of the equilibrium in an axially-varying field. Finally, I will elaborate on some of the predictions of this theory.

2.2 The Equilibrium in an uniform magnetic field

Prasad and O'Neil calculated thermal equilibria of pure electron plasmas in uniform magnetic fields [12] and we summarize their theory in this section.

We consider the simple case of a cylindrical electron plasma in a Penning-Malmberg

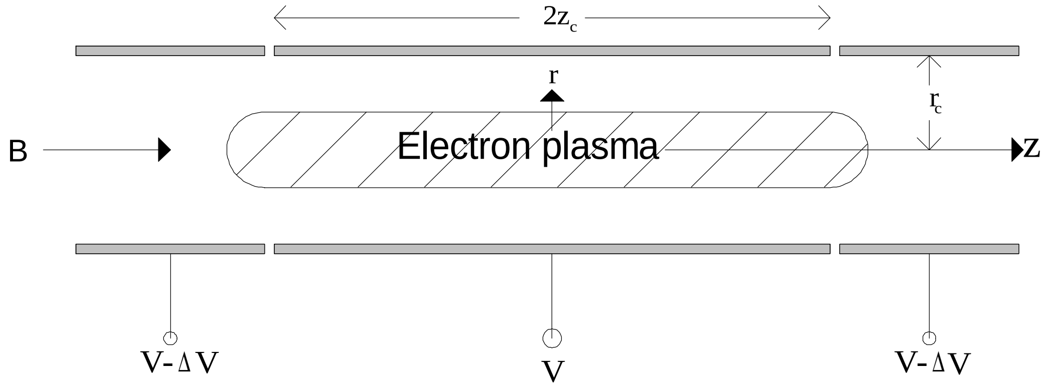

Figure 2.2: Scheme of a simple Penning trap

trap with a magnetic field along the symmetry axis z. The scheme is shown in Fig. 2.2 and the mechanism for plasma confinement is described in Chapter 3. The metal cylinders (or gates) at the ends of the plasma are biased ΔV negative relative to the central cylinder to provide axial confinement of the plasma. Since the system is time-independent and has cylindrical symmetry, the single electron Hamiltonian or energy function H and canonical angular momentum P_θ are constants of the motion, through Noether's theorem.

Any function of these constants, $f(H, P_\theta)$, is a solution of the Vlasov equation, through Jeans' theorem, and we seek self-consistent distributions f i.e. those that are consistent with the electric potential $\phi(r, z)$ described by Poisson's equation. In thermal equilibrium the conserved quantities H and P_θ must enter the distribution function on an equal footing, i.e. in linear combination [15, 16]. Therefore we choose $f(H, P_\theta) = f(H - \omega P_\theta)$, where ω has to be a constant so that the argument $H - \omega P_\theta$ is a constant of the electron motion and f is a Vlasov solution.

The electron energy is $H = \dfrac{p^2}{2m} - e\phi(r, z)$, where ϕ is the electric potential and m, $-e$, and p are the electron mass, charge, and kinetic momentum. (Notice that H does not include the magnetic field explicitly - the magnetic field does no work on the electron). The canonical angular momentum is $P_\theta = p_\theta r - (\dfrac{e}{c})A_\theta(r)r$, where $p_\theta(r)$ is the azimuthal component of the kinetic momentum and c is the speed of light. We can use $A_\theta(r) = Br/2$ for the azimuthal component of the vector potential, giving the electromagnetic contribution to the electron momentum. ω has the physical interpretation of being the azimuthal angular velocity of the electron fluid [17]. To see this, we write explicitly, with $\Omega = eB/mc$,

$$f(H - \omega P_\theta) = f\left(\frac{{p_z}^2}{2m} + \frac{{p_r}^2}{2m} + \frac{(p_\theta - m\omega r)^2}{2m} - e\phi(r,z) + \frac{m}{2}\omega(\Omega - \omega)r^2\right) \tag{2.1}$$

In the expression in parentheses on the right only the third term involves p_θ, the kinetic azimuthal momentum. The azimuthal fluid velocity is then,

$$V_\theta = \frac{\int \frac{p_\theta}{m} f(H - \omega P_\theta) d^3p}{\int f(H - \omega P_\theta) d^3p} = \omega r \tag{2.2}$$

Since the electron fluid spins around the axis at the same uniform rate, plasmas described by distributions of the form $f(H - \omega P_\theta)$ are termed 'rigid-rotor equilibria'; these plasmas have no radial shear in their rotation. Any steady-state axisymmetric plasma in thermal equilibrium can be described as such.

In global thermal equilibrium f takes the familiar Boltzmann form [12]

$$f = n_0 (\frac{m}{2\pi T})^{3/2} exp[-(\frac{1}{T})(H - \omega P_\theta)] \tag{2.3}$$

As pointed out by Davidson [17], f being a monotonically decreasing function of the argument $(H - \omega P_\theta)$ is a sufficient condition for the stability of the Vlasov solution $f(H - \omega P_\theta)$ in *any* axisymmetric field, even one with variation along the symmetry axis. Clearly, the Boltzmann form satisfies this stability condition.

By 'global thermal equilibrium' we mean that collisions have established equilibrium along and across field lines and the entire plasma is described by a single kinetic temperature T. The electron density is, of course, $n = \int f d^3p$ and the electrostatic potential is determined self-consistently through Poisson's equation,

$$\frac{1}{r}\frac{\partial}{\partial r} r \frac{\partial \phi}{\partial r} + \frac{\partial^2 \phi}{\partial z^2} = 4\pi e n = 4\pi e n_0 exp(-\frac{1}{T}[-e\phi(r,z) + \frac{m}{2}\omega(\Omega - \omega)r^2]) \tag{2.4}$$

In thermal equilibrium the two terms in the exponential balance each other to give constant density out to some radius r beyond which the last term gets large enough that the density decreases exponentially at large r. Similarily, when ϕ becomes too negative, due to the confining potentials on the end gates for example, the density drops off and the plasma is axially confined.

Poisson's equation is solved subject to boundary conditions on the cylinder of the trap and the solution depends on the parameters $n_0, T, \omega(- \quad - \omega), r_c, z_c$,and the confining potential ΔV.[Fig. 2.2]. r_c and z_c are the trap radius and axial extent. V is chosen to make $\phi(r, z)$ zero at the origin $(r, z) = (0, 0)$, so n_0 is the value of the density at the origin. As in [12] we rescale the variables,

$$\psi \equiv \frac{e\phi}{T} - \frac{m\omega(- \quad - \omega)r^2}{2T}, \rho \equiv \frac{r}{\lambda_D}, \xi \equiv \frac{z}{\lambda_D},$$
$$\lambda_D^2 \equiv \frac{T}{4\pi n_0 e^2}, \gamma \equiv \frac{2m\omega(- \quad - \omega)}{4\pi n_0 e^2} - 1, \tag{2.5}$$

and Eq. 2.4 becomes

$$\frac{1}{\rho}\frac{\partial}{\partial\rho}\rho\frac{\partial\psi}{\partial\rho} + \frac{\partial^2\psi}{\partial\xi^2} = (e^\psi - 1) - \gamma, \tag{2.6}$$

and the density is given by $n(\rho, \xi) = n_0 exp[\psi(\rho, \xi)]$. The solutions to Eq. 2.6 are uniquely determined by the parameters γ, $\frac{e\Delta V}{T}$, $\rho_c = \frac{r_c}{\lambda_D}$, and $\xi_c = \frac{z_c}{\lambda_D}$ (λ_D is, of course, the Debye length).

If we ignore axial dependence, [13, 18, 15]then for a given trap wall radius the thermal equilibrium of an infinitely long column of plasma with a given plasma temperature T and central density n_0 is completely described by the value of the parameter γ; γ may be interpreted as determining the plasma's radius, when the values of the other parameters are already prescribed. Excluding ξ dependence, Eq. 2.6 becomes

$$\frac{1}{\rho}\frac{\partial}{\partial\rho}\rho\frac{\partial\psi}{\partial\rho} = (e^\psi - 1) - \gamma \tag{2.7}$$

The boundary conditions on the solution $\psi(\rho)$ to Eq. 2.9 are $\psi(0) = 0$, since we choose $\phi = 0$ at $(r, z) = (0, 0)$, and $\psi'(0) = 0$, required by the cylindrical symmetry. The solution to Eq. 2.9 is $\psi(\rho) = \gamma[1 - I_0(\rho)]$, where I_0 is the Bessel function with imaginary argument. γ can be expressed in terms of the scaled radius of the plasma, ρ_p, defined by $\psi(\rho_p) \equiv -1$, as $\gamma = -1/[1 - I_0(\rho_p)]$ which is approximately

$(2\pi\rho_p)^{1/2}exp(-\rho_p)$, for $\rho_p = \dfrac{r_p}{\lambda_D} \gg 1$. (We define the 'radius' of the plasma to be where the density has fallen to $1/e$ of its central value).

To demonstrate the behavior of $\psi(\rho)$ we look at the case of $\rho_p \gg 1$ where γ is small and positive. (Although we will not restrict ourselves to that case, the strict definition of a non-neutral plasma is one for which the $r_p \gg \lambda_D$). For such γ, $\psi(\rho)$ remains small (and slightly negative) and essentially constant up to a large value of ρ after which it decreases sharply as $I_0(\rho)$ becomes essentially exponential. Therefore, the density $n = n_0 exp(\psi)$ remains nearly constant up to a large value of ρ after which it drops rapidly to zero, defining the radial edge of the plasma. This density dependence with scaled radius is shown in Fig. 2.3.

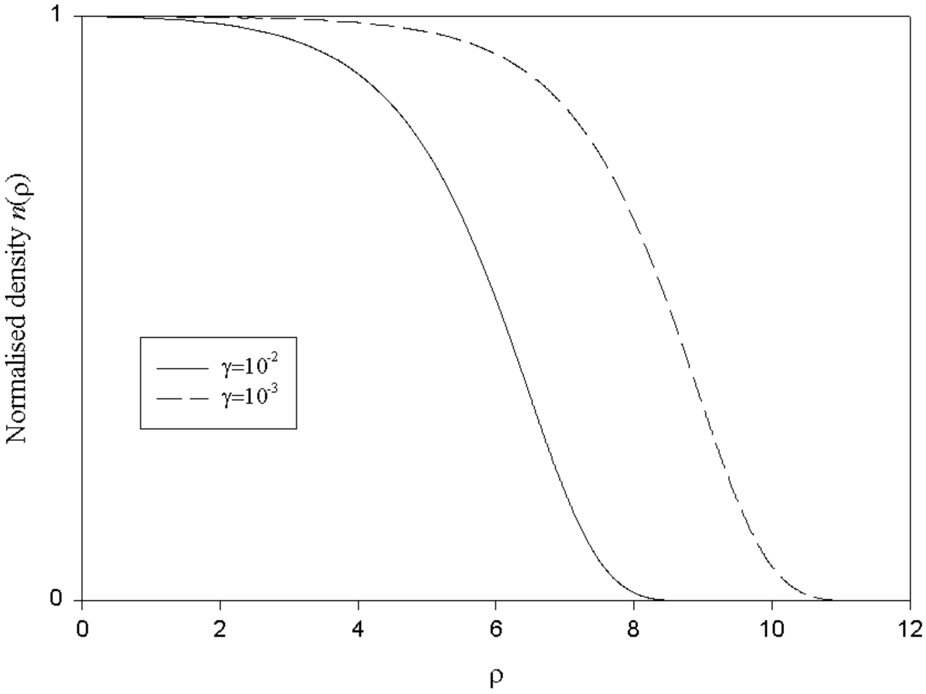

Figure 2.3: (Normalized)Density n vs. scaled radius ρ, for $\gamma = 10^{-2}$ and 10^{-3}

In the interior of the plasma, and away from the axial ends, the potential is constant along field lines and hence the exponential term in Eq. 2.4 is constant along a field line at some r; the plasma in thermal equilibrium has uniform density along the field lines, and nearly uniform density out to a radius r_p, beyond which it falls off to zero over a few Debye lengths.

At the edge of the density falloff region $\psi(\rho) \simeq -\gamma I_0(\rho)$ and as $\gamma \to 0^+$ Eq. 2.6 can be approximated as $\dfrac{d^2\psi}{d\rho^2} = exp(\psi) - 1$ (the term $\sim \dfrac{\partial\psi}{\partial\rho}$ is dropped since $\psi'(\rho) \simeq -\gamma I_0'(\rho)$ and $\gamma \ll 1$). This equation is independent of γ and unaffected by a translation in ρ. Since $I_0(\rho)$ is exponential in nature the γ dependence of ψ manifests itself only as a shift along the ρ axis. Therefore, the curves $\psi(\rho, \gamma)$ for different (yet small) values of γ are essentially the same in the falloff region and differ only by a lateral shift along ρ. This is shown in Fig. 1 of [13] and reproduced in Fig. 2.4.

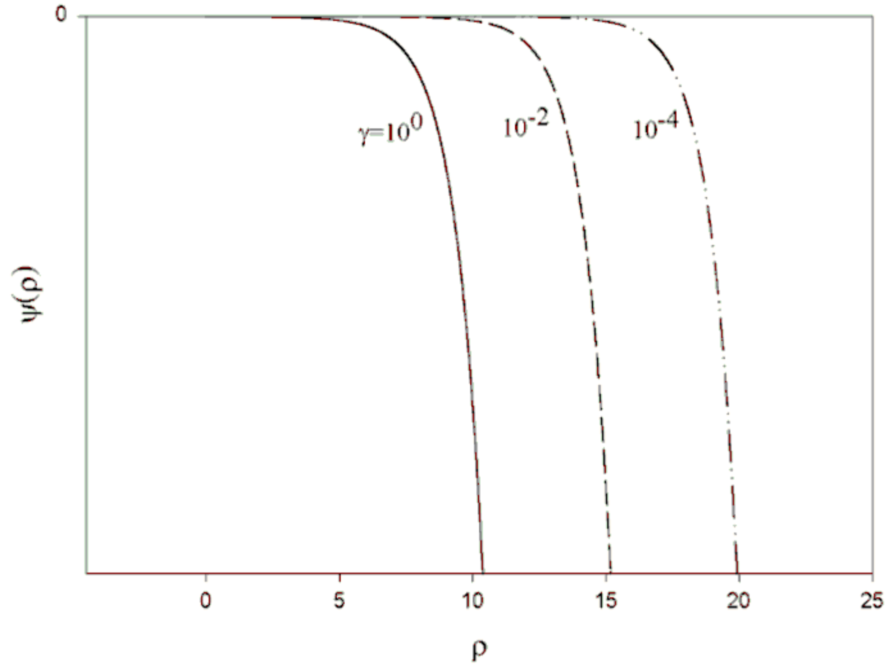

Figure 2.4: Universal nature of $\psi(\rho, \gamma)$

So, while the radius at which the falloff occurs depends on γ, the actual radial edge profile is determined only by the central density and temperature, which determine the Debye length.

We have so far described the behavior of the radial density profile for an infinitely long plasma, and this is adequate to describe the charge distribution of a finite length plasma, far away from its axial ends. We, of course, are only considering plasmas whose length is much greater than its radius.

The plasma behavior at the axial edges, at the confining end cylinders, is described in [12, 19]. Electron plasmas are described as being 'thick' or 'thin', and as being 'well- or poorly- confined'. 'Thick' plasmas have space charge potential $\phi_p \gg T$; this condition being equivalent to $r_p \gg \lambda_D$. Plasmas with $\phi_p \ll \phi_g$, the confinement gate potential, are described as 'well-confined', since the plasma does not penetrate significantly into the confinement gate. This description of the charge distribution at the axial ends of the plasma, at the confining gates, also applies in the case of an axially varying magnetic field , since the typical plasma radius is much smaller than the magnetic field scale length.

2.3 The Equilibrium in an Axially varying field

The theory in the previous section can be easily extended to treat the equilibrium with an axially varying but cylindrically symmetric magnetic field in a Penning trap. H and P_θ remain single electron constants of motion and the thermal equilibrium is still described by Eq. 2.3. We may imagine that the field consists of piece-wise uniform sections. A complication that arises with the formalism is that the axial variation of B means that there will necessarily be a slight variation of B_z with radial position at a fixed z. The Maxwell equations provide an estimate of this; $\nabla \cdot \mathbf{B} = \mathbf{0}$ implies $B_r \approx (r/2)\partial B_z/\partial z$ and $\nabla \times \mathbf{B} = \mathbf{0}$ gives $\partial B_z/\partial r = \partial B_r/\partial z$. So $\partial B_z/\partial r \approx (r/2)\partial^2 B/\partial z^2$. We may estimate the radial variation of B_z as $\delta B_z/B_z \approx (r^2/B_z)\partial^2 B_z/\partial z^2 \sim (r^2/L^2)$ or $\approx 1\%$ for a typical axial field scale length of $L \approx 10$ cm and $r \sim 1$ cm; barring the case of very steep magnetic field gradients, the radial variation of B_z may be ignored to a good approximation. To the extent this small variation is ignored we can continue to use the mathematical formalism of the uniform-B case. The azimuthal vector potential is $A_\theta = 1/r \int B_z(r', z)r'dr' \approx B_z(0, z)r/2$ and the cyclotron frequency - $\equiv eB_z(z)/mc$. We can rescale the Poisson equation[Eq. 2.4] as in Eq. 2.5. Recall that in the uniform-B case, n_0 is the density at the origin where the potential ϕ is set to zero; in this case also n_0 is the electron density at a point on the z-axis ($r = 0$) where the potential is set to be zero. We may arbitrarily choose this point to be at the low-field end of the plasma. Note that the scaling length, λ_D, in Eq. 2.5 corresponds to the density n_0 at that reference point, and is not necessarily the Debye length at other points in the plasma. Eq. 2.6 looks the same, except that now γ now varies with z (because now - $=$ - (z)).

$$\frac{1}{\rho}\frac{\partial}{\partial\rho}\rho\frac{\partial\psi}{\partial\rho}+\frac{\partial^2\psi}{\partial\xi^2}=(e^{\psi}-1)-\gamma(\xi), \tag{2.8}$$

In principle, Eq. 2.8 can be solved numerically for a varying γ. (We have to pick a value for the plasma radius r_p at a particular reference point in the plasma, such as where the density is n_0; this specifies $\gamma(z)$ at that point, and use Eq. 2.5, with - $\equiv eB_z(z)/mc$, to determine $\gamma(z)$ at other points).

It is more helpful to consider what happens in a magnetic field configuration that changes smoothly from one uniform level B_0 to an uniform higher level B_1, as depicted in Fig. 2.5. We can ignore the transition zone and assume that the equilibrium in the semi-infinite uniform field regions is of the same nature as the infinitely long uniform-B case described in section 1.2 . We then calculate how the equilibrium in one region relates to the equilibrium in the other.

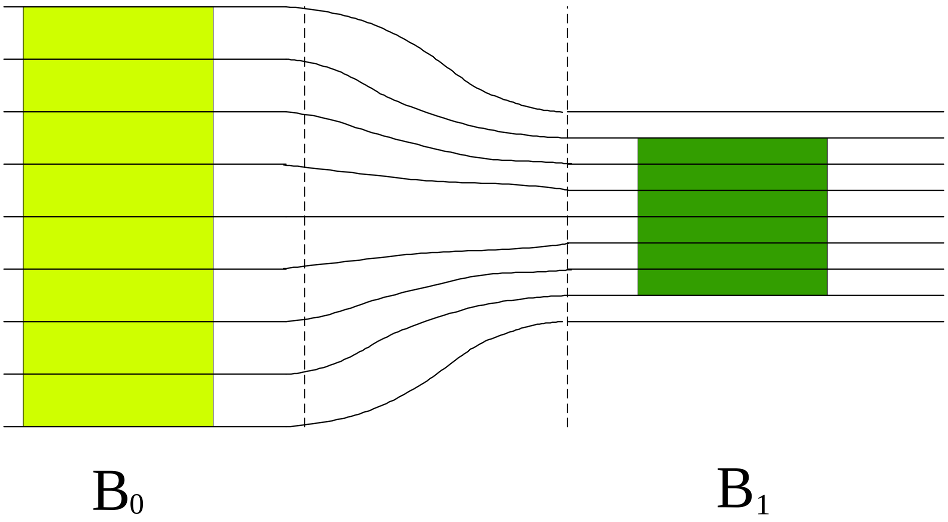

Figure 2.5: Plasma in a piece-wise uniform field

Considering the case of a piecewise-uniform field where the axial field magnitude steps quickly from one value B_0 to another higher value B_1 leads to an accurate description of a real situation with smooth, continuous variation provided that the plasma and wall radii are much smaller than the scale length of the magnetic field [19]. This condition is easily met since the scale length is typically greater than or comparable to the plasma length which, of course, is typically much greater than the plasma radius.

Recall that in a (semi-) infinite uniform field region the Eq 2.8 simplifies to

$$\frac{1}{\rho}\frac{\partial}{\partial\rho}\rho\frac{\partial\psi}{\partial\rho} = (e^{\psi} - 1) - \gamma \tag{2.9}$$

The parameter γ, which, for a given trap wall radius,plasma temperature T and central density completely describes the equilibrium for that particular axial magnetic field value, takes different values γ_0 and γ_1 in the two regions. We start by assuming a value for the central density in the low field region, n_0, and a value for the low-field plasma radius (defined as the radius at which the plasma density has dropped to $1/e$ of its central value). Thus we prescribe the Debye length in the low-field region λ_{D0}, and with the chosen value of r_{p0} this sets $\gamma_0 \equiv -1/[1 - I_0(r_{p0}/\lambda_{D0})]$. Given these, we want to calculate the values of γ_1 and the central density n_1 in the high-field region, thereby completing our description of the equilibrium in the axially varying B field.

The quantity that relates the two regions is the common value of the rotational velocity ω. Given γ_0 we can calculate ω by inverting the expression for γ in Eq. 2.5. Using the quadratic root formula for $1/\omega$ we get,

$$\omega = \frac{\omega_{p0}^2(1+\gamma_0)}{\Omega_0 + \sqrt{1 - \frac{2\omega_{p0}^2}{\Omega_0^2}(1+\gamma_0)}} \tag{2.10}$$

where $\omega_{p0}^2 = 4\pi n_0 e^2/m$ and Ω_0 refers to the low-field B_0 region, and we take the '+' root in the quadratic formula as being the physically relevant one [20].

We take an iterative approach to the numerical calculation of n_1 and γ_1. The two sections are connected by two requirements: a) the entire plasma rotates as a 'rigid-rotor' at frequency ω, and b) the density variation along the symmetry axis ($r = 0$) follows a Boltzmann equilibrium; an estimate obtained from the first requirement must be consistent with the other. We begin with guesses based on physical arguments; each estimate is checked for self-consistency, providing a better estimate for a subsequent iteration. When the estimates after repeated iterations settle to stable values we have a self-consistent description of the equilibrium.

The plasma radius in the high-field region, r_{p1} is defined as the radius at which the density has fallen to $1/e$ of its value at $r = 0$ in the high-field region. An initial guess for the high-field radius may be provided by assuming that the plasma's radial edge will tend to follow the magnetic field lines, that is , $r_{p1} \approx r_{p0}\sqrt{1/\eta}$, where we use $\eta = B_1/B_0$, to represent the mirror ratio. This seems a reasonable assumption to begin with since we expect the plasma electrons to move back and forth along the field lines. We also need a value for the high-field Debye length λ_{D1}, for which we need an initial estimate of the high-field density n_1. In a cold, high-density plasma where the rotation of the plasma around its axis is dominated by the $E \times B$ drift (the remaining contribution, from the diamagnetic drift, will be relatively negligible) we expect the rotation frequency ω to be proportional to n/B. Since this ω must be constant throughout we may expect that, as a first estimate, the density along the symmetry axis will scale with the magnetic field strength. So, we have an initial guess for γ_1, given by $-1/[1 - I_0(r_{p1}\sqrt{\eta}/\lambda_{D0})]$, where we have used $\lambda_{D0}/\sqrt{\eta}$ as an estimate of the high-field Debye length λ_{D1}, accounting for the expected scaling of the density. (Recall that the Debye length is $\lambda_D = \sqrt{T/4\pi n e^2}$). We can now recalculate a better value for n_1.

With ω_{p1} estimated from the values of γ_1 obtained above,

$$\omega_{p1} = \sqrt{\frac{2\omega\eta\text{-}\;_0\left(1 - \frac{\omega}{\eta\;\;_0}\right)}{1 + \gamma_1}} \tag{2.11}$$

The ω was obtained from Eq. 2.10, using the given low-field values.The high-field density is found from the ω_{p1},

$$n_1 = \frac{m{\omega_{p1}}^2}{4\pi e^2} \tag{2.12}$$

These guess values will be closer to the actual values for some plasmas than for others, but we have found this to be reliable starting point for all cases.

We have used the constancy of ω to get an estimate of γ_1, as well as an estimate for n_1 (which also determines the Debye length λ_{D1}). So, we have the values of n and γ in both regions. Now we can numerically integrate Eq. 2.9 independently for each region, with grounded wall boundary condition $\phi(r = r_w, z) = 0$, given the separate values for γ in the two sections. The potential ϕ can be recovered from ψ in each case using the appropriate value for - (- $_0$ in the low-field and η- $_0$ for the high-field) in the scaling equation Eq. 2.5, shown again below

$$\psi \equiv \frac{e\phi}{T} - \frac{m\omega(-\ \ - \omega)r^2}{2T} \tag{2.13}$$

Thus we get the values of the central potential ϕ_0 and ϕ_1 (at $r = 0$), and we have the difference between the high and low regions

$$\Delta\phi = \phi_1 - \phi_0 \tag{2.14}$$

We want these values to be consistent with the requirement that the density variation along the central field line ($r = 0$) must be in Boltzmann equilibrium. Recall that Poisson's equation, Eq. 2.4, with $n(r, z)$, also holds for an axially varying field and we have that the density along the axis must scale as $n \propto \exp(e\phi/T)$. This means that the difference in the central potential between the high and low field regions is equal to $T \ln(n_1/n_0)$. We can rewrite part of Eq. 2.5 independently for the high and low field regions and we have,

$$\gamma_0 \equiv \frac{2m\omega(-\ {}_0 - \omega)}{4\pi n_0 e^2} - 1, \gamma_1 \equiv \frac{2m\omega(\eta\text{-}\ {}_0 - \omega)}{4\pi n_1 e^2} - 1 \tag{2.15}$$

and we may invert each equation above to express the n's in terms of the γ's. Then the potential difference along the axis, as required by the need for a Boltzmann equilibrium, may be expressed in terms of the γ's and the mirror ratio η as,

$$\Delta\phi = T \ln\left[\eta\left(\frac{1+\gamma_0}{1+\gamma_1}\right)\left(\frac{1 - \frac{\omega}{\eta\ {}_0}}{1 - \frac{\omega}{\ {}_0}}\right)\right] \tag{2.16}$$

For self-consistency we want this potential difference, estimated by Eq. 2.16, to be equal to the difference calculated earlier (Eq. 2.14), arrived at from the constancy of ω.

The iteration begins with the initial guesses for γ_1 and n_1 and it is iterated till the values become stable. We vary γ_1 around the latest best estimate until the difference between the two estimates of $\Delta\phi$ vanishes, and the values become stable. If the numerical root-finding algorithm does not converge efficiently to a sensible value, we perturb the initial guesses slightly, until the convergence is improved.

Since we integrate to calculate the function $\psi(\rho)$ in each section, we also get the radial density distribution in both sections through $n = n_0 \exp(\psi)$, which gives the density everywhere inside the trap.

Thus, we have described the thermal equilibrium of a pure electron plasma in a piece-wise uniform axial magnetic field. It is trivial to extend this to the more practical case of a smooth and continuously varying field by dividing the field and plasma into sections, connected by a constant value of ω, and relating each section to the one just preceding it. Through this procedure we recover the variation of n and γ along the axis, and the description of the axial equilibrium is complete. Of course, we assume the typical case where the radius of the plasma is much smaller than the axial variation lengths.

2.4 Characteristics of the Mirror Equilibrium

The mathematical description of an electron plasma in an axially varying field was completed in the last section. The features which differentiate the gradient equilibria from uniform field-case include:

Density varies linearly with B

In the limit of a cold plasma ($T \ll \phi_p$, the plasma potential), the density n along the axis scales linearly with the magnetic field B.

This result is predicted by the calculation described in the last section, but there is a more obvious reason for this conclusion. As mentioned earlier the plasma must rotate about its axis as a rigid-rotor with frequency given by ω. The rotation frequency of a cold-fluid ($T \rightarrow 0$) plasma about its axis is $\omega = 2\pi nec/B$ [20]; since this frequency must be constant throughout the plasma clearly we must have $n \propto B$.

As the plasma temperature is increased, the density increase with magnetic field

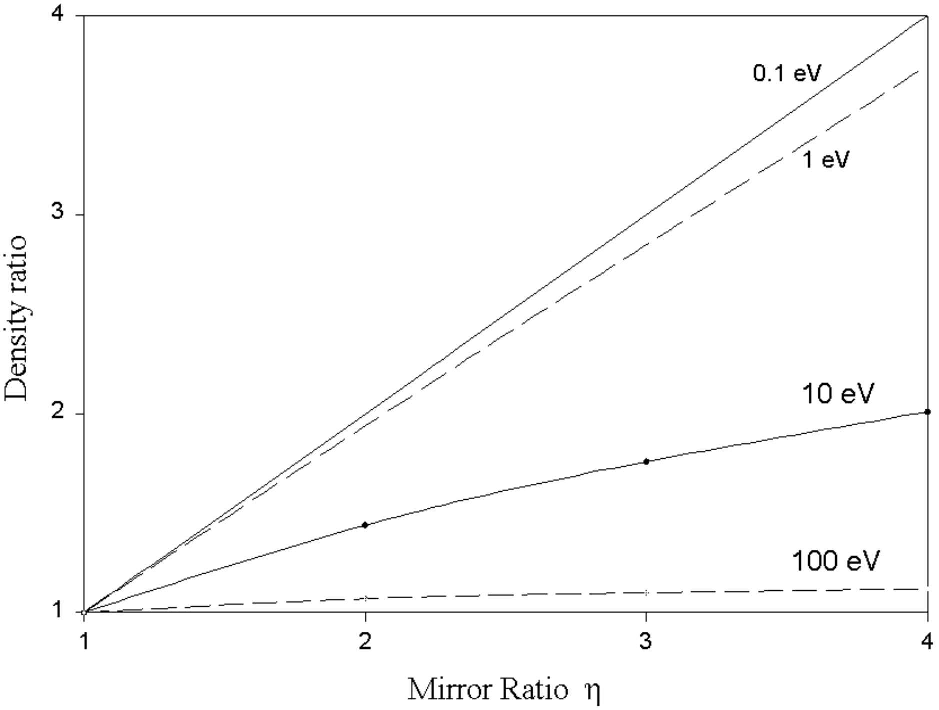

Figure 2.6: plot of n vs B at different temperatures. r_p=0.375 cm, low-field=10 kGauss and low-field density $n_0 = 10^7$ cm^{-3}. For 2 cm wall radius the central potential in the low-field for a cold plasma ($T < 0.1$ eV) is ϕ_0=4.5 Volts

becomes smaller; at very high temperatures, the plasma density becomes almost constant, and shows little dependence on the magnetic field. The reason is that with increasing temperature, the azimuthal diamagnetic drift (driven by the pressure gradient, which scales with the radial density gradient) contributes increasingly to the azimuthal velocity ωr, and the contribution of the cold-fluid $E \times B$ drift is correspondingly less. Of course, this is the limit where the long-range interactions between the electrons are small when compared with their thermal energy, and matches the behavior of a neutral plasma in a magnetic mirror where the density is independent of the magnetic field strength. However, as shown in Fig. 2.6 the scaling of n with B becomes slower than linear, even at temperatures well below the plasma potential ϕ_p.

The field lines are not equipotentials

Along the 'central field line', $r = 0$, the density must have the dependence $n = n_0 \exp(\psi) = n_0 \exp(\phi(z)/T)$, from Eq. 2.5. Then in the cold plasma limit, where the density scales linearly with B, the electrostatic potential must vary along this field line in order to produce a greater equilibrium density in the higher field region. Since we have assumed that the potential at $r = 0$ in the low-field region is zero, the potential increase $\Delta\phi$ into the high-field region is, in the $T \to 0$ case, simply

$$\Delta\phi = T \ln\left(\frac{B_1}{B_0}\right) \tag{2.17}$$

In the cold-fluid limit the potential variation is exactly the same on all magnetic field lines which remain in the *interior* of the plasma, and is given by Eq. 2.17. At higher plasma temperatures, the density becomes more nearly constant and the potential variation along field lines becomes less than that given by Eq. 2.17; but it still increases in the same direction.

This is in contrast to the situation in uniform $B-$ field plasmas (or in equilibrium neutral plasmas) where (except that the ends) the potential is constant along a field line in the plasma.

The plasma profile does not follow the field lines

The plasma must adjust its radius in the axially varying field so that, together with the density variation prescribed earlier and the boundary conditions on the trap walls, it achieves the potential variation prescribed by $\Delta\phi$. In the self-consistent plasma equilibrium the plasma radius varies such that the plasma shape does not necessarily follow the geometry of the magnetic field lines. Typically this means that, for finite trap wall radius, the plasma radius in the high field region is *smaller* than would be obtained by following the field lines from the plasma's outer edge in the low-field region. The equilibrium plasma, surrounded by grounded walls, sets up an electrostatic potential distribution which causes the radius adjustment. This happens because particles at the outer radial edge of the plasma in the low-field region are reflected back by an electric field along those field lines which keeps them out of the high-field region.

It is helpful to consider how the density variation along the magnetic field lines is determined. The plasma density is everywhere described by $n = n_0 \exp(\psi)$. Thus the contours of equal density of the plasma are determined by the 'equi-potential' contours of ψ. The function ψ is described in Eq. 2.5 for the case of an uniform axial magnetic field but this can be easily generalized to the case of an axially varying field, to make more apparent the adjustment of the plasma radius with the magnetic field. We go back to Eq. 2.3 and rewrite the expression in the exponential $H - \omega P_\theta$ in different form. $P_\theta = (p_\theta - (e/c)A_\theta(r))r$, but we may drop the first term, involving the kinetic momentum, since it is negligible in comparison with the second term for most typical plasmas considered experimentally. [It can be shown that the ratio of the two terms is comparable in magnitude to the ratio $nmc^2/(B^2/8\pi)$ [21]. This ratio becomes equal to unity at the'Brillouin limit' - the maximum possible plasma density that can be stably confined for a given magnetic field strength; for typical experimental electron plasmas this ratio is much less than unity - a 10^7 cm^{-3} density plasma in a 1 kGauss field, for example, the ratio is less than 10^{-3}]. Thus, we can keep only the term involving the vector potential in the expansion for $H - \omega P_\theta$ in Eq. 2.3 with $H = p^2/2m - e\phi$, as usual. Then, performing the integral over the Maxwellian distribution in momentum space, we have for the density n,

$$n = \int f d^3p = n_0 \exp[-(\frac{1}{T})(-e\phi(r,z) - \omega(\frac{e}{c})A_\theta(r)r)] \tag{2.18}$$

The equation may be placed in more transparent form when we notice that $A_\theta(r)r = (1/2\pi)A_\theta(r)2\pi r = (1/2\pi)\oint A_\theta(r)dl = (1/2\pi)\int_s \mathbf{B} \cdot d\mathbf{a} = (1/2\pi)\mathbf{\Phi}$, using Stokes' theorem. Here $\mathbf{\Phi}$ is the magnetic flux through a circle of radius r at the location of the particle. See Fig. 2.7. Thus, Eq. 2.18 can be written as,

$$n = n_0 \exp[-(\frac{1}{T})(-e\phi(r,z) - (\frac{\omega}{2\pi})(\frac{e}{c})\mathbf{\Phi})] \tag{2.19}$$

A contour of constant plasma density is clearly the surface for which the argument of the exponential in Eq. 2.19 is a constant. The magnetic flux $\mathbf{\Phi}$ is, of course, a constant along any given magnetic field line, as shown in Figure 2.7. Therefore, along a magnetic field line, the density follows the simple form $n \propto \exp(e\phi/T)$.

Recall that within the bulk of the plasma we already have potential variations of order T along any magnetic field line . At the radial edge of the plasma the boundary conditions of the nearby grounded trap walls can cause the potential along a field line to be substantially more negative (for electrons) in the high-field region than in the

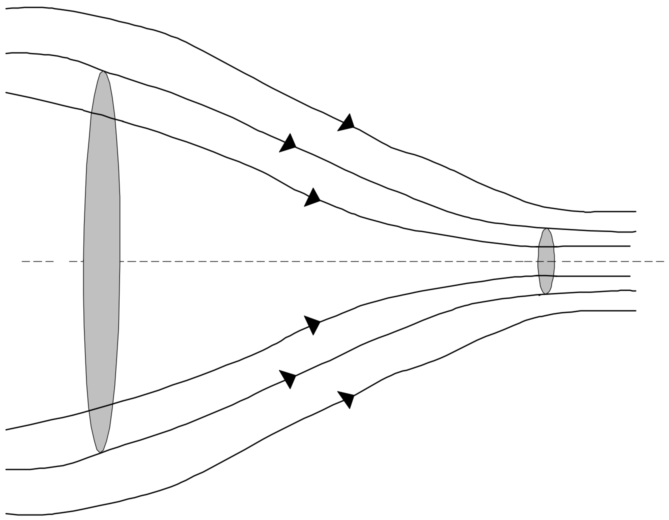

Figure 2.7: Constant flux along a field line

low-field. This result is evident in all our numerical calculations, including plasmas where the values of parameters such as density, temperature, and low-field radius have been varied over the entire range; but we have no analytic proof that includes all cases.

We show in Fig. 2.8 and Fig. 2.9 the inverse of the ratio (low-field/high-field) of the plasma radius squared in the two regions versus the ratio of the magnetic field strength, for two values of the density 5×10^6 cm^{-3} and 5×10^7 cm^{-3}. The diagonal line shows what the curves would be like if the plasma cross-sectional area did vary as $1/B$. It is clear in all the plots that the plasmas deviate substantially from this straight line. Some trends are clear in both plots: hotter plasmas tend to be closer to following the field lines than colder ones; and as the wall-radius becomes larger relative to the plasma radius, the plasma profile better matches the field line geometry. This is what we expect since in the limit of a plasma with walls at infinity there would be no boundary conditions to match and the profile would follow the field lines exactly.

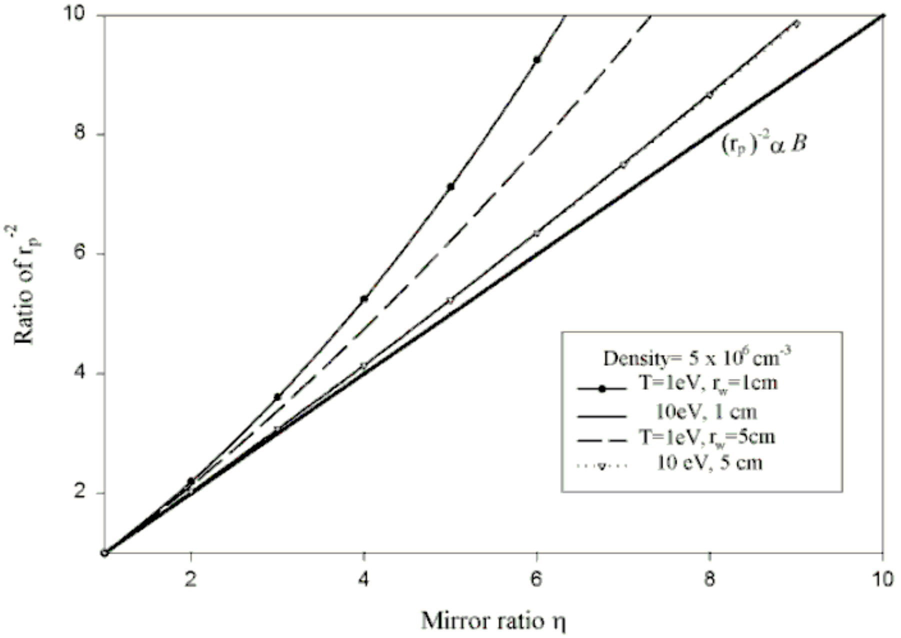

Figure 2.8: Ratio of the inverse plasma radius squared vs. the ratio of magnetic fields in the two regions, for a (low-field) density of 5×10^6 cm^{-3}. The (hi-field) plasma radius was chosen to be 0.25 cm for both plots Fig. 2.8 and Fig. 2.9. The traces are shown for two values of the plasma temperature, and different wall radii

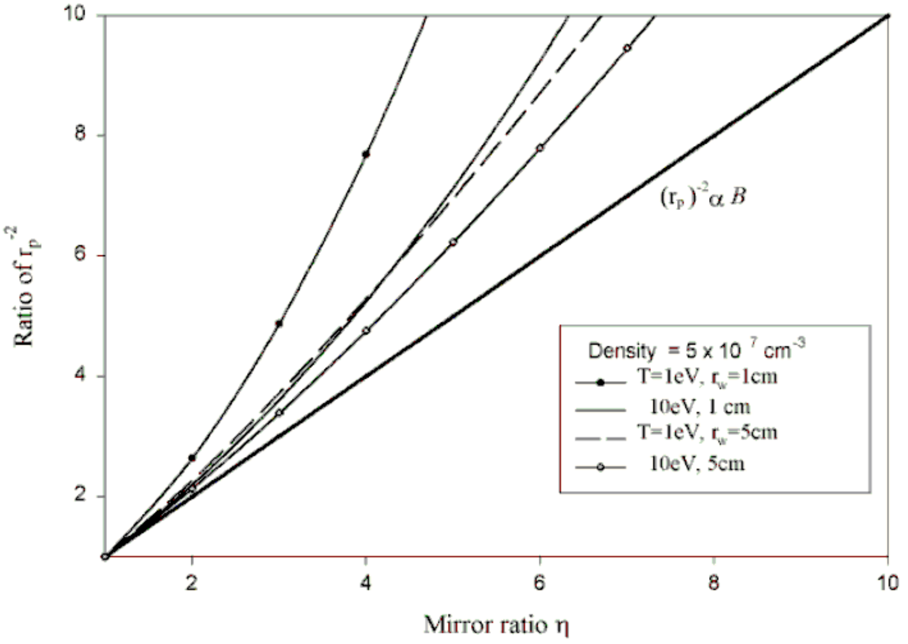

Figure 2.9: Ratio of the inverse plasma radius squared vs. the mirror ratio, for a (low-field) density of 5×10^7 cm^{-3}.

2.5 Trapped Particles

In a plasma contained in a Penning-Malmberg trap with an uniform axial magnetic field, the electrons zip to and fro at the 'bounce' frequency along the entire length of the plasma, being reflected back only at the ends by the negative potentials of the confining gates. Perhaps the most surprising aspect of an electron plasma trapped in an axially varying magnetic field is that the particles typically do not traverse the entire length of the plasma. It is well known that in a conventional neutral plasma in a magnetic mirror, some particles are trapped in the low-field region through the magnetic moment adiabatic invariant. Similarily, in a non-neutral plasma in a mirror, particles with large enough perpendicular kinetic energy and low enough parallel kinetic energy are trapped in the low-field region by the force of the magnetic field gradient which repels the magnetic moment of the electrons from the stronger field back into the lower field region. However, as noted in the last section, the field lines are not equipotentials, and there is now a potential increase toward the high field region, of order the temperature T. The thermal equilibrium velocity distribution is, of course, Maxwellian everywhere, both in $v_\perp$ and $v_\|$, and by equipartition the typical parallel kinetic energy is everywhere $T/2$. This means that a substantial fraction of the electrons in the high-field region will be trapped by this potential drop $\Delta\phi$, and will not make it all the way into the low-field region. The plasma thus has particles trapped both in the low-field region and the high-field region. The phase space regions that are trapped in each case are shown schematically in Fig. 2.10 and Fig. 2.11. The geometry of the 'untrapped' phase space in the low-field region is changed from the loss-cones (of a neutral plasma) to the interior region of a (one-sheet) hyperboloid, due to $\Delta\phi$.

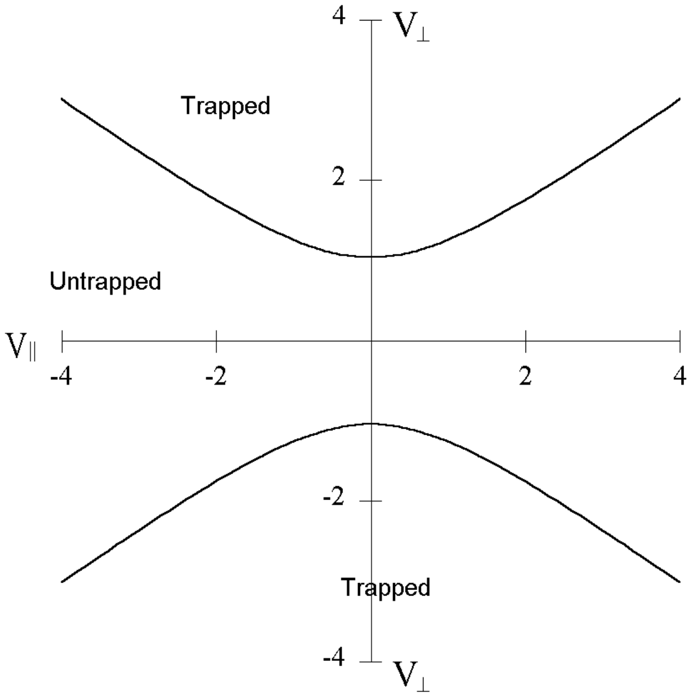

Figure 2.10: Phase spaces in the low-field region. Particles such that $m/2{v_\|}^2 < (m/2{v_\perp}^2(\eta - 1) + e\Delta\phi)$ are trapped in this region. (η is the mirror ratio, and $\Delta\phi$ is the potential difference between the high-field land low-field regions.)

As mentioned in the previous section, the plasma's radial edge does not follow the geometry of the magnetic field lines. Electrons at the plasma's outer radial edge in the low field region are reflected back along the field lines by the electrostatic

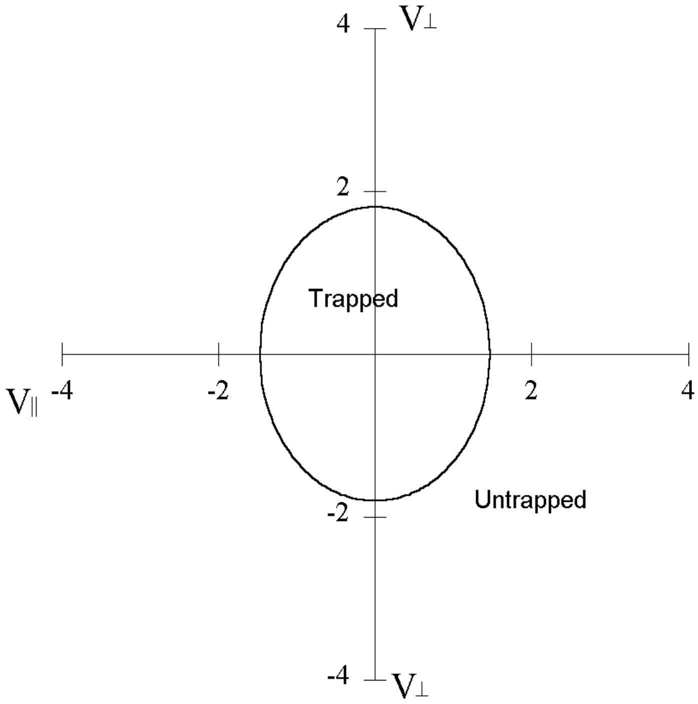

Figure 2.11: Phase space in the high-field region. Particles such that $m/2({v_\perp}^2+{v_\parallel}^2) < e\Delta\phi$ are trapped. ($\Delta\phi$ is the potential difference between the high- and low- field regions).

potential which results from the combination of the charged plasma and the boundary conditions on the conducting trap walls. In that sense, all the electrons at radial edge of the plasma in the low-field region are trapped entirely in this region. It is this that leads to the plasma 'necking down' into the high field region, faster than the converging field lines.

In Figure 2.12 and Figure 2.13 we show the trapped fraction in the respective regions for a typical plasma at temperatures of 0.1 eV and 5 eV. In Figure 2.12 we can see that the fraction of particles trapped in the low-field is somewhat less than the similar fraction that would be trapped in a neutral plasma in a magnetic mirror. This is, of course, because there is the potential increase $\Delta\phi$ from the low-field region into the high-field region which reduces the trapping efficacy of the magnetic mirror. As the temperature increases $\Delta\phi$ becomes smaller (the density variation is smaller), and the trapped fraction is very nearly the same as the neutral plasma case, as seen in

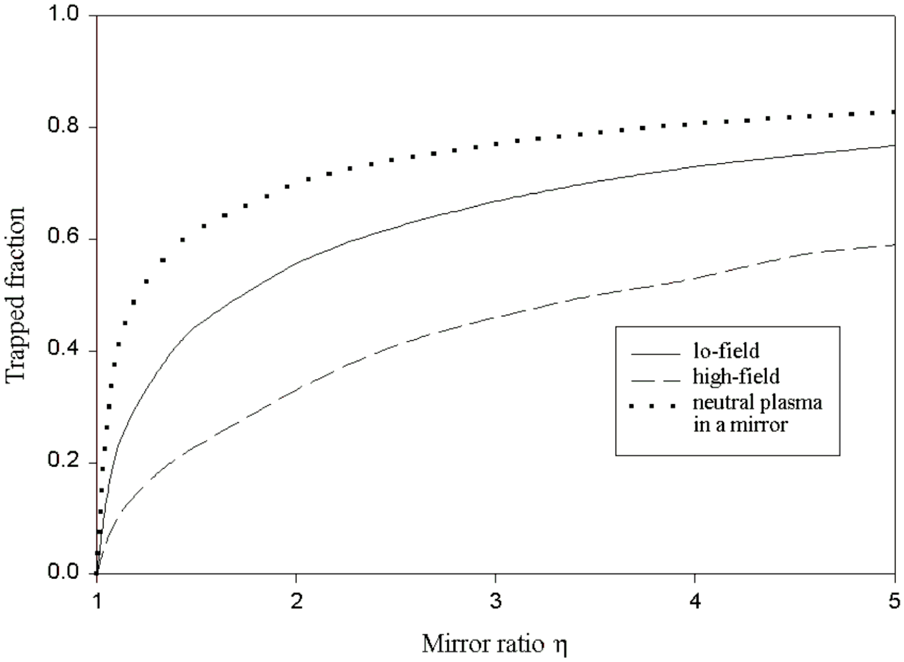

Figure 2.12: The fraction of trapped particles in the respective regions for a 0.1 eV plasma, with density 10^7 cm^{-3}, and r_{p0}=0.75 cm and r_w=1.5 cm

Figure 2.13. For this reason also the high-field trapped fraction becomes much smaller at the higher temperature; the potential drop is not as deep as in the low-temperature case. Yet in both cases, the high-field fraction is smaller than the low-field fraction because the volume of trapped phase space is much smaller.

The phenomenon of bounce-averaging along z is critical to the integrity of Penning trap electron plasmas and makes possible the study of long-term 2-D fluid-like effects in them. The fact that there are axially trapped particles renders such bounce-averaging ineffective in plasmas that are trapped in axial gradients, and may have consequences for the long-term coherence of simple modes such as the $m = 1$ diocotron oscillation.

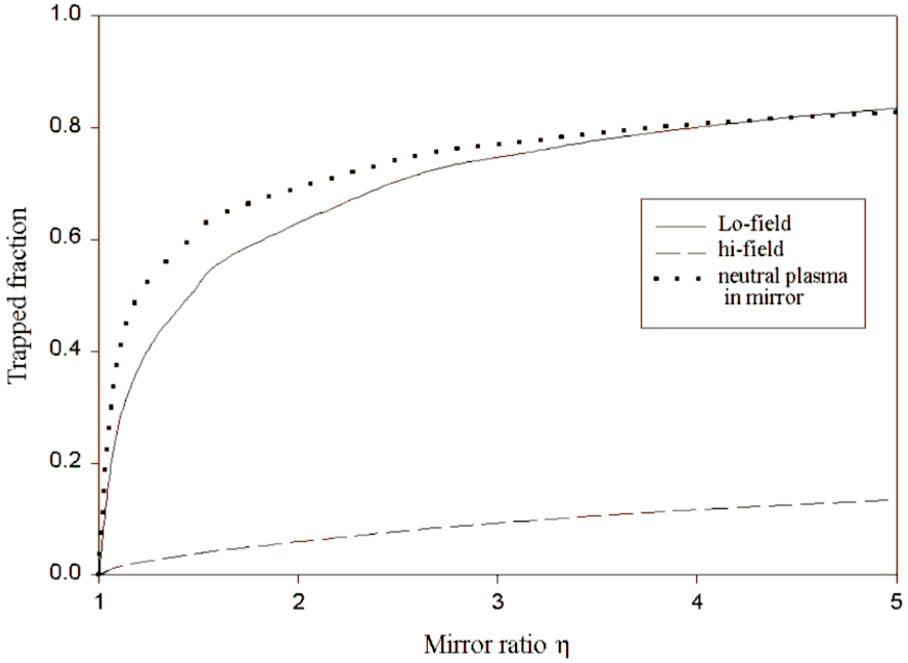

Figure 2.13: The fraction of trapped particles in the respective regions for a 5 eV plasma, with density 10^7 cm^{-3}, and r_{p0}=0.75 cm and r_w=1.5 cm

Chapter 3

The Cryogenic Electron Trap

3.1 Introduction

The experiments described in this thesis were performed on the Cryogenic Electron Trap. This trap was constructed at Berkeley to conduct experiments on cold, strongly magnetized plasmas in an axially varying magnetic field. The Trap is designed to be cooled by a liquid Helium dewar. This produces very good vacuums in the region of plasma confinement, and allows the electrons to be cooled to cryogenic temperatures. The cylindrical dewar can be moved axially in the bore of a superconducting solenoid magnet, providing a simple means of varying the magnitude of the axial magnetic field along the trap length. We are able to study the equilibria of electron plasmas in magnetic mirror-like field configurations. The trap has a thermionic filament cathode to produce the electrons, and has the diagnostic features of other typical Penning-Malmberg traps such as a phosphor screen-CCD camera based imaging system. The cathode and these diagnostics are, of course, operated at room temperature, so the trap has large thermal gradients on both sides when it is operated in the cryogenic regime.

This experiment is unique in its combination of so many aspects into one set-up. Designing a cold trap with warm regions on either end has presented some technical challenges. In this chapter I will describe the physics and engineering issues that arise in the development and operation of the Cryogenic Trap. I will also discuss some of the experimental techniques used to study the plasmas in this trap.

This trap will also form part of the Spin Experiment which is described in detail in Appendix A.

3.2 The Penning-Malmberg Trap

The basic scheme for a typical trap is shown in Fig. 3.1. The cutaway shows a cylindrical rod of charged plasma being confined axially between two negatively biased cylinders, while an external magnetic field provides the radial confinement. The axial magnetic field is coaxial with the trap cylinders and typically uniform along the axis, but as we shall see in this thesis this need not always be the case. The hollow metal cylinders are typically called 'gates'.

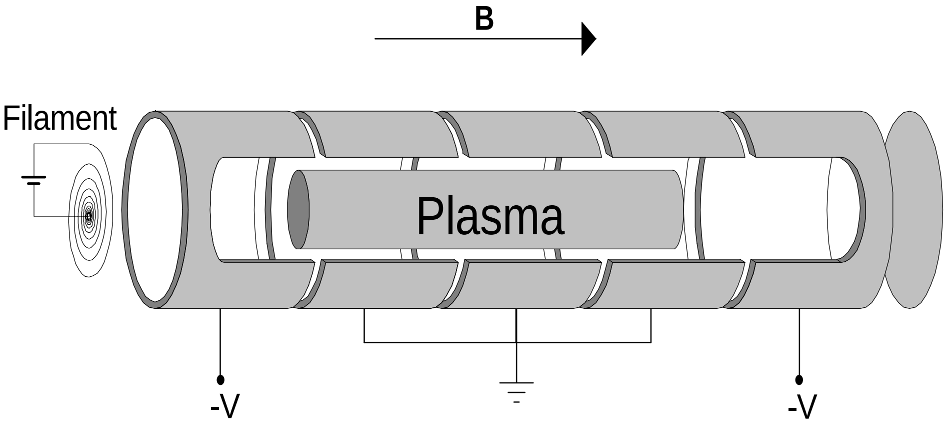

Figure 3.1: A typical Penning-Malmberg trap

A tungsten-filament wound into a spiral-shape is located at one end of the trap and acts as the cathode. Tungsten wire with a trace of thorium is often used because it is a better thermionic emitter of electrons when current is passed through the wire to heat it up (to 1500-2000 K). The filament is usually wound in a spiral-shape because the resulting potential drop across the radius of the filament better matches the $\propto r^2$ potential of an equilibrium plasma with a flat-top density distribution; this usually results in denser plasmas with low intial temperatures. The plasma radius may be controlled by adjusting the negative bias at the center of the filament [22]. When under the influence of a strong magnetic field ($\geq$ 10 kG), and prolonged heating, the filament can distort considerably from its initial shape due to the $I \times B$ forces. Since all the data in this thesis was taken on plasmas with relatively small radii, and at a strong magnetic field, a simple straight-line filament of thoriated 0.05 mm tungsten wire was used for these experiments. The filament was biased negatively to produce electron plasmas and we observed that the initial plasma temperatures were at or below the voltage drop across the filament ($\approx$ 1V), and the space charge of resulting plasma scaled more or less linearly with the filament bias, up to about -30 V. The densities were typically in the high 10^7 cm^{-3} range.

For the proposed Spin Experiment the electron plasma would be produced by the GaAs photocathode which is described in detail in Appendix A.

A plasma experiment is typically performed in an 'inject-hold-dump' cycle. During the 'inject' phase, the 'dump' gate, located at the far end from the filament, is biased negatively, with all other gates at ground. Electrons from the hot filament, biased at a negative voltage, stream along the magnetic field lines, and fill the region in between the filament and the dump gate. After a suitable wait period, generally on the order of tens of milliseconds, the 'inject' gate, located nearer the filament is biased negatively, pinching off a plasma in the 'hold' region between the inject and dump gates. The plasma is then held in the hold gate for the time that is relevant to the experiment. At the end of the 'hold' time, the dump gate is grounded, and the plasma electrons stream out, along the magnetic field lines, toward diagnostics located at that end of the trap. These diagnostics may include measurement of the total charge of the plasma and the plasma temperature at dump. A phosphor screen placed at that end, and biased at a high positive voltage, is used to produce a 2-D image of the plasma, providing information of the radial density variations. The phosphor screen, along with a CCD camera to record the images on it, now have become standard diagnostics on such traps since it was demonstrated to image plasmas sucessfully in [23].

Since the plasma is usually 'dumped' and destroyed when a measurement is made, any time-sequence of measurements must be made on different plasmas. The situation is saved by the fact that plasmas produced from a filament are highly reproducible

[22], allowing measurements on a sequence of plasmas to be as meaningful as if they were performed on a single plasma shot. It is the simplicity and reproducibility of these plasmas that makes them such a good test area for plasma physics in general.

3.3 Confinement of a Pure Electron Plasma

This section will explain how a pure electron plasma is confined in equilibrium for very long times. John Malmberg at UCSD pioneered the use of the static electric and magnetic field configuration of a Penning trap to confine and study thermal equilibrium electron plasmas. Stable pure electron (and pure ion) plasmas are now studied in a variety of traps based on the principle of the Penning-Malmberg trap; the experiment described in this thesis is one such variation.

3.3.1 Radial Confinement

A cylindrical pure electron plasma cannot be confined in stable equilibrium by static electric fields alone. However, the combination of an axial magnetic field to provide the radial confinement, and negative electrostatic potentials to provide axial confinement, works very well.

The simple explanation of radial confinement through the axial magnetic field is that the charged particles tend to remain on the magnetic fields, and that radial drifts across the magnetic field lines, toward the trap walls, occur on a time scale that is generally much slower than that of the plasma dynamics of interest.

We can also gain some insight into the radial confinement by considering conservation of the total angular momentum of the plasma. The plasma angular momentum, P_θ, as described in Chapter 2, is due to both the kinetic momentum of the electrons and the momentum due to the electromagnetic field. If we assume a non-relativistic plasma, well below the Brillouin limit ($\omega_p^2/-\ ^2 \ll 1$), the case of most experimental plasmas, the plasma angular momentum is almost entirely due to the field momentum and can approximated as [8]

$$P_\theta \simeq -\frac{B}{2c}(r_w^2 \sum_j q_j - \sum_j q_j r_j^2) \tag{3.1}$$

We assume $q_j = -e$ for electrons, and the sum is over all the plasma particles' positions r_j. The first term above, involving the trap wall radius r_w, is constant. Then, to the extent the plasma angular momentum is conserved, $\sum r_j^2$ is constant, and the particles' radial positions are constrained. The plasma can expand to the walls only through the application of torques, such as due to collisions with neutral gas molecules and non-axisymmetric external field perturbations. A trap with perfectly axisymmetric electric and magnetic fields, will conserve P_θ, through Noether's theorem, and the radial positions of the plasma particles will remain bounded for ever. The details of the mechanism through which small asymmetries in the trap couple torque into the plasma and ultimately drive it into the wall are still poorly understood. Yet, a lot of care is taken to minimize azimuthal asymmetries in these traps, to reduce radial transport. Generally, such care has led to better plasma lifetimes [24].

Recently, a 'rotating-wall' technique has been developed which injects angular momentum into such plasmas. This technique, which consists of applying sinusoidal electric fields which 'rotate' slightly faster than the plasma rotation, has the effect of injecting angular momentum into the plasma, counteracting the slow action of torques due to the asymmetries. This method has been sucessful in confining ion plasmas at near thermal equilibrium for days, which is essentially forever [25].

3.3.2 Axial Confinement

The plasma is confined axially in a grounded gate by the negative electrostatic potentials (for electrons) on the end gates, which create a potential well along the z-axis. The space charge of the plasma produces a negative plasma potential ϕ_p along the z-axis, and the plasma is well-confined if $-e(V_b - \phi_p) \gg T$ where V_b is the maximum (negative) potential produced by the confining gate potentials, along the axis. For finite length gates, V_b is always somewhat less than the potential applied to the confining gates. It is good practice to make V_b more negative than the plasma potential ϕ_p by at least several times the plasma temperature T so that even the hottest plasma electrons are confined. Making the confinement gate potential too negative can have the effect of reducing the plasma length, as the potential on the end gates penetrates further into the 'hold' gate [19].

3.4 Basic Plasma Dynamics

In order to better understand the results presented in this thesis, it is helpful to note some basic aspects of the dynamics of a non-neutral plasma in a typical Penning-Malmberg trap. While I will describe pure electron plasmas, almost everything said in this section applies to pure ion plasmas too, (with the polarities of voltages reversed for positive ions). An electron in a typical plasma undergoes three simultaneous motions: these are usually well-separated in time-scales (and length-scales) and may be considered individually.

3.4.1 Cyclotron motion

Each electron performs circular cyclotron motion in the external magnetic field. This is typically the motion with the fastest time scale (over 50 GHz/kGauss), and the Larmor radius is smaller than all the other spatial scales in the plasma. Hence, the guiding center approximation is good enough to describe the dynamics of the bulk plasma [17]. However, when considering processes that depend on electron-electron collisions, one has to look at the cyclotron motion in detail, as will be described in Chapter 6.

3.4.2 Bounce motion

As each electron undergoes cyclotron motion, it also bounces back and forth along the magnetic field lines, along the length of the plasma. The frequency of this motion is, of course, directly proportional to the parallel thermal velocity and inversely proportional to the plasma length.

$$f_b = \frac{\overline{v_\parallel}}{2L_p} \tag{3.2}$$

The cyclotron motion is superimposed on this bounce motion, and the electron traces a helical path between the ends of the plasma, as shown in Fig. 3.2. Typically, the bounce motion occurs on the second largest time scale in the plasma.For a 1 eV electron, and a 40 cm long plasma, the bounce frequency is ≈ 1 MHz.

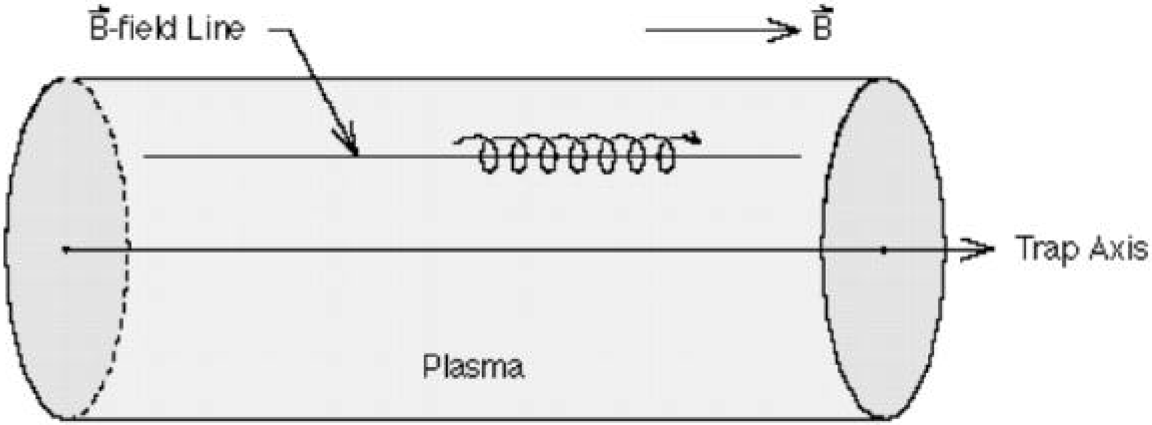

Figure 3.2: Axial drift motion of the plasma electron

3.4.3 Rotation of the Plasma

A cylindrical non-neutral plasma always has a macroscopic equilibrium electric field that points radially inward (for electrons), in the bulk of the plasma. This radial electric field, together with the external axial magnetic field, causes the entire plasma to perform $\mathbf{E} \times \mathbf{B}$ motion around the trap symmetry axis. This rotational velocity would be in the azimuthal direction, and coupled with the axial magnetic field, results in a Lorentz force which opposes the radial repulsion due to the electric field. The two forces balance each other, and the plasma can stay in stable equilibrium, essentially forever.

It is easily shown that for a flat-top density distribution, which is case of a plasma in thermal equilibrium, the rotation rate is constant throughout the plasma; the entire plasma rotates as a rigid-rotor with frequency ω_R. For a 'cold' plasma, where we may neglect the diamagnetic drift at the plasma edges, it is easily shown [17] that the angular frequency of rotation is

$$\omega_R = \frac{2\pi nec}{B} \tag{3.3}$$

This end-of-plasma view of this motion is shown in Fig. 3.3. For a plasma with an electron density 10^7 cm^{-3} in a 10 kGauss magnetic field the rotation frequency is about 15 kHz. Typically, this drift motion of the plasma electrons about the plasma symmetry axis is the slowest motion of them all. As the plasma temperature is increased, or alternatively its density reduced, the plasma may no longer maintain the 'flat-top' density profile. When the radial density gradient becomes substantial, the diamagnetic drift will make a larger contribution to the rotation velocity [13], and this contribution to the local drift velocity is given by

$$V_d = \frac{T}{m\text{-}\ n}\frac{\partial n}{\partial r} \tag{3.4}$$

Yet, as we showed in Chapter 2, the thermal equilibrium plasma still rotates as a rigid-rotor, around its symmetry axis.

The motion of each individual plasma particle is always a superposition of these three motions. It is well-known in plasma physics that there are adiabatic invariants associated with each of the motions described above: the magnetic moment is associated with the cyclotron motion; the bounce action, proportional to $v_{\|}L_p$, is associated with the bounce motion; and the magnetic flux enclosed by a circular drift orbit is the adiabatic invariant related to the drift motion about the symmetry axis.

3.5 The Trap

In the following sections I will describe aspects of the trap construction and how it is placed in the liquid Helium dewar. The trap description will be followed by a description of the dewar design and its construction.

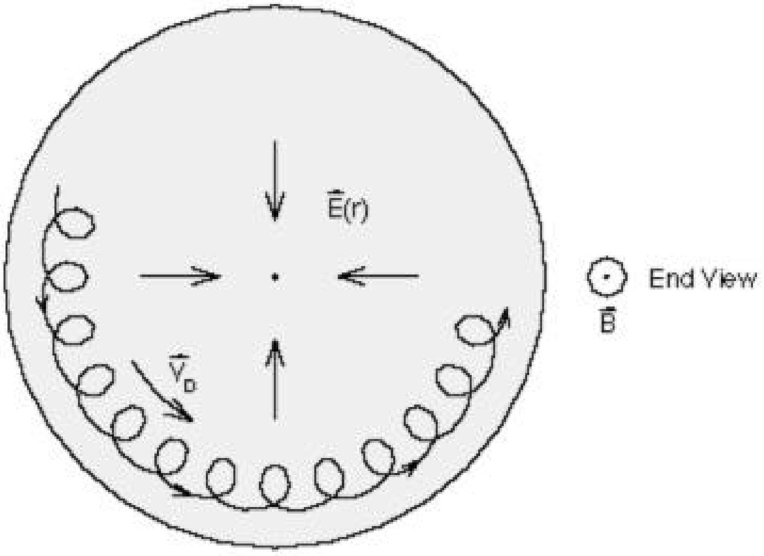

Figure 3.3: Rotational drift around the trap axis

3.5.1 Trap Construction

The useful part of the trap is about 60cm long and has 13 'gates', as shown in Figure 4.5. All gates are hollow metal cylinders of inner diameter of 2.413 cm (0.950") and are 2.54, 3.81, 5.08 or 10.16 cm long (respectively 1, 1.5, 2 or 4 inches).

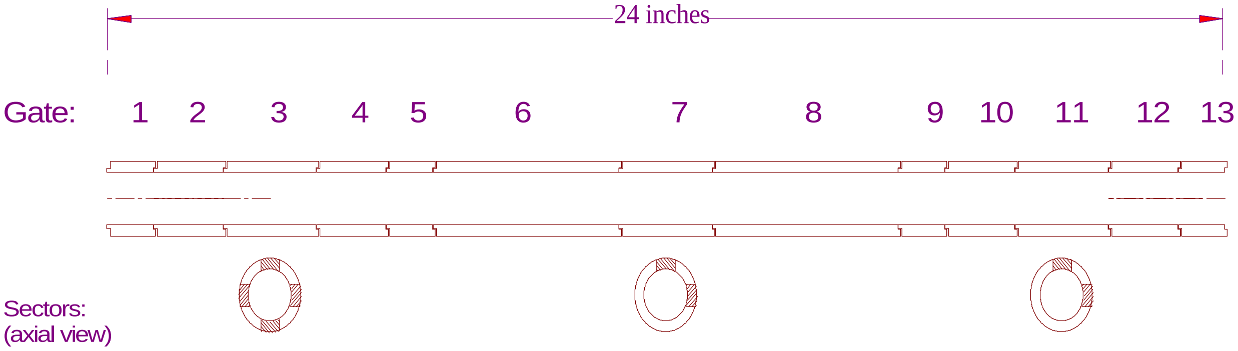

Figure 3.4: Gates' scheme for the Cryogenic Electron Trap

The gates are stacked against each other and insulated from each other by 0.030" thick ceramic spacer rings, milled flat to better than 0.001", as shown in Fig. 3.5. The gates at the end of the trap are pushed inward by screws, ensuring that the gates do not slip apart during assembly.

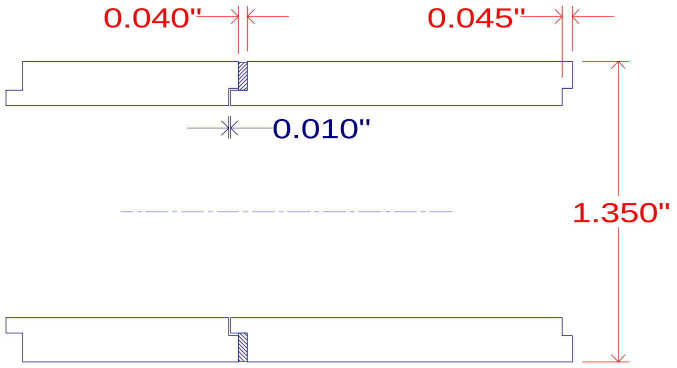

Figure 3.5: Adjacent gates stacked against each other

On the inside, the gates have a 0.010” gap between them. The gates are machined from OFHC copper to tolerances of better than 0.002 cm 0.001”. They are gold-plated to prevent oxidation; it is feared that an oxide layer may produce stray electric fields which could have reduced plasma lifetimes on previous experiments [26]. A ‘strike-layer’ of nickel is put down first, before gold plating, to prevent slow diffusion of the gold into the bulk copper.

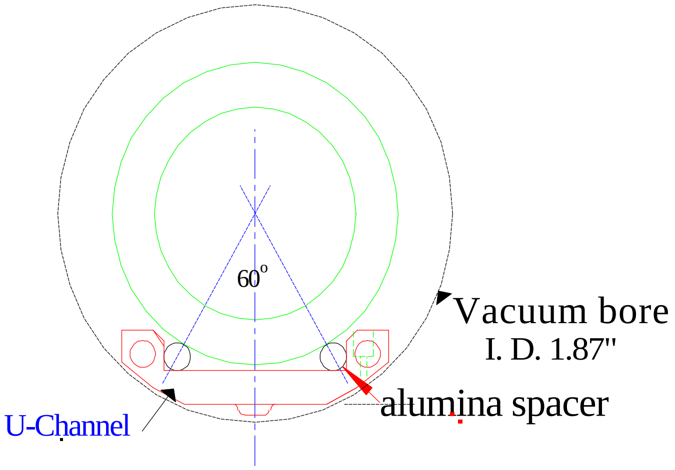

Figure 3.6: Axial view of trap, with gates resting on the U-channel

The gates are stacked in a row on a pair of (0.125”) alumina rod spacers, which insulates them from the ‘U-channel’ - the chassis that holds the entire trap together.

This is shown in the axial end view of the trap in Fig. 3.6. The 'U-channel' is attached to a copper ring at each end, which fits snugly into either end of the 4.75 cm (1.87") I. D. copper tube that forms the vacuum chamber for the cryogenic trap. It is this outer copper tube that is cooled by the liquid Helium reservoir. To cool the trap gates to near 4.2 K, we need to ensure good thermal contact between the trap chassis and the reservoir, through the copper rings. Thermal conduction between two surfaces is usually proportional to the normal force between them. At very low-temperatures we need a large force to ensure enough cooling since the thermal gradients become small too [27]. One of the copper rings supporting the 'U-channel' was provided with a lip; we used four screws to tighten it against the copper flange of the liquid helium reservoir, providing over 150 lbs. of contact force, ensuring adequate cooling at low temperatures.

The dewar, with the trap inside it, is designed to be moved axially through the bore of the superconducting solenoid, and this allows us to place various sections of the trap in regions with varying axial magnetic field gradients. In a typical position taken by the trap in the solenoid, it may be thought of as having three sections, shown in Fig. 3.4: a section on the left is meant to be in the uniform field region of the solenoid and one on the right is in the region with a strong gradient in the magnetic field; both regions are about 15 cm long. The intermediary region between them has a moderate axial gradient in the magnetic field. When the field in the uniform region is 3 Tesla, for example, the field at the far end of the non-uniform field region has fallen to about 0.7 Tesla.

All three regions have gates with sectors placed at 90^o to damp and grow diocotron modes (See Chapter 5. Gate G3 (in the uniform field region) has four sectors, symmetrically placed, while G7 and G11 have two each.

In the following sections I will describe the construction and operation of parts of the cryogenic trap, as well as the liquid Helium dewar that contains it. Many technical issues, great and small, had to be considered while constructing this trap; I have elaborated on these to give a sense of this trap's unique features.

3.6 Sector Gate Construction

The trap has three gates which have sector probes located at 90^o to each other, as shown in Fig. 3.4 These sectors provide a non-destructive diagnostic on the plasma because they allow the observation and manipulation of the diocotron mode of the plasma. The diocotron mode amplitude, determined by the size of the diocotron orbit, can be damped out when the signal from one of the sectors is amplified and sent to an adjacent sector. These techniques are discussed in greater detail in Chapter 5.

In the construction of these gates, the challenge is to make the separate pieces of the gate and its sectors so that the assembled product maintains azimuthal symmetry, with the sectors remaining insulated from the gate that contains them. To make the sector gates, slots were milled out in a 'skeleton' gate into which the sectors were placed. The sectors were held precisely in place with three ceramic pins, and each sector was kept separated from the gate by alumina washers on these pins. Figures 3.7 and 3.8 give some idea of how these were put together. This method of construction has also made possible the production of sector gates in which the sectors extend over the entire length, and which cover all azimuthal angles. This scheme, with sectors held by ceramic pins, has been used in the 'Vortex' electron trap at UC Berkeley where it is expected to enable the study of plasmas which have been distorted azimuthally into highly asymmetric shapes, over their entire length.

3.7 Dewar Construction

All the previous research on cold electron plasmas has been conducted on the 'CV' trap at UCSD, (there has also been some recent related work at Harvard University [28]); in CV the vacuum can enclosing the CV trap is immersed entirely in the liquid helium reservoir that also cools the superconducting magnet coil. The vacuum can is pumped down to a reasonable vacuum and then cooled in the liquid helium reservoir; since the entire trap is at very low temperature, essentially all gases are condensed out, and the resulting pressure is very low [29].

In our trap, we have included the ability to cool the electrons down to cryogenic

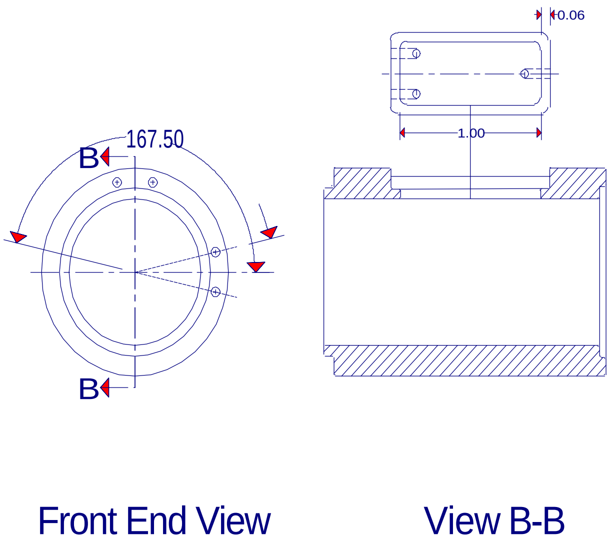

Figure 3.7: Sector Gate Construction

temperatures by cooling the trap walls with a liquid Helium reservoir. The trap is maintained at cryogenic temperatures to enable cyclotron cooling of the electron plasma, and also to provide an extremely good vacuum in the plasma confinement region. However, we also have a phosphor screen, and microchannel plate (MCP) - based temperature diagnostic, which needs to be operated at temperatures well above 4.2 K. The phosphor screen image needs to be visible to the CCD camera, and the MCP needs to be warm enough so that it recharges itself quickly after amplification of a large pulse of electrons. In our design we have placed these in a room temperature section, located at one end of the trap. The challenge was then to thermally isolate the cryogenic section of the trap from the room temperature parts. To keep the cold parts sufficiently cold we have to keep the warm parts sufficiently far away so that the thermal load is minimized. The thermal load is, of course, through radiation and conduction along the numerous electrical connections that run along the length of the trap. A cutaway of the dewar, without the trap inside it, is shown in Fig. 3.9

As described earlier, the trap is held in a copper tube at the center of the dewar. This copper tube forms the inside surface of a liquid Helium reservoir, which holds about 5 liters when full. The cold helium vapor from this cylindrical tank is passed through tubing that cools a ‘vapor shield’ that surrounds the helium reservoir. This

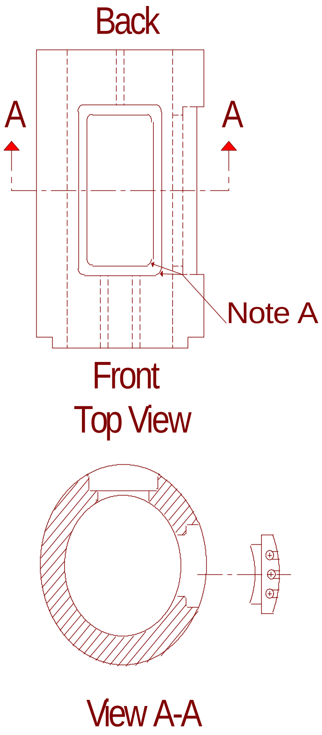

Figure 3.8: Sector Gate Construction

design keeps the vapor shield in the temperature range 20-50 K and thus keeps the thermal radiation load on the liquid helium reservoir to a negligible level. We used low-thermal conductivity stainless steel tubing between the helium reservoir and the vapor shield, but used copper tubing on the vapor shield itself to allow adequate cooling as the cold vapor passes through many turns on the shield. The vapor shield is surrounded by a stainless steel tank designed to hold liquid nitrogen. This entire setup is then wrapped up like a 'mummy' in mylar foil. We found that this was necessary to reduce the radiation from the 300 K outer walls of the dewar, which make up the rest of the dewar chamber. The inner surface of the dewar vacuum wall was electropolished to a bright finish, reducing its thermal emissivity. A vacuum lower than 10^{-3} torr in this chamber is adequate to provide thermal insulation. We placed zeolite molecular sieve on the vapor shield and the liquid nitrogen tank. While the chamber is brought to a rough vacuum with a mechanical pump, cooling the zeolite with liquid Nitrogen or Helium pumps away the residual gas and produces a vacuum

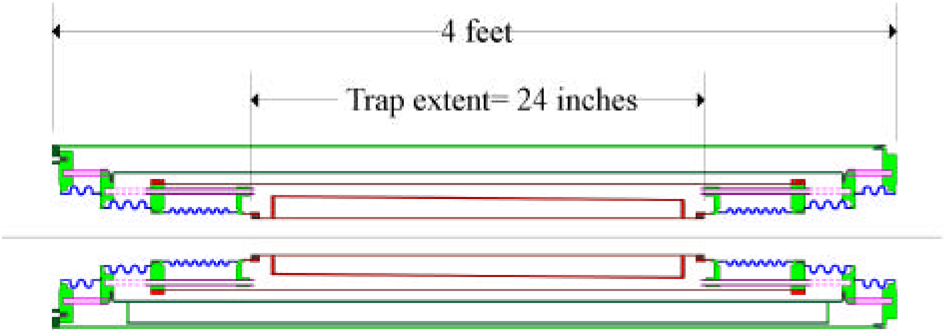

Figure 3.9: Cutaway of the Dewar

that is good enough for our purposes.

We have been careful to reduce the radiation load to the liquid Helium reservoir. We must also make sure that thermal conduction from room temperature is also reduced to a negligible level. This has proved tricky, since we want to operate the dewar with its axis lying horizontal, with both ends open. Further, we were unable to use the common materials for thermal insulation such as G10 on the insides of the trap vacuum, since such fiberglass materials are not compatible with baking to achieve a ultra-high vacuum. Since stainless steel is the ideal UHV material we decided to use bellows made of 321SS to mechanically attach the copper tube holding the trap to the outermost flange on the dewar, which is at room temperature. The bellows allow us to support a high internal vacuum even with very thin walls (0.006”). The thin walls reduce the thermal conduction considerably. Also, the convolutions on these bellows provide an increased path length from room temperature to liquid Helium temperature. Both the vapor shield and the liquid Nitrogen tank are attached at either end to flanges. We have bellows (of increasing diameter) from the copper tube to the vapor shield flange; from the vapor shield flange to the liquid Nitrogen flange and finally, from the liquid nitrogen flange to the room temperature flange of the dewar. This series of three bellows (on each side), provided a extended thermal path on both sides of the liquid Helium reservoir, reducing the heat transferred through conduction to a tolerable level.

On both ends of the Cryogenic Electron trap were a series of four baffles which obstructed the view of the trap from the outside. This blocked out almost all the room-temperature thermal radiation that might otherwise be incident on the much cooler trap. The outermost, and largest, baffle faced the room temperature section. The one just behind it was bolted tightly to the flange attached to the liquid nitrogen reservoir. This ensured that this baffle and all those interior to it were at 77 K, or colder. If all the surfaces seen by the trap were at this temperature or colder, the radiation load is reduced by a factor of $(77/300)^4 \approx 4 \times 10^{-3}$, bringing it to tolerable levels. Drift tubes, with 1.0" I. D., and machined from OFHC copper, were placed in the center of the baffles, to allow the electrons to reach the trap from the filament, and to exit the trap and reach the phosphor screen and other room temperature diagnostics. The outer surfaces of these drift tubes was provided with a bright, smooth finish, to provide greater reflectivity against incoming radiation, while the inner surfaces were given a rough finish, which reduced the transmission of infrared and microwave room-temperature photons along the insides of these drift tubes, into the trap region. These inner surfaces may be given a coating of certain metal oxides, which often have large absorption bands in the infrared, and further reduce transmission of warm photons along the insides of the drift tubes. The baffles are given a shiny polish too to reduce their emissivity.

The set of three bellows on each side of the trap tube make up the vacuum wall. However, these bellows do not give any mechanical support; this is provided by a set of four G10 tubes which connect between each set of flanges, three sets in all on each side of the trap. These 3/8" G10 tubes are short enough that the 'sag' of the trap from the outer flanges on the dewar is negligible.

Besides the radiation flux, the dominant thermal load on the cold trap insides is that due to conduction along the various electrical connections between the trap gates and the feedthroughs located on the end chamber, located at room temperature. This was kept to a minimum by using 0.009" diameter manganin wire, a poor thermal conductor, to make most of the electrical connections [30]. We used teflon tubing as insulation on the outsides of these wires. Electrical connections to the sectors, which needed to be quiet, were made with coaxial cable from Lakeshore Corp.; this cable had a stainless steel central conductor, and stainless steel braid shielding, with teflon insulation in between. Since this wire had a continuous sleeve of teflon on the outside, we introduced periodic cuts in the sleeving to allow efficient pump out of the trapped gases. To connect to the gates, we also tried using stainless steel wire earlier, but it tends to kink easily, and appeared to break when strains due to thermal contraction in cryogenic environment became significant. Besides, stainless steel is usually slightly magnetic, and may cause small asymmetries in the field, which could reduce plasma lifetimes. Phosphor bronze, another material commonly used in cryogenic applications, was avoided because it is detrimental to a ultra-high vacuum system. The teflon insulation on the wires was adequate for purposes of the data taken for this thesis, in which the trap was only cooled to liquid nitrogen temperatures. At lower temperatures, down to liquid helium, the teflon would be too great a thermal load, and would have to be eliminated. One scheme to use at the lower temperatures is to insulate the thin manganin wire by sections of alumina tubes. The alumina tubing would be split at intervals which would essentially eliminate thermal conduction along the entire length. Grounded copper tubing surrounding the alumina would provide shielding against noise, needed for sensitive measurements of very low temperatures. The Lakeshore cryogenic cable may also be used, but using large quantities may increase the possibility of virtual leaks from the tight fitting insulation and braiding. While we had attempted using this scheme from the very beginning, we frequently developed problems with wires shorting to ground through their outer shields, and we dropped this scheme for the simpler solution of using manganin wire insulated with teflon tubing.

The wires connected to the trap gates and sectors exited the trap through a series of small holes in the baffles. They then connected to electrical feedthroughs on an end chamber attached to the dewar. A silicon diode sensor, from Omega Electronics, placed on one of the trap gates allowed the temperature of the trap to be monitored accurately by measuring the voltage across a pair of leads, while a 10 μ A measuring current was passed through the other pair.

The dewar has a fill line going to each reservoir. The fill tube to the liquid Helium reservoir reaches the bottom of that tank, which is tilted slightly with respect to horizontal so that any remaining liquid collects at this end when the reservoir is near empty. As mentioned earlier, the exit tube from the liquid Helium reservoir winds its way back and forth several times on the vapor shield before leading out the dewar flange. The vacuum jacket of the fill lines are a part of the overall dewar vacuum, which must be pumped out before any filling is begun.

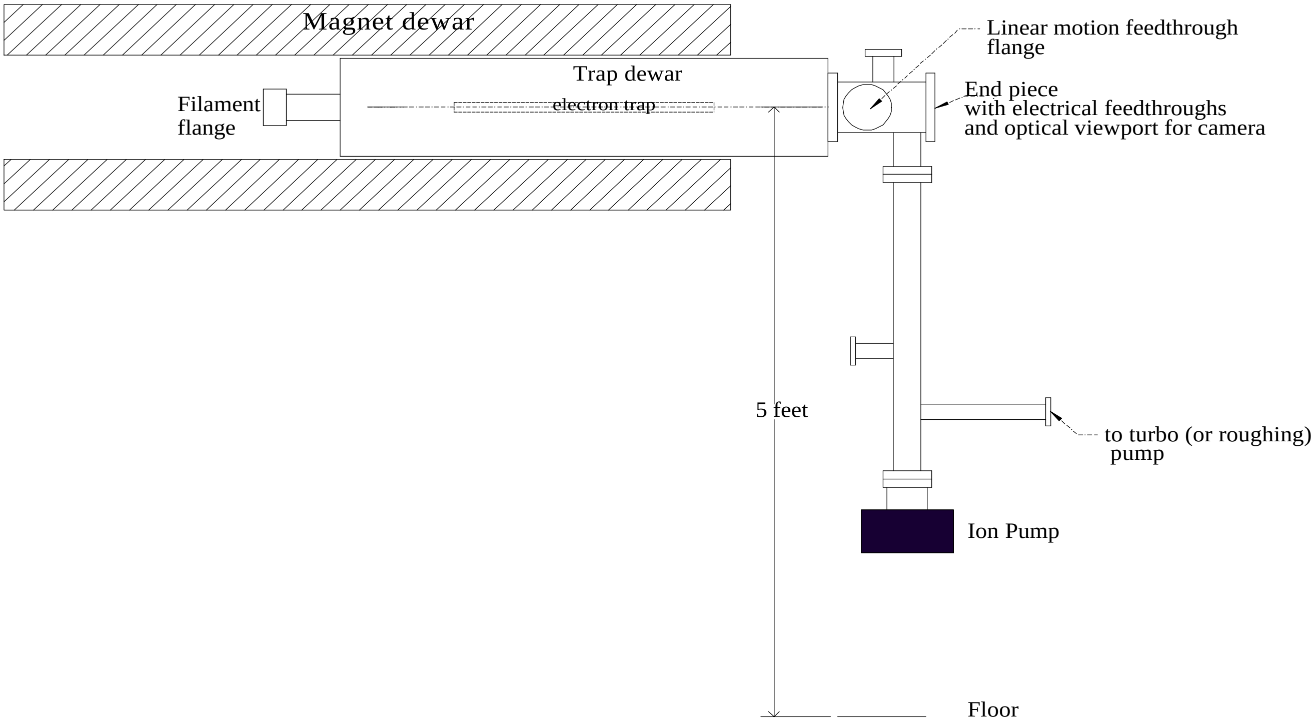

Figure 3.10: The scheme for the experiment

3.8 The Trap Vacuum

In general it is desirable to keep the neutral gas pressure in the trap as low as possible. The time scale for inelastic collisions of a plasma electron with trap neutrals can be less than a second at pressures of 10^{-8} torr ; the plasma's temperature and the velocity distribution of the electrons may be substantially affected through neutral collisions over this time scale, marring the observation of any intrinsic dynamical evolution of the plasma. Besides, a poor vacuum generally reduces the plasma lifetime, as the neutral gas applies torque to the plasma and the electrons diffuse radially outward to the trap wall through repeated collisions with neutrals. As shown in Fig. 3.6, the trap sits inside of a narrow tube of I.D. 1.87", which is about 24" long and is at the center of the LHe dewar. Most of the conductance is along the 1" I. D. tube formed by the trap gates, and this is no more than about 6 l/s. This tube opens out, through the dewar bellows, into an end chamber which have all the electrical feedthroughs to the trap. A 30 l/s ion pump hangs at the end of a long tube, with I.D. 2.5", attached to the bottom of this end chamber. The long tube ensures that the ion pump operates normally by being placed far enough out of the fringing field of the superconducting solenoid magnet. This ion pump provides the only external pumping on the ultra-high vacuum trap. A pumping speed much greater than about 30 l/s is not useful since the conductance from the plasma confinement region is much less anyway. At either end of the trap, were placed two cylindrical 'cages' containing activated charcoal. This charcoal is baked along with the rest of the trap and the containers become extremely efficient pumps when cooled to cryogenic temperatures. The charcoal absorbs almost all residual gases, except hydrogen and helium, when cooled by liquid Nitrogen in the dewar, and the remaining hydrogen and helium are condensed out by liquid helium cooling. Each of the containers provides an estimated pumping speed of 150-200 l/s [31].

For the bake-out the dewar is heated to 150^oC for a few days, during which the trap vacuum is pumped on by a turbo pump (the superconducting magnet is off during this time!). To bake out we introduce about 200 mtorr of dry nitrogen into the dewar vacuum and heat its exterior. The nitrogen gas makes sure that all parts of the trap tube and bellows are heated uniformly. As the bake is ended, the turbo pump is disconnected from the chamber, by closing an all-metal UHV valve, and the ion pump is started to provide pumping down into the UHV range. The base pressures achieved are in the low 10^{-9} torr range, as measured in the 'end-chamber' region. We have found that we are able to reach very good vacuums even though we have charcoal in the trap. When the trap is at room temperature, the pressure inside may be an order of magnitude or more higher, due to the poor conductance. However, when the trap is cooled to cryogenic temperature, the poor conductance to the room temperature part actually helps the base pressure achieved in the trap, as the charcoal pumps can produce a pressure in the trap that is about 40 times lower than that measured by the ion gauge, located near the ion pump. This pressure can be as low as the high 10^{-11} torr range, which is adequate for the purposes of this thesis, although some improvements may need to made for the Spin Experiment described in Appendix A.

3.9 The Cathode Filament

As mentioned earlier, the plasmas studied for this thesis were produced by a small length (≈ 7 mm) of 0.05mm thoriated tungsten wire. This wire was connected between the pins of a current feedthrough on a flange. The filament was typically biased negative (about 10 Volts), and a small copper plate behind the filament was also maintained at this bias. We have noticed more efficient production of electrons for plasmas when the filament is operated with this copper plate behind it; the plate remains more negative than any other point on the filament.

We have placed two irises in between the filament and the trap. One of these, with diameter 0.5", is in the middle of the drift tubes of the baffles. The other, nearer to the trap, has diameter 0.216". These irises reduce the thermal radiation from the filament to the trap. Also, we were able to limit the diameter of our plasmas to the length of the filament that is mapped along the field lines through the smaller iris. This is very useful since we have no other way of controlling the radius of our plasmas. We noticed that the plasmas created were slightly larger than the 0.216" of the iris, but remained otherwise reproducible.

It is difficult to maintain precise alignment of the filament with the iris and the center of the trap. We have mounted the filament flange on a bellows. This bellows is given mechanical support by four rods which are held rigid by a Aluminium ring. We can move the ring around until the filament is 'visible' and centered with respect to the irises.

3.10 The End-piece diagnostics

Aside from the measurements of the diocotron modes through the sector gates, all other observations of the plasmas occur by ‘dumping’ it out of the trap towards the diagnostics at the other end. In the end-piece chamber of the trap we have a linear motion feedthrough containing a set of such measuring devices. Located on a base-plate held by this feedthrough is a phosphor screen, which is used to produce 2-D images of our plasmas. The base-plate also has a holder which can alternatively hold a pin-hole charge measurement diagnostic or a micro-channel plate (MCP) electron multiplier. In a third position on this plate is a hole with a drift tube, to let electrons from the trap to pass through, as will be required by the Spin Depolarization experiment described in Appendix A. The motion of this feedthrough is perpendicular to the trap axis and it allows us to choose the diagnostic we want to use by translating the feedthrough to different positions.

The plasma electrons exit the trap along the magnetic field lines and may be imaged on the phosphor screen which is at a high-voltage. This 2-D imaging diagnostic has been described in [32]. One side of the 2.47” diameter quartz plate screen is coated with P43 phosphor and aluminized. We considered imaging our plasmas with a CCD camera which is fitted with a green filter, and we chose the P43 phosphor because it is an efficient emitter of green light. The plasma electrons that leave the trap along the magnetic fields hit the phosphor and produce a visible image when the phosphor is biased at a high-voltage (about 11-15 kV). Since the light from any part of the phosphor is proportional to the number of electrons that hit that region, we have diagnostic on the radial density variations of the plasma. The phosphor is given a coating of aluminium to block out the visible light from the filament, which would otherwise interfere with our plasma images. The phosphor screen was insulated from the copper base plate that held it by a Macor ring. A stainless steel ring, placed on top of the screen makes electrical contact to it. This ring was held down to the base plate with three nylon screws, which provided the necessary tension to keep the screen in place.

A smaller voltage ($\sim$ 40V) is enough to draw all the plasma electrons onto the phosphor screen, and we can observe the voltage signal resulting from the dumped charge on an oscilloscope. The voltage can be translated to a charge value when we measure separately the capacitance of the screen and the attached cabling. This is a diagnostic of the total plasma charge.

The other diagnostic is a copper plate with a pin-hole (diameter 0.110") in it, with a charge collection plate behind it. The back plate collects the charge that makes it through the pin-hole when the plasma is dumped. This diagnostic allows us to measure the volume charge density of the plasma through a technique better described in Chapter 4.

This pin-hole diagnostic is located in a copper housing which provides shielding from noise for the measurements of very small charge amounts. This housing, shown in Figure 3.11 can also be used to hold a MCP electron multiplier that will be used to measure very low plasma temperatures (below 50 K).

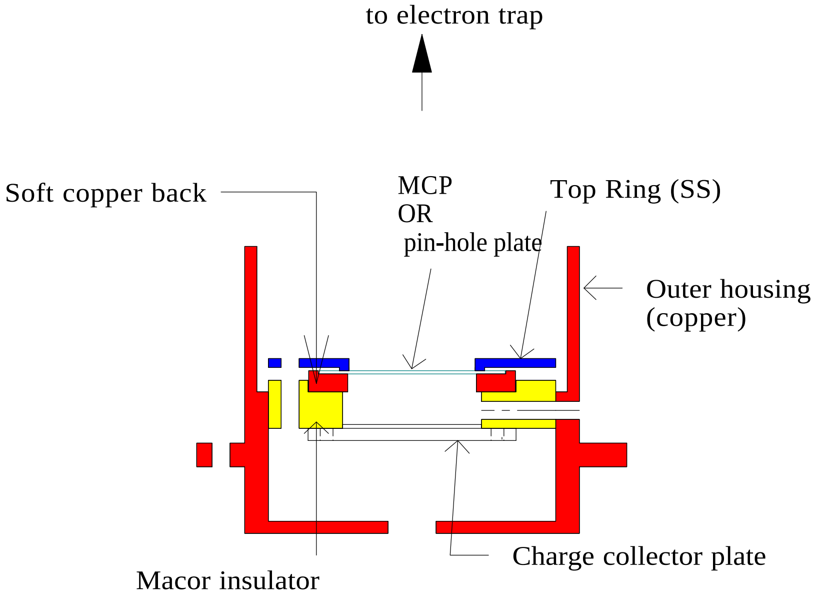

Figure 3.11: Cutaway of the Micro-channel plate holder

When we want to measure low temperatures the MCP takes the place of the pin-hole plate in the assembly shown in Figure 3.11. The MCP is held down by a stainless steel ring on to a copper ring which is annealed soft to protect the fragile 0.017" thick glass plate that makes the MCP. We use a ‘wave-disc spring’ (made of beryllium copper) in between to provide cushioning for the MCP. The SS ring biases the front face (facing the electron trap) of the channel plate while the copper back ring biases the rear side. A plate at the back of the Macor insulator collects the charge that has resulted from the MCP amplification (or made it through the pin-hole diagnostic). All of this is in the copper housing which shields it from external noise, and reduces the capacitance to ground.

The electrical connections to the MCP and charge collecting back-plate are made through wire insulated with teflon tubing. We have (grounded) copper braid on the outside of the teflon insulators to provide electrical shielding to the signals. These connecting cables were wound in a coil around a post to provide flexibility when the linear feedthrough moved to various axial positions.

3.11 The Axial Magnetic Field

The magnetic field was produced by a superconducting solenoid magnet, constructed at the Kurchatov Institute of Atomic Energy in Moscow, Russia. The room temperature bore measured 26 cm in diameter, and the uniform field region of the solenoid was 60 cm in length. The magnet could be charged up to a maximum of 3 Tesla, and all the experiments in this thesis were performed at this field strength. The field profile along the axis is shown in Figure 4.1, illustrating how the field strength varies along the trap length.

3.12 Aligning the Trap with the Magnetic Field

In the typical Penning-Malmberg trap the coils for the solenoid that provides the axial magnetic field are typically wound in place around the bore of the vacuum can of the trap. This automatically ensures that the magnetic field and the trap gates share the same symmetry axis. Since we use a superconducting solenoid, we need to be more subtle in achieving this alignment.

The electron trap gates rest on U-channel which is within a tube located in the center of a much larger dewar with an outer diameter of about 9.6". The dewar is moved axially in and out of the bore of a superconducting magnet which has a bore of diameter about 10.25", as shown in Fig. 3.10. In order to minimize torques on the plasma that would arise through non-axisymmetric fields, causing radial transport, the axis of the trap must be aligned with the axis of the magnetic field of the solenoid.

The superconducting magnet coils are thermally isolated from the physical magnet bore and are not necessarily coaxial with it. Further, the axis of the trap gates is not necessarily coincident with the axis of the dewar tube which encloses it. So it is difficult, if not impossible, to achieve alignment of the trap axis with the solenoid axis by mechanically centering the dewar in the magnet bore. We can use a procedure detailed in [33] to achieve this alignment, however. In this technique, we look at the $m = 1$ diocotron mode of the plasma where the plasma orbits about the trap axis, as shown in Fig. 3.12. Typically, we grow the mode to a fixed amplitude according to the methods described in Chapter 5. The plasma orbits around an axis which is parallel to the direction of the magnetic field. If this magnetic field is tilted with respect to the axis of the conducting gates, then during half of the diocotron cycle one end of the plasma is closer to the trap wall while during the other half the other end gets closer to the trap wall, as shown in Fig. 3.12

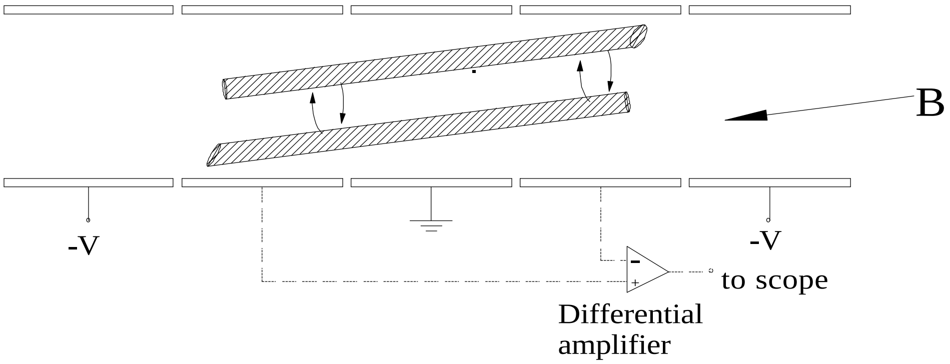

Figure 3.12: Observing a misaligned $\ell = 1$ diocotron mode

Since the diocotron frequency is much less than the plasma frequency ($f_d \sim 25$ kHz $\ll f_p \sim 15$ MHz), this effect of this motion can been seen as a quasistatic change in the plasma equilibrium. The simple physical picture is that the electrons tend to accumulate wherever they can be closer to the positive image charge on the conducting wall, since that lowers the total energy. The electrons are constrained to move along the field lines, so plasma density tends to increase at end close to the gate during one half of the cycle, while decreasing at the opposite end. Thus, the plasma density 'sloshes' back forth along its length. This 'sloshing' signal can be observed as the output of a differential amplifier connected to two gates, each located at opposite ends of the trap. The signal, even though at the diocotron frequency, would typically be out of phase with it. As the tilt angle decreases, and goes through zero, the output signal of the differential amplifier decreases in amplitude, and changes sign. Thus the trap axis can be aligned by noting where the phase between the sloshing signal and the diocotron signal changes sign. (In principle, the sloshing signal should go to zero when the tilt angle is zero, but even if the tilt angle along one axis is reduced to zero, there is always a slight misalignment along the other axis, so there is always a small sloshing signal in practice. This makes the phase a better measure of the alignment). In practice the trap tilt was changed gradually by adding teflon sheet shims about 0.010" thick on one axis (horizontal or vertical) at a time. Thus the trap, which is > 20" long, can be aligned to better than about 0.5 milliradian.

3.12.1 Alignment for Maximum Lifetime

While we have used the technique described in the last section with some sucess, a more straightforward procedure involves adjusting the trap alignment until the lifetimes of the trapped plasmas are maximised.

In general it is desirable to have plasmas last as long as possible in such traps. The longer a plasma is held in a trap the closer it is to thermal equilibrium. A global thermal equilibrium is usually the simplest situation to understand theoretically, and one would like to conduct experiments that are as close as possible to this state. As the plasma slowly expands to the wall it tends to heat up as the electrostatic energy converts to random thermal energy of the particles. Therefore, in experiments where a very cold electron plasma is desired, it is important to reduce the radial transport rate to a minimum.

As mentioned earlier the plasma electrons migrate to the walls through a combination of various torques which change the angular momentum of the electron plasma. These torques may be due to the presence of the residual neutral gas in the trap, and the non-axisymmetry of the magnetic (and electric) fields of the trap itself. We have noticed that in the mid-10^{-8} torr pressure regime that we typically operate the transport is mainly due to the slight misalignment of the magnetic field axis relative to the trap axis. We adjust the tilt in the trap axis to increase the lifetimes.

The trap is, of course, located at the center of the dewar cylinder with an outer diameter that is nearly equal to the inner diameter of the bore of the superconducting solenoid magnet. To effect the adjustment we have a set of four screws, two at each end of the magnet bore. Turning these screws slightly, one at a time, allows us to scan around a particular position to see if we can move the trap alignment to a newer position which results in a longer-lived plasma. Since each pair of screws are located at 90^o angle at the bottom of each magnet bore end, all positions of horizontal and vertical tilt are accessible. These 3/8”-24 screws allows to vary the tilt angle by as little as 0.1 milliradian at a time, allowing us to ‘tune’ the trap into the right position.

To do this scan quickly it is not necessary to measure the lifetime at each tilt position. We found it adequate to set the plasma hold time to a value that leaves behind only a small fraction of the original plasma charge, as measured when the plasma is dumped to the end diagnostic. Then we measure how much charge remains after this fixed hold time, for each tilt position, and vary the position until this residual charge is maximised. While this technique is somewhat crude it is generally effective in achieving better lifetimes. If we are more interested in maximising plasma density than total charge, then we look at the residual charge that makes it through a pin-hole when the plasma is dumped. Generally, there is little more than a factor of 2 difference between the two estimates.

We usually begin with a good ‘eyeball’ position for the alignment, making sure, for example, that the plasmas are dumped near centered on the phosphor screen visual diagnostic. Then we iterate the four screws until a position is found that results in a (usually dramatic) improvement in the amount of charge remaining. We

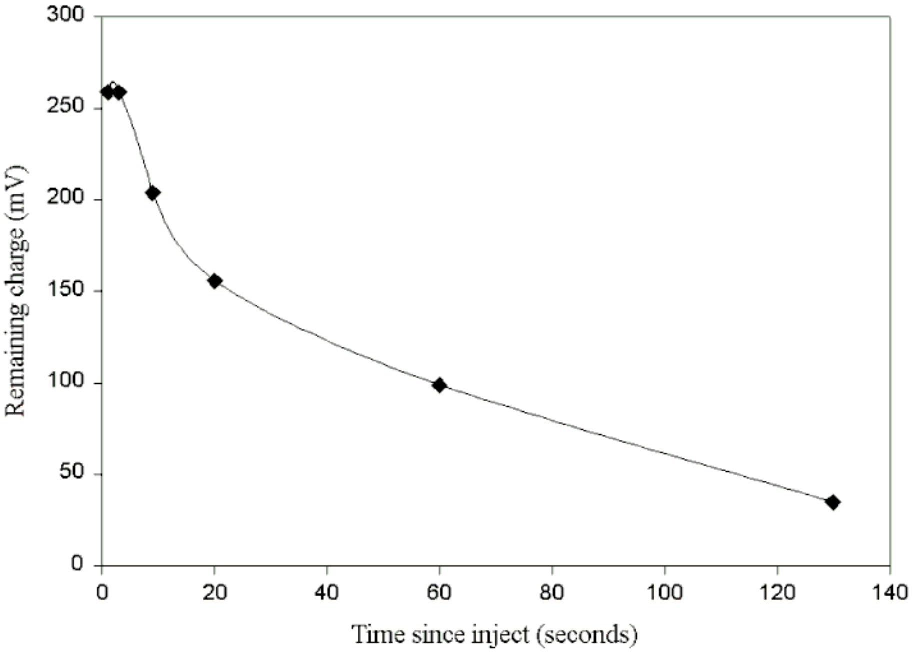

Figure 3.13: Residual plasma charge vs. time for a plasma held between G2 and G12 ($\approx$ 49 cm). The maximum field was 3 Tesla and the ratio of the fields between the ends of the plasma was $\sim$ 1.5. The trap was not aligned for maximum lifetime.

have generally not sought to try to find the 'global' optimum position for the lifetimes, usually running the experiment where the transport rate is small enough not to matter to the measurements we seek.

3.13 Plasma Lifetime

After an initial period of rapid transport, the quiescent plasma slowly loses charge to the walls. As its charge density declines, it may or may not expand and increase its radius. We define the 'lifetime' of the plasma in the trap to be the time over which the plasma's total charge declines by a factor of e. The change in the residual charge of the plasma held between gates G2 and G12 is shown in Figure 3.13

The lifetime of a pure electron plasma in a uniform axial field generally increases with magnetic field as B^2, and decreases with plasma length, scaling as L^{-2} [24] We have operated our plasma experiment without varying the maximum field of the solenoid (maintained at 3 Tesla). Although, we have no data for direct comparison, what we have observed with the axially varying field in our trap agrees qualitatively with previous work.

When the plasma is trapped only in the uniform, ‘good’ field region, we have seen the plasma last for nearly 1000 seconds. A plasma that extends out to a much greater length, including the non-uniform field region lasts for times on the order of tens of seconds. As the dewar is pushed further into the solenoid, including more ‘good’ field length, this number improves by a factor of about two, and decreases by a similar amount when the dewar is pulled out to include more of the region where the axial gradient is most pronounced.

While the misalignment seemed to be the major limiting factor on the plasma lifetime we were also able to make some improvements by improving the vacuum in the trap. This was done by cooling the trap by introducing $\mathrm{L}N_2$ into the liquid helium tank. Lowering the trap pressure (into the 10^{-10} torr range) we noticed a lifetime improvement by a factor ~ 5 at an alignment position that was roughly near the 'global' best for the alignment.

3.14 Plasma Temperature Control and Measurement

One of advantages in the study of a pure electron plasma is that its temperature can be controlled easily, over a wide range. In a magnetic field of sufficient strength, the plasma cools through the emission of cyclotron radiation to the temperature of the surrounding trap. This process is described in the next section. The plasma can be heated by applying a noise signal, in the MHz frequency range, to one of the gates that contains the plasma. Although the exact heating mechanism is not well understood, the noise signal probably excites waves in the plasma which then damp out increasing the kinetic energy of the plasma electrons. By choosing an appropriate balance between these heating and cooling mechanisms, the plasma temperature can be controllably varied over a wide range. In our experiment, we have been able to vary the plasma temperature between 0.11 eV and 12 eV, acquiring data over two orders of magnitude in this parameter. The experimental details of the heating method are described in Chapter 4. The plasma temperature can be measured by raising the dump gate potential slowly to allow electrons from the radial center of the plasma to trickle out. The amount of charge that escapes as a function of gate potential is fitted to a Maxwellian, which then provides a value for the parallel temperature of the plasma electrons. This technique has been used since the earliest days of pure electron plasma physics, and a more detailed description can be found in [29], for example. As shown in this reference, if N_e is the number of electrons that exit the plasma (and are collected on the phosphor screen) as a function of the barrier potential V_b, then the temperature T is determined (to within 5%) from

$$\frac{1}{e}\frac{d}{dV_b}\log(N_e) \simeq \frac{1.05}{k_B T} \tag{3.5}$$

This provides a good estimate of the temperature of the plasmas down to about $T \approx 500K \approx 0.05eV$. This trap is also designed to operate with colder plasmas, and the measurement technique for lower temperatures is considered in a following section.

3.14.1 Cyclotron Cooling

The plasma electrons undergoing cyclotron motion in the plane perpendicular to the magnetic field emit cyclotron photons and radiate away their perpendicular kinetic energy. Thus $T_\perp$ is lowered, and since the anisotropic temperature equilibration time ${\nu_{\perp\|}}^{-1}$ is typically much faster than this cooling rate, the plasma temperature is lowered until it comes into thermal equilibrium with the thermal radiation in the trap. This cooling rate is easily determined from a simple classical model of the electron cyclotron orbit in a magnetic field $\mathbf{B} = B\hat{z}$. The electron's motion in the perpendicular plane is given by $v_x = v_\perp \sin(- \; t)$ and $v_y = v_\perp \cos(- \; t)$ where $- \; = eB/mc$ is the cyclotron frequency. The acceleration of the electron charge is then $a_\perp = v_\perp -$ and this accelerating charge radiates. The classical Larmor formula gives the power radiated by the circular motion

$$\frac{dE_\perp}{dt} = \frac{2}{3}\frac{e^2}{c^3}{a_\perp}^2 = \frac{4e^2\text{-}\,^2}{3mc^3}E_\perp \tag{3.6}$$

where $E_\perp = m{v_\perp}^2/2$. Assuming that the velocity distributions stay Maxwellian throughout, the cooling rate of the plasma temperature is

$$\frac{dT}{dt} = \frac{2}{3}\frac{1}{k_B}\left(\frac{dE_\perp}{dt}\right) = -\frac{4e^2\text{-}\,^2}{3mc^3}T = -\frac{1}{\tau_r}T \tag{3.7}$$

where the braces denote the ensemble average, and the factor of 2/3 includes the cooling of the parallel temperature, which proceeds simultaneously, since the $T_\perp - T_\parallel$ equilibration rate is typically much faster than the cooling rate. τ_r is, therefore, an estimate of the cyclotron cooling time. A thorough calculation of the cooling rate of a pure electron plasma through cyclotron radiation including such effects as the proximity of a conducting trap walls, which act as a waveguide, is in [8]. This classical formula is remarkably good at predicting the cooling rate down to very low temperatures of about 50 K [29]. At lower temperatures, i.e. where the energy separation between the quantized cyclotron orbits or Landau levels $\hbar$- $\approx k_BT$, a large fraction of the electrons are in their lowest quantum energy levels and are no longer able to radiate; and the classical formula above must be modified to include the slowing in the cooling rate. We have observed our plasmas to cool from initial temperatures of about 0.8eV to 0.11eV in 3 seconds. This cooling rate is less that predicted by $\tau_r \approx 1$ s for a average magnetic field in our trap of about 2 Tesla. We believe this is due to the slow radial expansion of the plasma, and also a low level of noise ($\sim$ 10-20 mV$_{p-p}$)on the high-voltage pulsers that drive our confinement gates. This noise slowly heats the plasma. We believe that we should be able to achieve lower temperatures in the trap, by eliminating this noise with suitable filtering, and by also improving the plasma lifetime through better alignment.

3.15 Measuring Very Low Plasma Temperatures

Through cyclotron cooling the electron plasma may be cooled to essentially the temperature of the trap, which can be 4 K, the temperature of liquid Helium (or even lower if the dewar is pumped on). However, as the plasma's temperature is lowered T becomes an even smaller fraction of the plasma's space charge potential. This makes it harder to measure very low temperatures, as fewer electrons are observed at the high-energy tail of the parallel-velocity Maxwellian distribution. A more subtle model of the charge dump process is required, as described in [29]. The analysis described in this reference can make sense of temperature measurements down to 4 K. While we have not observed temperature less than 0.1eV (1100 K) on our trap so far, we expect to be able to do so if we take greater care. Beck and Fajans [1] produced colder plasmas on the CV trap at UCSD, but they were unable to measure temperatures below about 30 K with much certainty. The charge was dumped onto a plate in their scheme and this voltage signal was fed to a front stage amplifier which was external to the cryogenic dewar of the trap. Microphonic noise on the cable going to this external amplifier limited the ability to measure T below 30K. The MCP diagnostic described in section 3.10 is expected to provide enough initial gain ($> 10^3$) on the electron signal to overcome this problem of front end noise.

Chapter 4

Experimental Results on Mirror Equilibria

4.1 Introduction

In this chapter I will describe observations of equilibria of pure electron plasmas in a magnetic mirror field. I will describe the several techniques we have employed to study these equilibria. Comparisons of these observations with the predictions of the theory of such non-neutral plasmas in thermal equilibrium, presented in Chapter 2, will also be made.

We have studied plasmas with different levels of axial magnetic field gradient across them. The field gradient across the length of the trap can be varied by moving the dewar to different axial positions in the bore of the solenoid, as shown in Figure 4.1. We show the profile of the magnetic field alongside the trap scheme. As the trap is pulled out of the bore, the average magnetic field across its length is decreased, and the (relative) gradient is increased.

In the simplest description of an equilibrium plasma in an axially varying magnetic field, we seek to know the charge distribution everywhere - the nature of the variation of the charge density along the axis of the plasma, and the variation of the density with radius at each axial position. We have determined these variations using three main diagnostic techniques. We measure the central density of the plasma along the

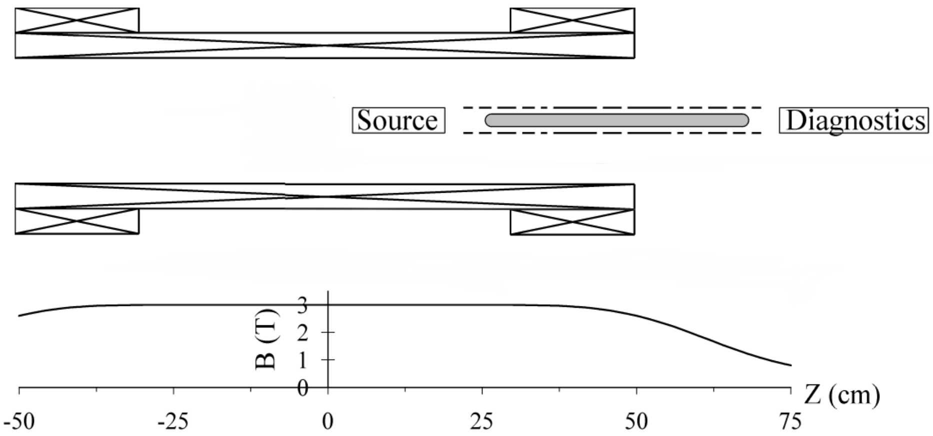

Figure 4.1: The trap in dewar scheme, with the magnetic field profile shown

axis through the 'two-split' experiment. As described in Chapter 3 we can measure the plasma charge by dumping it to a charge collector diagnostic located at one end of the trap. We can split the plasma into longitudinal sections by applying negative biases on intermediate gates (typically, in two places), before the dump. The plasma may then be dumped in sections; we measure the charge from each section in the sequence that it is dumped to the end diagnostic. When the plasma is dumped the charge that reaches a particular point on the charge collector gets there by propagating along the magnetic field lines. By collecting the charge that makes it through a pin-hole at this end we were able to sample the plasma density in each section. The 'two-split' experiment allows us to measure the relative variation of the density with magnetic field, along the axis of the plasma. We will see that these measurements compare well with the theoretical model of such plasmas.

The plasma is made up of un-neutralized charge and is confined in a metal cylinders that are typically at ground potential. When the plasma is dumped the amount of charge that flows into the gate from ground is equal (and of opposite sign) to the amount of plasma in the hollow of the gate, as is required by Gauss' law. The total plasma charge that resides in a given gate at the end of the 'hold' period, can be observed easily on a scope when the plasma is ‘dumped’ out of the trap, at the end of this period. When we measure this charge from each gate in the stack we have a straightforward diagnostic on the charge per unit length, the linear charge density of the plasma, at various points along its length. Our line-charge measurements and the theoretically expected values seem to be in general agreement.

Our third diagnostic measures the (axially averaged) radial density profile of the plasma. The pin-hole charge collector is placed on a linear motion feedthrough which allows us to move the pin-hole (and charge collector) in a line perpendicular to the trap axis. We move this pin-hole to various positions along this line, and by measuring the charge each time we are able to acquire a map of the radial distribution of plasma density (averaged over the plasma length, of course). If the plasma were dumped in sections, we acquire the radial density maps of each section, allowing us to compare the radial profiles of the low-field region with that of the high-field region.

From the ‘line-charge’ measurement and the measurements through the pin-hole of the charge density along the axis we acquire knowledge of the charge distribution of the plasma. The description of the plasma would be complete if we knew the velocity distribution of the particles at each point in the plasma. At present, there is no diagnostic that measures the entire velocity distribution of an electron plasma. (Techniques using laser-induced fluorescence have been used very effectively to study the velocity-space dynamics in a pure-ion plasma [34] but there are no bound states for the free electron, and this technique does not work for pure electron plasmas). We content ourselves with the assumption that even if the temperature is not uniform across the plasma, the velocity distribution is everywhere a Maxwellian. We can leak out the electrons at the high-energy tail and estimate the temperature by fitting this charge signal to a Maxwellian, giving us the temperature at the radial center of the plasma; this method has been described in greater detail in Chapter 3. Since most experiments allow the plasma to equilibrate for at least a few electron-electron collision times, the assumption that particles are Maxwellian at least along field lines appears a good one, and seems to be adequate to describe the data.

The extremes of plasma behavior are expected at the limit of cold, high density plasmas on the one hand, and hot, tenuous plasmas on the other. We cover these limits, and the parameter region in between, by lowering the density, or increasing the temperature of the plasmas' initial state which is cold and dense.

We have not tried a combination of 'splitting' and heating, since it was not necessary to cover the parameter range of interest.

As we described earlier the axial gradient across the length of the plasma is varied by placing the dewar in different axial positions in the magnet bore. We have taken data on the 'two-split' experiment and the line-charge measurement with the trap placed in two positions - one with the dewar flange about 9 cm from the magnet bore end, and another with it pulled out to about 25 cm. Since we know the field distribution of the solenoid magnet in the entire region relevant to the experiment we can ascertain the magnetic field profile across the length of the trap in any axial position.

We also took data on comparing the radial profiles of the two-split plasma, and these data were taken with the trap placed in between these positions, with the dewar pulled out 16 cm, where the effect was most likely to be observed.

All our data was taken with the solenoid charged up to a maximum field strength of 3 Tesla (30 kGauss); a large field provides a longer lifetime and a faster cooling rate for the plasma.

In the following sections, we will describe how we create the plasma equilibrium and control its density and temperature. Next, we cover how the diagnostics were used to reveal features of the plasma equilibrium, and compare these observations with the global thermal equilibrium theory of Chapter 2. Where the observations deviate significantly from the theoretical prediction, plausible explanations are given for the difference.

4.2 Creating the Plasma Equilibrium

To study the plasma equilibria we need to be able to produce plasmas where we can control the radius, density and temperature in a reproducible manner. The theory of Chapter 2 refers to a plasma that is in global thermal equilibrium. An electron plasma created in our machine would take a relatively long time to achieve this complete thermal equilibrium. This time is limited by the rate of cross-field transport in electron plasmas. From the observations of the approach of plasmas toward thermal equilibrium in [14], we estimate that this does not happen in our plasmas for perhaps 10 seconds or more. For practical reasons, we have chosen to look at plasmas after a hold time that is much shorter; so we expect that most or all of the plasmas we have studied for this thesis are not in this ideal state. Yet we expect that they are all in a Vlasov equilibrium that is some approximation of the global thermal equilibrium state.

As mentioned in Chapter 3, the electron plasma was created from the thermionic emission of a filament; the space charge of plasma created was roughly equal to the (negative) bias on the filament relative to ground, equal to -10 V. An iris placed in front of the filament, with radius equal to 0.275 cm, allows us to control the radius of the plasma that was formed since electrons on field lines outside of this radius do not make it into the trap to create a plasma. The radius of the plasma created (in the high-field region) was typically slightly larger than the iris radius, but otherwise remained reproducible. We used inject times (duration for which the inject gate is at ground) of 100 milliseconds (ms), since this produced the plasmas with the most amount of total charge, with the least level of shot-to-shot fluctuation.

In Chapter 2 we showed that the thermal equilibrium state of the plasma in a mirror field is completely determined by the values of the parameter γ and the central density n at a reference point on the axis. Given the values of n_0 and γ_0 we can calculate the density everywhere else. However, if we are only concerned with the relative density distribution then all we need is the value of γ at the reference point. γ is, of course, set by the value of the plasma radius and the Debye length at that point. Since the plasma radii at the high-field end are set by the iris, we can parametrize all our plasmas by λ_D. Since $\lambda_D \propto \sqrt{T/n}$, we can look at all of our data in terms of the parameter ratio T/n. Dense, cold plasmas and hot plasmas of low density would be at the opposite limits of plasma behavior, in this viewpoint. High temperatures are equivalent to lower densities, and vice versa. We begin by creating cold, dense plasmas; this is a desirable starting point since it is easy to heat the plasma, or lower its density, to cover the rest of the parameter range. We have not tried a combination of ‘splitting’ and heating, since it was not necessary.

4.2.1 Varying the Density

The plasma’s total space charge potential, after initial injection, was essentially fixed by the bias on the filament, and produced plasmas with a density (averaged over its length) of about 7×10^7 cm^{-3}. We estimate this by dumping the entire plasma onto the phosphor screen; the resulting voltage signal is translated to a charge value when multiplied by the capacitance (to ground) of the phosphor screen. We determine this phosphor screen capacitance by putting it in series with another calibrated capacitor, and measuring the voltage attenuation when a sinusoidal signal is fed between the ends. We have an estimate of the plasma radius from the size of the filament iris, and we are able to confirm this from the pin-hole diagnostic. Along with our knowledge of the plasma length, set by the confinement region, this allows us to estimate the density of the plasma and we have found it high enough to confirm the predictions of our theory. To produce ‘thinner’ plasmas, with lower densities, we use ‘splitting’, where a section of the plasma is split (by applying a negative bias on an intermediate gate) and dumped and this sequence is repeated to reduce the density of the plasma that remains by as much as is desired. The scheme for this is shown in Figure 4.2. We have been able to reduce the total charge in the plasma by as much as 100 times less than the initial value, i.e., into the 10^5 cm^{-3} range.

4.2.2 Varying the Temperature

Our method of determining the plasma temperature was described in Chapter 3. The plasma were created with initial temperatures ≈ 0.7 eV. As described in Chapter 3 we can lower this by holding the plasma for long enough that cyclotron cooling takes effect. After a 3 second hold time we were able to produce reproducible plasma temperatures of 0.11 eV. This cooling rate is smaller than the theoretical rate given by the classical Larmor formula for dipole radiation in a 3 Tesla field. This is because of the slow radial expansion of the plasma, which causes Joule heating [29], and perhaps also some residual high-frequency noise on the pulsers that drive the confinement

Figure 4.2: The ‘splitting’ scheme to lower the plasma density. The split-dump-expand procedure may be repeated many times to reduce the density by a factor of over ~ 100.

gates, which may cause some heating during the hold period. However, temperatures of about 0.4 eV were low enough to confirm the high-density, low-temperature limit of our theory and this temperature was obtained after a hold time of only 1 second. Thus, we chose our hold times to be 1 second long; longer times would correspondingly lower the rate at which we acquired data (We typically averaged over 25 shots for each data point). We noticed that the temperatures of plasmas whose density had been reduced by ‘splitting’ also remained near 0.4 eV, after a 1 second hold time. The measurement of low temperatures (less than 0.7 eV) was complicated by high-frequency noise coupling into the charge signal, from the dump pulser. We included a circuit on the output of the dump pulser to reduce the level of this noise.

To study plasmas with temperatures greater than 0.4 eV, we heated the plasma with 10 MHz ‘white’ noise from a signal generator, fed to G10 for the entire ‘hold’ time. By increasing the amplitude of this noise signal we were able to create plasmas with (final) temperatures as high as 12 eV. The final observed plasma temperature as a function of the heater noise amplitude is shown in Figure 4.3.

This heating method also caused the total plasma charge to change considerably.

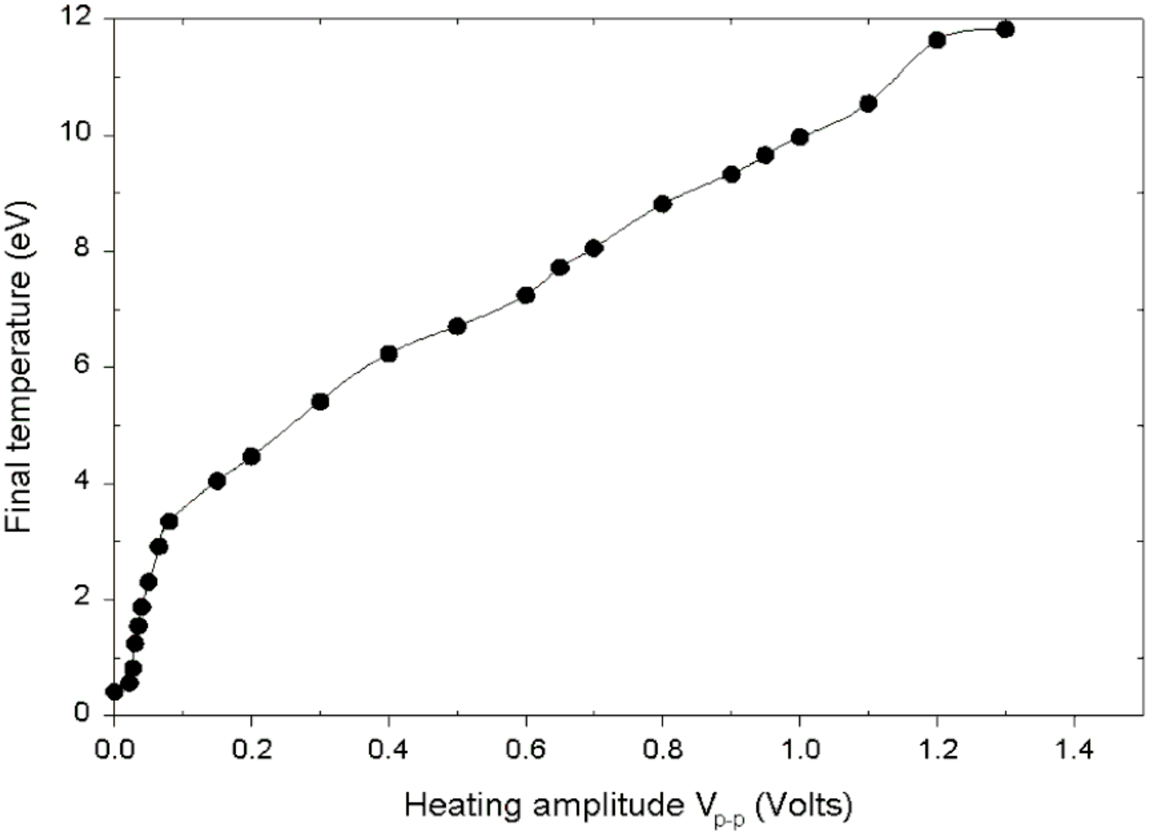

Figure 4.3: Final plasma temperature vs. heating noise level

As the amplitude of noise signal from the signal generator was increased from 0 to 200mV the amount of plasma charge, at the end of the hold time, also increased. We have assumed that this was due to ionization of the background neutrals, which increases as the plasma electrons become more energetic.

However, above a certain noise level, we noticed that the total plasma charge began to decrease as a function of noise amplitude. This decrease may be due to the fact that the electrons were getting hot enough that the hottest electrons may be slowly being evaporated over the -80 V confinement gate potentials [35]. We noticed that we were able to reduce this effect somewhat by passing the noise signal through a high-pass filter with cut-off at 20 kHz. We found that this also allowed us to vary the temperature more smoothly as a function of the heater amplitude. We have used the filtering for all levels of heating amplitude, and the measurements shown in Figure 4.3

were performed with the filter included in the heating circuit. The plasma charge at a heating level of 1.3 V was about one tenth the charge at 0.2 V, even as the final temperature was nearly three times bigger.

When observing plasmas that have been heated to high temperatures, we tried to include as much of the dumped charge signal as possible into our analysis of the temperatures; this eliminates the problem that the high energy end of the Maxwellian tail may be depleted through evaporation over the confinement gates.

During the entire time of the hold, we kept the diocotron mode suppression on, to kill any stray off-axis drift of the plasma (The off-axis dioctron mode and its damping through feedback is described in Chapter 5). After the 1 second heating, the plasma was held quiescent for 50 ms, with no feedback or diocotron suppression, before any measurements were made. This 'quiet' time allows collisions to thermalise the electron velocity and density distributions, at least along field lines.

Thus, starting with cold, dense plasmas we were able to cover the entire parameter range necessary to confirm our theory, by lowering the density, or alternatively, raising the temperature. Reductions of a factor of 100 in the density n and increases in the temperature T of over a factor of 10 were easily achieved, and we have been able to cover a range of more than two orders of magnitude in the relevant parameter T/n.

4.3 Density variation with Magnetic Field

The simplest theoretical prediction of a plasma in an axially varying magnetic field is the variation of the volume charge density of the plasma along the axis. We have used a simple technique to sample the density in symmetrical sections of the plasma, located in regions with different values of the magnetic field strength (and axial field gradient).

When the plasma is dumped, the charge that reaches a particular point on the charge collector at one end of the trap gets there by following the magnetic field lines. If this charge is collected through a pin-hole, we collect all the charge in the volume that is mapped by the field lines from the pin-hole back into the plasma. If the plasma is split along its length, and dumped in sections, we are able to sample the volume determined by the ‘mapped cross-section’ of the pinhole, as shown schematically in Figure 4.4.

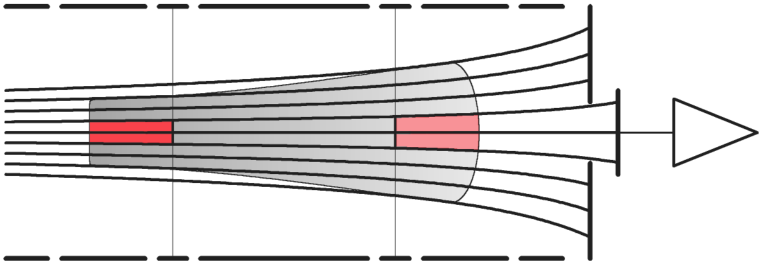

Figure 4.4: Measuring density from two sections

Since we know the field strength everywhere along the axis we know the (relative) volumes of the region whence came the charge that made it through the pin-hole. Dividing by the length of the section which issued the charge signal, and the mapped cross-section of the pinhole, yields the volume charge density of the plasma in each section (averaged over the length of each section, of course).

As shown in Fig. 4.5, the trap is symmetrical about its mid-point; gates of equal length are located at equal distances from this mid-point. Gates G5 and G9, for instance, are both 1 inch long and located 6 inches from the corresponding ends of the trap. If G12 and G2 were used as the inject and hold gates respectively, then applying a high negative bias to G5 and G9 simultaneously would split the plasma into three sections, the outer two being of the same length. The two sections of equal length are located in regions with a different magnetic field strength.

As mentioned earlier, we hold all plasmas for 1 second each. The heating, if necessary, is done during the duration of the hold time. Any ‘splitting’ to reduce density is performed before the hold time. At the end of the ‘quiet’ period of 50 ms which follows the hold we split the plasma into three sections by rapidly applying negative biases on G5 and G9 simultaneously. It is important to perform this splitting on the two gates as symmetrically as possible. Both gates are connected to the same pulser to achieve this. About 60 microseconds (μs) after G5 and G9 are biased negative, to -80 volts, we ground the ’dump’ gate G2, to let out the section of plasma that is trapped between G2 and G5. Soon after the plasma is split into three parts,

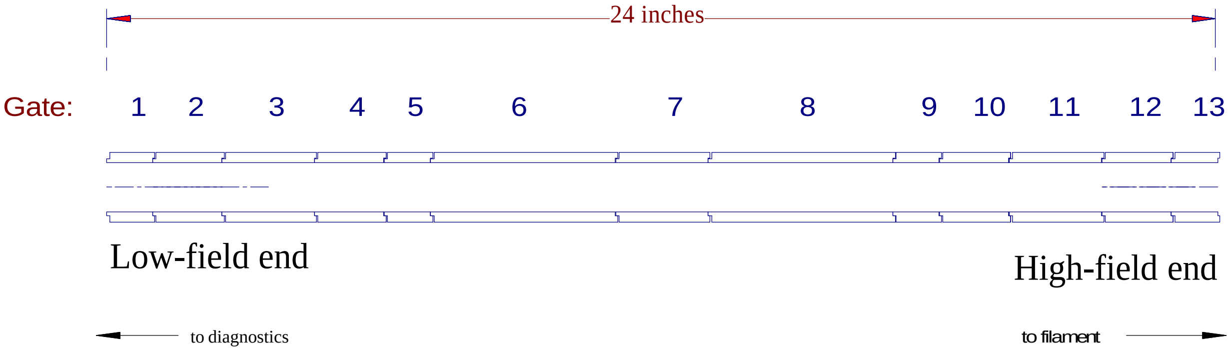

Figure 4.5: Gates' scheme for the Cryogenic Electron Trap

with G5 and G9 driven by the same high voltage pulser, we use a relay to switch G9 to another pulser. This pulser ensures that G9 stays negative even after the pulser connected to G5 goes to ground, dumping the middle section of the plasma. About 10 ms after the first section is dumped to the diagnostic, we dump the middle section by grounding G5. About 25 ms after the middle section is dumped, the pulser connected to G9 goes to ground, causing the third and last section to be dumped to the charge collection diagnostic.

When each section is dumped it is important to ensure that the plasma is centered as close as possible to the trap axis before it exits the trap, that is, there is no large amplitude diocotron oscillation present. This is to ensure that the pin-hole only samples charge from the radial center of the plasma, and not from its edges. The 'splitting' gates switch from ground potential to -80 Volts in less than a few microseconds. This relatively fast potential change can induce the plasma in each section to drift off-axis, initiating a diocotron mode. We found that by dumping the first section almost immediately after the splits have occurred (about 60 μs later), such drifts are minimized, and the plasmas remain close to the center of the trap. Similarily, after the middle section is dumped, we keep diocotron suppression on for about 25 ms on the sectors of G11, to ensure that the last plasma section is pushed back to the axis of the trap. We do not worry about this problem for the middle section since we generally do not include this section of plasma in our analysis.

It is important to ensure that the four high-voltage pulsers used to produce a split plasma are all equivalent. This means that they all go to the same negative bias of -80 V when pulsing, and go to 0 Volts (within 10mV) when they are supposed to be at ‘ground’. This ensures that the plasmas in the ‘front’ and ‘back’ sections are treated equivalently. A higher negative bias on one end pulser, for example, will squeeze the plasma length in that section more, resulting in the two sections seeing different conditions during the splitting process.

Once a section is dumped, it leaves the trap region along the magnetic field lines, toward the charge collection diagnostic. Given knowledge of the magnetic field along the axis of the trap, we can measure the *volume* charge density in the two sections of the plasma, one of which is in a region with where the average field is low and the other where the average field is a factor of 1.5-3.0 higher. As mentioned earlier, we allow each dumped section of the plasma to hit a plate with a 0.279 cm pin-hole in the center. Behind the pin-hole is another plate that collects the charge that makes it through the pin-hole. As described in Chapter 3, both these plates are placed in a grounded copper housing which provides adequate electrostatic shielding, reducing coupling noise on the measurements of small signals. Both the plate with the pin-hole and the back-plate behind it are independently connected using shielded coaxial conductors. I typically bias the front plate to +60 Volts, using a battery; a voltage this high seems necessary to make sure that all the charge makes it out of the trap. The back plate, where the charge through the pin-hole is collected, is biased at +90 Volts. The other end of the biasing battery box (a series of standard batteries) is connected to a Voltage pre-amplifier (a Stanford Research Systems 560 amplifier), typically operated with a gain of 100.

The oscilloscope trace of this amplifier output will show three distinct charge signals, separated in time from each other. The *RC* decay time of each charge dump signal is about 2 ms resulting from the 100 M - input impedance of the SRS amplifier and capacitance of the back-plate+cable to ground. Each charge dump can be observed distinctly because, as mentioned earlier, they are separated by at least 10 ms. Digital background subtraction was used to eliminate the effect of electrical coupling (from the switching voltages on the dump gates) from the total signal traces on the scope. This subtraction was most accurate with the oscilloscope on a fast time scale

($\sim 10\mu$s/div), so we observed the dump signals from the front and back sections of the plasma on separate scopes with each scope being triggered by the dump pulser that grounded the appropriate gate.

To acquire the signal entirely due to coupling in the vicinity of each dump, we turned the plasmas off by biasing the filament positive, and averaged over 25 scope acquisitions of the coupling signal. The charge signals were also averaged over 25 shots. Since there was 10-15% shot-to-shot variation on some plasmas, we made sure we started and stopped the acquisitions on both scope at the same times, in order to ensure that they both had averaged over the same set of plasmas.

Let us consider what we expect of the charge signals for a plasma that is cold and dense. As pointed out in Chapter 2 we expect the density along the plasma's axis to scale with the magnetic field strength. Yet the volume of the region sampled by the pinhole must be inversely proportional to the magnetic field strength, since the charge follows the field lines. Thus, for a cold, dense plasma, the total amount of charge collected from each section through the pin-hole must be very nearly equal.

In the case of a high-temperature, low-density plasma we expect the density to be essentially constant along the length of the plasma. This means that the charge signals observed through the pin-hole from the front and back of the plasma will be proportional to the volume sample from each section. The signal from the low-field end will then be greater than the signal from the high-field end by a factor equal to the ratio of the (spatially-averaged) magnetic field strength in each section.

Our experimental results confirm these expectations. We have created plasmas with varying densities, using the 'splitting' method, and graphed the ratio of the pin-hole charge signals from the low-field and high-field regions. This is shown in Figure 4.6, for the trap axial position that corresponded to a magnetic field ratio of ~ 2.1 in the two regions. The temperature of the plasmas remained ≈ 0.4 eV, even as the densities were varied. The predicted dependence according to Chapter 2 is also shown. We see that the ratio of signals varies from little more than 2 for low-densities plasmas to nearly unity for high-density plasmas.

The agreement between theory and data is less precise at the low-density limit. We do not have an explanation for this, at the present moment. It is quite possible that in this limit of low-collisionality (the densities are low), the experimental equilibrium is quite different from the theoretical case treated in Chapter 2 but it quite possible that the discrepancy is due to an effect of the splitting process itself, and may not reflect the actual plasma densities.

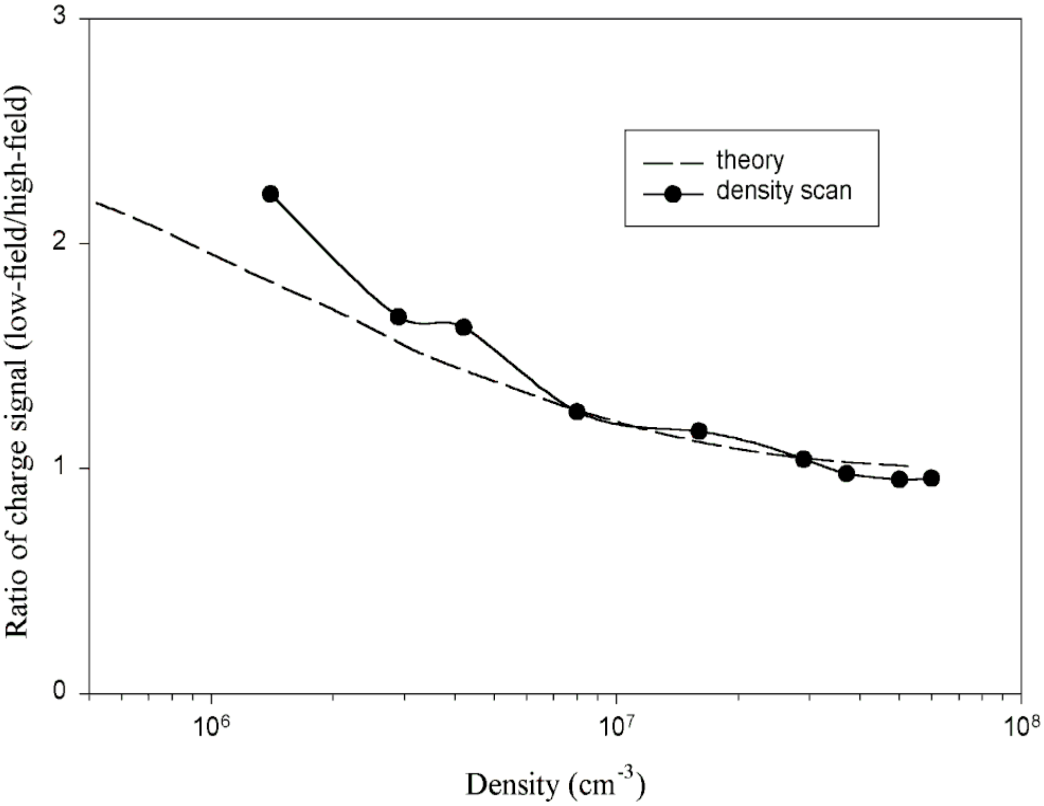

Figure 4.6: The density ratio in the two regions vs. plasma density. The temperature for all the plasmas remained ≈ 0.4eV. The prediction according to the global equilibrium theory of Chapter 2 is also shown for comparison

We also measured this density ratio by varying the temperature of the plasmas. However, as mentioned earlier it was not possible to change the temperature of our plasmas without affecting the density of the final plasma state. Since we were unable to take data by varying T, while holding n constant, we decided to parametrize our temperature variation data according to the ratio T/n. Hot, tenuous plasmas would have large values for this parameter, while cold, dense ones would have lower values. Our results for such a scan in temperature are shown in Figure 4.7, taken at the same axial position, with field ratio ~ 2.1. The horizontal axis is presented in convenient units.

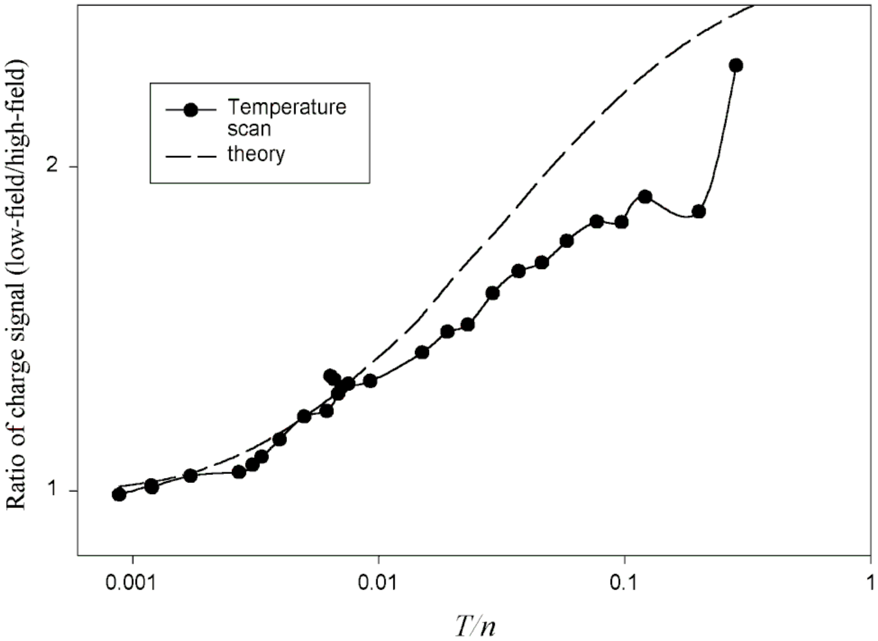

Figure 4.7: Experimental results of the pin-hole charge, from a range of plasma temperatures. The theoretical prediction is also shown for comparison

Once again, we have good agreement between theory and the data in the regime of cold, dense plasmas but they deviate considerably when the ratio T/n gets large, as it does for a hot (or low-density) plasmas. Of course, this is the limit where the collision frequency (due to the large T) is low and the plasma may not yet have reached the global thermal equilibrium state described in Chapter 2. The splitting process too may affect the measurement for hot plasmas, although at the moment, we have no consistent model of how this happens.

From our theory of Chapter 2 we expect that the behavior of cold, low-density plasmas will be equivalent to the behavior of hot plasmas of higher density; if two plasmas have the same value for T/n, then their equilibrium properties, such as the distribution of relative density must be the same. We can infer the volume charge densities in the two regions from our knowledge of the axial magnetic field profile. To recover the density in each region, we divide each signal by the value of the (average) magnetic field in that section. The results of both the density and temperature scan versus the parameter T/n are shown together in Figure 4.8. For reference, we also indicate the locations of two plasmas, at extremes of the parameter range. Also shown is a similar set of data from the trap in the other axial position, where the gradient is smaller, and the field ratio is ~ 1.2. The theoretical curves are also shown.

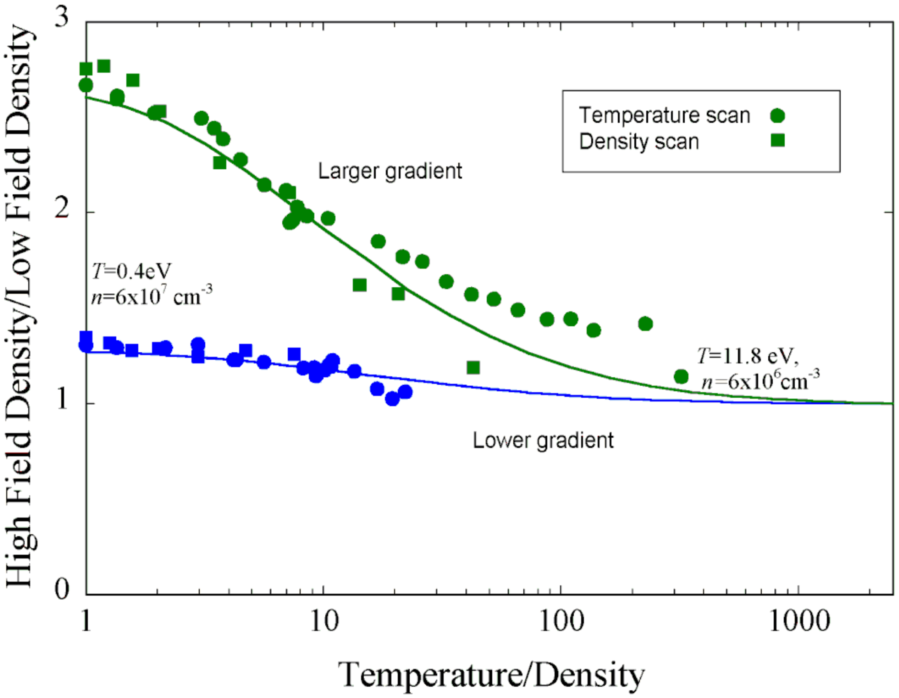

Figure 4.8: The ratio of the densities, as determined from the pinhole charge vs. T/n. The n and T values for two plasmas are also shown.

The agreement is very good for cold, high-density plasmas, that is, for plasmas with a low value for T/n. Here the ratio of the densities is essentially the ratio of the magnetic field strengths averaged over the two sections. As we go toward larger values of T/n, that is toward hotter and more tenuous plasmas the agreement between the theory and data is less precise, but the trend is definitely toward the ratio approaching unity.

We may speculate that a plausible reason for the less-than-perfect agreement between the data and our theory is that the plasmas we created were not in global 'shear-free' thermal equilibrium. This could mean that the angular frequency of the rotation of the plasma ω is not constant across the field lines, even if the values for this parameter were uniform along these lines. The mechanisms which causes the radial velocity profile to relax to the 'shear-free' state are not well understood, but it is expected to be mediated through electron-electron collisions. The collision frequency $\nu \sim n/T^{3/2}$, and the collisionality is reduced in the limit of low-densities and/or high-temperatures. It is possible that the experimental plasmas do not have a 'flat-top' distribution in ω. This would mean that the radial density distribution is not 'flat-topped' either, and the diamagnetic drift makes a substantial contribution to ω. Since our estimates of the density ratio depend on the assumption that ω is constant throughout the plasma, the experimental density ratios may then differ quite significantly from the theoretical case.

Why does this 'splitting' diagnostic yield sensible results ? Any section of the plasma is by itself a valid equilibrium configuration. Thus we expect the 'splitting' process to preserve the original properties of the equilibrium if it does not cause any gross rearrangement of the charge along the field lines. That the agreement between the theory and the data is surprisingly good leads us to believe that this may indeed be the case. The plasma is split by voltages on the gates G5 and G9 which drop to -80V from ground in less than a few microseconds. Both gates are relatively small (1" long each), and any charge contained in them would make only a small addition to the charge in the split sections. Ideally, we would like to drive this negative voltages as quickly as possible to split the plasma faster than any of the time scales that might rearrange the plasma charge in the split sections such that they are different from the distribution in the initial equilibrium. However, the speed of the HV pulsers are limited by the Tektronix PG505 pulse generators which are unable to ramp up to voltage faster than a microsecond. This time scale is comparable with the typical 'bounce' time of the electrons in the plasma - the time for an electron to travel across the plasma with its thermal velocity along a magnetic field line - the bounce time is 1μs for a 1 eV electron in a 40 cm long plasma. Yet the situation is better than at first appears; the space charge potential of the plasma, the potential at the center field line is never more -15 Volts, and the gates potential needs to be only of this order to split the plasma. The splitting gates may achieve this potential in less than the bounce time, preventing any substantial rearrangement of charge along the length of the plasma. Note that the splitting does occur faster than the rotation time for the plasma about its axis; for a 5×10^7 cm^{-3} plasma in a 2 Tesla field, for example, this time is about 30 μs.

Another point of concern is that the splitting of the two sections does not occur equally because there is necessarily a potential variation along the axis of the plasma. For a cold plasma this potential difference is $T \ln(\eta)$ (η is the mirror ratio), and is typically less than 1 Volt. This variation is much less than the space charge potential of these plasmas $\sim$ 10 V. For hot plasmas, the density variation along the axis is small, and the potential variation is also substantially smaller than the plasma space charge potential.

4.4 The Line Charge density

Another method of diagnosing the equilibrium of an electron plasma in an axially varying field is measuring the variation of the total line charge density of the plasma along its length. Except for the end gates, the gates of the trap which confine the plasma are at ground potential. Since these cylindrical conductors stay at ground through the entire hold period, Gauss' law for electric fields requires that the presence of a (charged) plasma within them must be balanced by an equal amount of charge (of opposite sign) that flowed into the conductor from ground. When the plasma in the interior is dumped, the charge in the conductor returns to ground, and the resulting voltage across the cable capacitance can be observed on an oscilloscope. We can measure the amount of this charge for each gate and this provides us with an experimental measurement of the line-charge density of the plasma along its length.

The measurements were performed by attaching each gate to a cable which led to a scope. We measured the capacitance of each gate, with the (same) cable attached, by placing it in series with a known capacitor and measuring the voltage across the cable+gate combination, with a fixed amplitude sinusoidal signal being fed across the ends of both capacitances. The gates, along with their internal wiring within the vacuum chamber, usually had a capacitance of a few hundred pf; the capacitance in the measurement was dominated by the over 30 feet of 30 pf/ft BNC cable that ran between the chamber and the oscilloscope. (Almost all our electronics was located in room different from the one with the superconducting magnet and experiment; the scopes would not be able to operate in the high-magnetic field-hence the long cable length). Knowing the capacitance of the cable+gate combination in each case allowed us to calculate the charge from the voltage signal measured on the scope.

We varied the plasma temperature and density as described earlier, and measured the charge on each gate, for each value of T and n. When a low-density plasma is dumped it becomes difficult to measure the voltage on the gates; the signal is barely visible above the noise. This problem becomes more pronounced when there is a substantial level of coupling between the dump gate and the gate on which the charge signal is being measured; this coupling often occurs between the wires leading to the gates, within the vacuum system, and can be substantial even if the gates themselves are not near each other. As the dump gate is switched to ground from -80 Volts, the coupling on nearby gates can overwhelm the much smaller signal generated by plasma exiting the gates.

We devised a method to reduce the level of this coupling when the signal is observed on the scope. This coupling signal is proportional to the voltage switching signal on the dump gate, that is, it has the same time structure. We built a circuit that takes the signal obtained by inverting the output of the pulser which drives the dump gate and feeds it to the same input of the preamplifier that also looks at the actual gate signal. To observe only the coupling level on the scope we turned off the plasma, by biasing the filament positive. We looked at the output of the amplifier on the scope, which is a sum of the coupling signal from the gate and the inverted signal coming directly from the pulser. Using our circuit we were able to (smoothly) adjust the gain on the inverted signal fed into the input until it cancels out the coupling signal from the gate, fed into the same input. When this pure coupling signal has been eliminated we start producing plasmas again, to see the effect due to the charge alone. We continue to use digital background subtraction to eliminate any residual effect of the coupling on the total signal.

This technique allows us to measure charge signals on the scope that are much

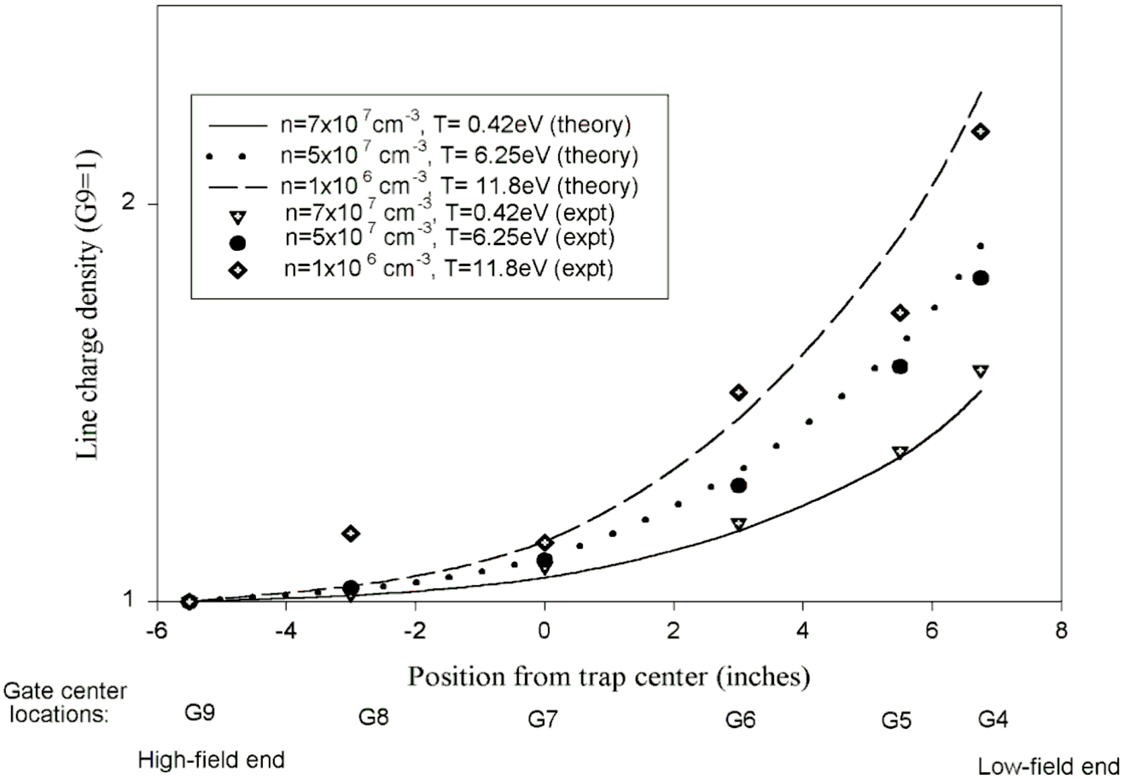

Figure 4.9: Relative line charge density across the trap for plasmas at various temperatures (and densities). The theoretical (spline-fit) curves are also shown for comparison.

smaller than the coupling level; this makes possible observations of plasmas with very low density, in the 10^5 cm^{-3} range.

Our experimental observations of the the line-charge for plasmas with various values for the density and temperature are shown in Figure 4.9 and Figure 4.10. The trap axial position in the magnet bore corresponded to a field ratio across its length of ~ 2.1 .

We can see that the experimental measurements of the line-charge density are in reasonable agreement with the theoretical curve fits. As we mentioned earlier, it is likely that ω is not constant across the field lines, a requirement for the theoretical model, and this may explain some of the discrepancies observed.

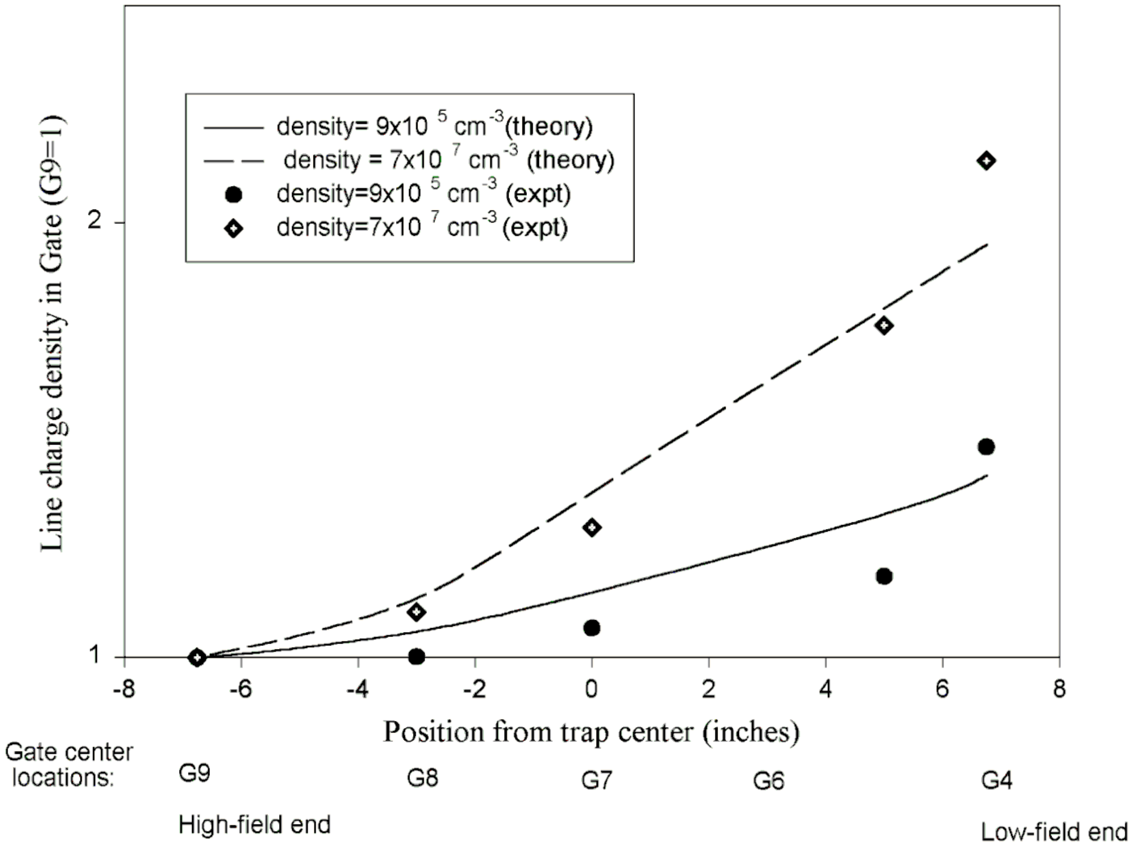

Figure 4.10: Relative line charge density across the trap for plasmas at the same temperature ≈ 0.4eV, yet at different densities. The theoretical (spline-fit) curves are also shown for comparison

4.5 The Radial Profiles

The pin-hole can be moved in a line perpendicular to the trap axis, so we are able to measure the charge collected through the hole at various points along this line, thus measuring the radial density profile of the plasma. If the plasma is dumped in sections, as it is in the 'two-split' experiment, we can simultaneously measure the radial profiles of both sections. The pin-hole is located in a region where the magnetic field is much smaller than the maximum axial value, so the plasma expands as it leaves the trap. Such a map is shown in Fig. 4.11

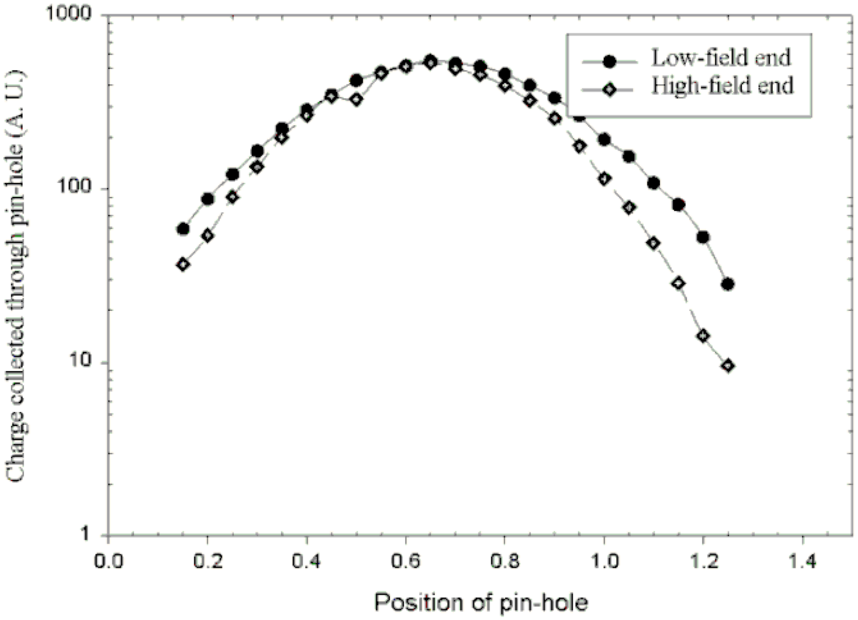

Figure 4.11: The radial profiles of two sections. lo-field density n=4x10$^7 cm^{-3}$, T =0.4 eV

We can recover the actual density profiles of the plasma by scaling the profile measured by the pin-hole by $\sqrt{B}$. If the plasma profile were to follow the magnetic field lines across the low- and high- field regions then the two profiles shown in Fig. 4.11 would fall upon each other; however, it is clear that the profile of the high-field section is narrower, and falls to zero from its central value faster than the profile of the low-field region. We have presented the data on a semi-log plot to better emphasize the difference between the profiles. This demonstrates that the plasma is smaller in radius in the high-field region than would be obtained by following the magnetic field lines from the low-field region. Also the scale length of density fall-off, the Debye length, is smaller in the high-field profile, indicative of the greater density in that region.

In the axial trap position chosen for the measurements in Figure 4.11, the ratio of the (averaged) fields in the high-field and low-field regions is 1.35. For the plasma parameters shown, the ratio of the low-field radius to the high-field radius is about 1.25. This is larger than the ratio ≈ 1.1, inferred from Figure 4.11. We have no explanation for this discrepancy other than that the plasma may not have reached global thermal equilibrium, and that ω may not be constant across all the field lines. (It also appears that the 'center' of the high-field radial profile does not coincide with the center of the low-field profile. A plausible explanation for this is that the high-field (and low-field) sections of the plasma may be slightly displaced from the trap axis during the splitting process. When the two sections are dumped, they follow the magnetic field lines out of the trap and arrive at slightly different positions on the charge collection diagnostic.

Chapter 5

Diocotron oscillations in an Axial Field Gradient

5.1 Introduction

Perhaps the simplest and most commonly studied collective mode in a pure electron plasma is the $m = 1$ diocotron mode oscillation. In this mode, the plasma's rod of charge revolves around the trap axis. When the plasma rod of charge is displaced from the axis of the grounded conductors of the trap, it interacts with the electric field of its image charge on the trap walls, which together with the axial magnetic field B, causes the plasma to ExB drift about the trap axis. In conventional Penning-Malmberg traps, with an axially uniform B this mode is very stable, lasting for $\sim 10^5$ cycles or more, without growth or decay [36]. The frequency of the mode is proportional to the line charge density of the plasma, and inversely proportional to the magnetic field strength.

We have found that diocotron-like oscillations persist in our traps, over ~ 1000 cycles, even with a substantial axial gradient in the magnetic field. This is surprising surprising, since we might expect the plasmas to smear out azimuthally on a much shorter time scale.

In this chapter, we first provide some background on the $m = 1$ diocotron mode in electron plasmas. Then, we describe our experimental observations of long-lasting modes in our trap with an axially varying magnetic field. Lastly, we discuss a plausible explanation for why this mode survives for an unexpectedly long time.

5.2 The $m = 1$ mode

Azimuthal surface waves on a cylindrical plasma in a Penning trap take the form $\delta r \propto \cos(m\theta)$. For $m = 1$, this wave is accurately described as the bulk displacement of the plasma from the axis of the trap. Since the plasma is in a conducting cylinder, it sees the radial electric field of its image charge on the wall, and performs ExB drift motion about the trap axis. This is shown in the axial view of the trap in Figure 5.1

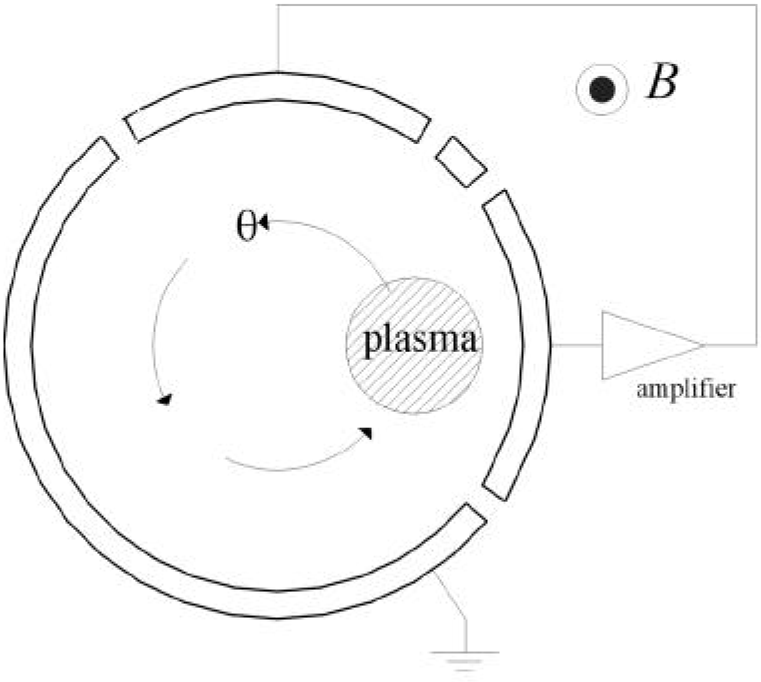

Figure 5.1: The $m = 1$ diocotron mode

For small displacements of the plasma from the trap axis, the angular frequency of (an infinitely long) plasma revolving about the trap axis can be shown to be [36]

$$\omega_d = \frac{2ec}{B}\frac{\pi n {r_p}^2}{{r_w}^2} \tag{5.1}$$

In this calculation the plasma, and its image on the wall, are treated as line charges with the same linear charge density, a model that works well even for larger displacements (greater than the plasma radius r_p) from the trap center. The mode frequency is proportional to the line charge density of the plasma, and inversely proportional to the magnetic field strength.

The diocotron mode is typically diagnosed by observing the signal on the azimuthal sectors on the gates, as shown in Figure 5.1. When the plasma is near one of the sectors, the capacitance of the sector produces a voltage relative to ground; this voltage may be amplified and observed on a scope. As the plasma revolves around the trap axis, the voltage signal appears as a sine wave at the diocotron frequency. The frequency of this sinusoid gives us the line charge density of the plasma. The $m = 1$ mode is a non-destructive diagnostic of the total charge in the plasma [22]. As the plasma gets closer to the wall, the motion becomes more non-linear and higher harmonics appear on the sector signal.

The diocotron mode may be grown and damped out by using feedback, as first demonstrated in [36]. In Figure 5.1 if the signal from the sector is amplified and fed to the other sector placed at 90^o to it, it produces an electric field which (along with the B field) causes the plasma to drift radially outward, increasing the mode amplitude. If the input signal is inverted before amplification it has the opposite effect and causes the mode to be damped. By using such feedback, the mode amplitude can be adjusted to the desired level.

Without feedback, the diocotron mode remains neutrally stable, lasting for $\sim 10^5$ cycles or more [36].

5.3 Diocotron oscillations with an axial gradient in B

When a plasma is displaced off-axis in a trap with a uniform axial B field, its charge per unit length remains constant along its length. From Eq. 5.1, this means that any section of the plasma revolves around the trap axis at the same frequency,

ω_d, and the plasma stays together over many cycles. Further, all the plasma electrons zip to and fro between the trap ends at the bounce frequency ω_b, which is much faster than the diocotron frequency. The electrons 'bounce-average' their azimuthal drifts across the entire length of the plasma, ensuring that all the particles experience the same motion in the θ direction over time.

If the axial magnetic field B varies along the plasma length, however, it is not obvious that the plasma should stay together as a coherent structure over many cycles. We may assume that the off-axis plasma, for small displacements, may be approximated by the on-axis equilibrium described in Chapter 2. For a cold, high-density plasma, the line-charge density in the high-field region is less than the line-charge density in the low-field region (For a mirror ratio of 2, for example, this ratio is usually between 0.5 and 1). Since the diocotron frequency is directly proportional to the line-charge density of the plasma, and inversely proportional to the magnetic field strength we may expect that the high-field end of the plasma will drift at slower rate, causing the the low-field end to move ahead in θ position. We also expect (from the description of the on-axis equilibrium) that there are trapped particles at either end of the plasma, and that bounce averaging will not work for a substantial fraction of the plasma particles. It may seem then that the displaced plasma should smear out in azimuth over a few diocotron cycle times.

Such a smearing out, in fact, is not observed until much longer, and the plasma maintains its integrity and continues to orbit around the trap axis for more than ~ 1000 cycles. We have observed such long-lived oscillations in three different axial positions of the trap in the solenoid magnetic field; the three positions produced different gradients across the trap length. To diagnose these diocotrons we have measured the frequency of the oscillations on the sectors.

We made these observations on cold plasmas ($T \approx 0.7$eV), with low-field densities about 6x10^7 cm^{-3}. The plasmas were trapped in the length of the trap between G2 and G12. The high-field end plasma radius was ≈ 0.3 cm. Since the plasmas were always injected slightly off-axis, there was an observable diocotron from the very beginning of the hold period. The displacement of the plasmas from the trap axis remained less than the plasma radius r_p.

In Figure 5.2,we show the variation of the diocotron amplitude with time for the three different axial positions. The ratio of the fields at the *ends* of the trap in these positions was 1.4:1, 3:1 and 5:1 and we can call them respectively, the ‘low-gradient’, ‘medium gradient’ and ‘high-gradient’ positions. A qualitative understanding of the results in Figure 5.2 is easy; the diocotrons last longer in smaller gradients. The frequency of the diocotrons was typically $\approx$ 3 kHz; the mode of the plasma in the entire length of the trap survives for between few hundred to nearly 1000 cycles, depending on the gradient across it.

The damping of the diocotron due to the gradient in the magnetic field did not appear to be affected by the trap pressure. The diocotrons seemed to last just as long with the trap cold, where the ambient pressure would be lower, as they did without any cooling.

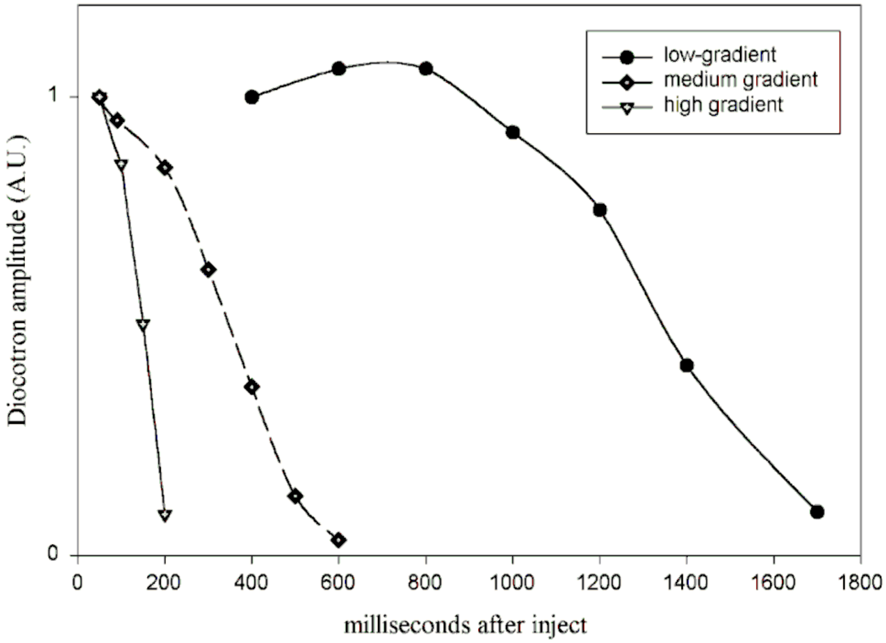

Figure 5.2: The decay of the diocotron signal at three different axial positions of the trap

We also split the plasmas in two, soon after they are created, by applying a -80 V bias to G7, which is located in the middle of the trap. (See Fig. 4.5) One of the sections is, of course, in a higher average field than the other. The diocotrons on the

G2-G7 section were observed through the sector on G3, and the G7-G12 section was seen on the sectors on G11. The results are shown in Figure 5.3 and Figure 5.4 for the case of the 'medium-gradient' and 'high-gradient' region, respectively.

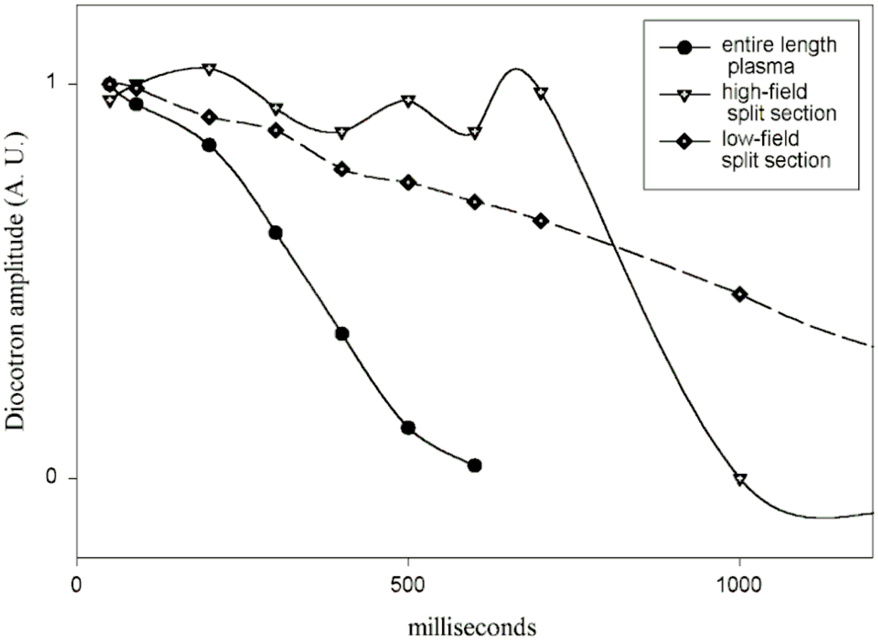

Figure 5.3: The dioctron signal amplitude for the unsplit plasma and the two split sections. The axial position of the trap corresponded to 'medium-gradient'

We can see that the shorter split sections last considerably longer than the full-length plasma, in both gradient levels. This makes sense because it is simply much harder to keep a long plasma coherent than a short one, the change in the drift velocity being greater over a long plasma. The split sections last for ~ 1 second, and so survive more than ~ 1000 cycles.

We present in Table 5.1 the measured frequencies of the diocotrons, before and after the splitting occurs.

The diocotron frequency formula given by Eq. 5.1 is for the axis of an infinitely long rod of charge, and does not include finite-length effects that produce a slightly different measured frequency. As described in [37], the mode frequency of a finite length plasma is greater than the frequency predicted by Eq. 5.1, the difference de-

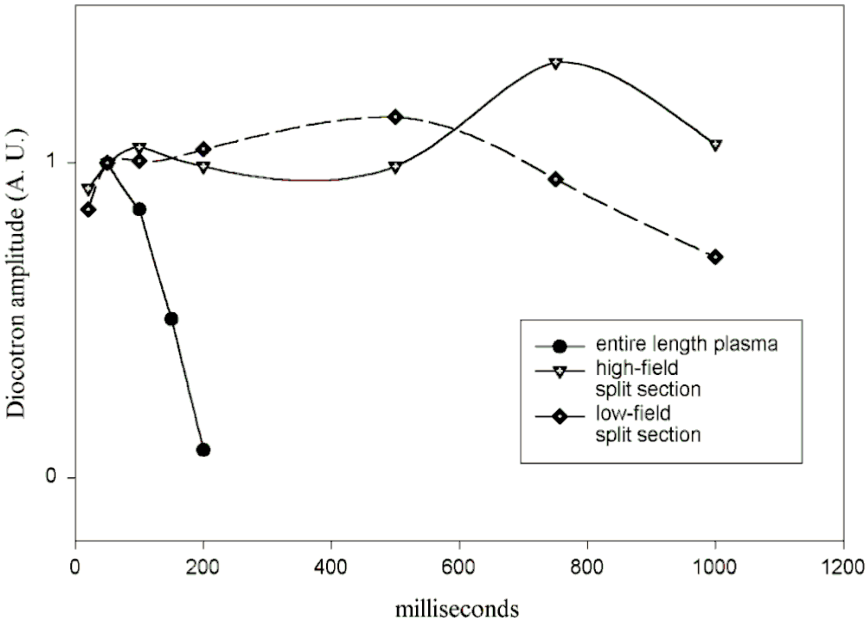

Figure 5.4: The diocotron signal amplitude for the unsplit plasma and the two split sections. The axial position of the trap corresponded to 'high-gradient'

Gradient	Field Ratio	Unsplit	Split Hi	Split Low
low	1.4:1	2.56	2.77	3.45
medium	3:1	2.77	2.38	4.25
high	5:1	3.03	0.96	3.85

Table 5.1: The measured frequencies (in kHz) of the diocotron mode for various axial positions of the trap, before and after the plasmas are split.

pending on the ratio of the trap wall radius to the plasma length, r_w/L_p, and the plasma radius to the wall radius, r_p/r_w. We have made such corrections to our measured frequencies to estimate a 'diocotron frequency' that corresponds to Eq. 5.1, which assumes no finite length effects. The values, corrected to eliminate finite length effects, are shown in Table 5.2.

We assume that since we had diocotrons with small amplitude their charge distribution was similar to that of an on-axis plasma. So we are able to estimate the variation of the line charge density of the plasma across its length. For the plasmas we considered this ratio (depending on the trap axial position) was in the range 0.65-

Gradient	Field Ratio	Unsplit (corrected)	Split Hi (corrected)	Split Low (corrected)	Weighted Avg.
low	1.4:1	2.32	2.13	2.87	2.45
medium	3:1	2.52	1.98	3.54	2.71
high	5:1	2.75	0.80	3.21	2.3

Table 5.2: The diocotron frequencies (in kHz) of the unsplit plasma, and its split sections, after correcting for the finite length effects. The weighted average of the frequencies in the two section is shown in the last column.

0.85. The high-field section of the plasma would have a lower frequency both due to the higher field magnitude and the lower line charge density.

In our analysis, we have taken the frequencies of the two sections (corrected for finite length effects), and then calculated their average, weighting them appropriately to include the variation of the line charge density as predicted by the theory of Chapter 2. If ω_L and ω_H were the frequencies of the split sections in the low-field and the high-field, and λ_L and λ_H the (z-averaged) line-charge densities, then the weighted average would be given by

$$\overline{\omega} = \frac{\lambda_L \omega_L + \lambda_H \omega_H}{\lambda_L + \lambda_H} \tag{5.2}$$

In Table 5.2 we show the frequencies corrected for the finite length effects, and in the fifth column, the weighted average of the two sections, according to Eq. 5.2.

We can see from Table 5.2 that agreement between the weighted average and the 'corrected' diocotron frequency of the unsplit plasma is good to within $15 - 20\%$.

This suggests that when a diocotron mode exists in a trap with an axially varying magnetic field, the plasma particles are bounce averaging their azimuthal drifts across the length of the plasma, so that the plasma moves as a coherent whole for many diocotron cycles. The relative line charge densities may be used as a rough estimate of the fraction of time spent by the typical plasma particle in each section.

How does this bounce averaging come about? We expect that a plasma displaced slightly off-axis will also have trapped particles at either end, much like the on-axis equilibrium of the plasma. However, we believe that since there is a tendency for the low-field end to revolve faster around the trap axis than the high-field end this equilibrium is perturbed enough that the trapped particles are untrapped and are able to allow the bounce averaging mechanism to continue. The particles are trapped in the high-field region by a potential difference that tends to keep low-energy particles in that end. If the low-field end moves slightly ahead of the high-field this potential difference (of order T) may be reduced or reversed slightly to cause particles to become untrapped and bounce average through the entire length of the plasma. Similarily, the tendency of the low-field end to get ahead of the high-field end will perturb it enough that its particles are no longer reflected back by the space charge of the high-end.

There is another mechanism that also helps preserve the plasma's integrity. If one end of the plasma begins to lag behind the other end in azimuth (the θ direction), then the particles from that end will begin to smear out behind the leading end, as the particles will bounce back and forth along the field lines. However, we have to consider that even as the plasma revolves around the trap axis, it also rotates about its own axis on a much faster time scale. Thus any particles from the high-field end that have smeared out behind the low-field end will be 'wrapped around' to the front of the low-field end in a time that is much shorter than the diocotron period. On average these particles do not lag behind the bulk plasma. The scheme for this mechanism is shown in Figure 5.5, where we are looking down the axis of the plasma from the low-field end.

The latter mechanism will not be effective if a substantial fraction of the particles at either end are trapped. It is possible that the charge distribution of the plasma is modified according to the first mechanism to allow bounce averaging to happen, while the second healing mechanism 'wraps' the plasma around on itself so that it does not spread in azimuth.

Even though the diocotron mode persists for a long period, we surmised that the low-field end of the plasma might be slightly ahead of the high-field end in azimuthal position. We have no estimate of the value of this phase lead between the two ends, but devised a method of looking for this effect, if it existed in a measurable amount. We compared the diocotron signals on the sectors of gates G3 and G11, located at opposite ends of the trap, looking for a noticeable phase difference between the two sinusoidal signals as observed on a scope. There will always be an instrumental phase

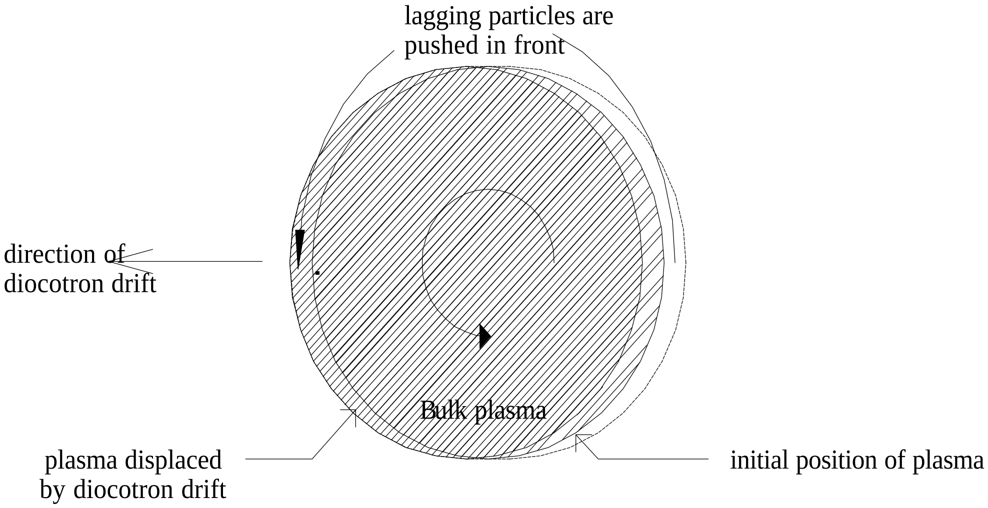

Figure 5.5: The ‘healing mechanism’ for the plasma. The particles that are lagging behind from the high-field end, are ‘wrapped around’ to the front of the low-field end in half a plasma rotation time.

shift between the two sector gate signals because they were not aligned perfectly with respect to each other, an offset that must be subtracted out to reveal any real effect. We arranged to account for the misalignment by reversing the magnetic field direction of the solenoid for the trap. In principle, this reverses the direction of the(ExB) diocotron drift, and the sign of a real phase difference would be reversed. The sum of the phase shifts measured on the scope from the two field directions would give us the value of the real phase angle lag. Although we got this technique to work reasonably well, we saw no consistent difference in the θ position of the plasma at the two ends. Any effect, if it existed, was certainly less than a few degrees, the resolution of our diagnostic.

5.4 Magnetic Pumping

When an axisymmetric magnetic field has a gradient along its axis, the Maxwell equations require that the magnetic field strength also vary slightly as function of radius at a given axial position. We have demonstrated that even with substantial axial gradients there exist diocotron oscillations that are quite long-lived. As pointed out earlier, the plasma rotates about its own axis even as it revolves about the trap axis at a slower rate. The effect of this rotation in a trap with an axial field gradient is that the electron plasma fluid is advected through regions of varying magnetic field strength. We suggest that this should lead to the phenomenon of ‘magnetic pumping’, analogous to the experimentally observed ‘rotational pumping’ in the electron plasmas at UCSD [38]. We discuss the mechanism behind magnetic pumping and its significance in Appendix B.

Chapter 6

Further Work

6.1 Introduction

The Cryogenic Electron Trap, as described in Chapter 3, was constructed with the intention of studying electron plasmas at very cold temperatures, in an axially varying magnetic field. Although no cryogenic plasmas were studied for this thesis, they will be integral to future research on this trap. In this chapter we will describe some of the novel phenomena that are exihibited by these plasmas, while suggesting the possibilities for further study.

When a pure electron plasma is cooled to low temperature in a strong magnetic field it enters the 'strongly magnetized regime'. This regime is characterized by an exponential decrease in the anisotropic temperature equilibration rate. The physics behind this steep decline is discussed in this chapter. When the electrons cool to cryogenic temperatures, they populate the lowest quantized cyclotron orbits, or Landau levels. The separation between these energy levels is equal to the energy required to flip the intrinsic spin magnetic moment in the external magnetic field. Therefore, this is a regime where the electron-spin is expected to have observable effects. Chen and Dubin have calculated the equilibration rate of spin-temperature in a cryogenic 'strongly-magnetized plasma'. This has motivated many ideas for experiments that involve consideration of the electron's spin in the collisional dynamics of the plasma electrons. We will discuss some of these ideas in this chapter, providing a background for the description of the Spin experiment in Appendix A.

Plasma physics has perhaps been the one realm of modern physics where quantum mechanics has historically been irrelevant. This situation may be about to change since Planck's constant finds a natural place in the study of the 'extreme' plasmas discussed in this chapter.

6.2 Strongly Magnetized Plasmas

Electrons performing cyclotron motion in a magnetic field, radiate away their perpendicular kinetic energy in cyclotron photons. As the parallel temperature of the plasma electrons $T_{\|}$ equilibrates with the cooled perpendicular temperature $T_{\perp}$ the entire pure electron plasma can cool and come into thermal equilibrium with the walls of the trap, which can be be cooled by liquid helium, for instance, to 4.2 K. This cooling mechanism was discussed theoretically in [39], and has been observed experimentally in [29]. For a sufficiently strong magnetic field the time-scale to cool to near the wall temperature ($\approx$ 1.6s for a 3 Tesla field), is much smaller than the plasma lifetime .

As the plasma cools, it enters a regime where the typical cyclotron orbit radius r_c becomes smaller than the typical distance of closest approach $b = e^2/T$ between two colliding electrons. When the ratio $\epsilon = r_c/b \ll 1$ the plasma is said to be in the 'strongly-magnetized' regime [40]. Since $r_c \propto T^{1/2}/B$, $\epsilon \propto T^{3/2}/B$, this regime is achieved only with strong magnetic fields and low plasma temperatures. (Typically $B > 1$ Tesla and $T < 100K$). Even for a magnetic field as high as 10 T, the temperature has be much lower than 0.1 eV for the plasma to be 'strongly-magnetized'; at these low temperatures a neutral plasma will have recombined. Therefore, the novel physics of this regime is not relevant to typical neutral plasmas in the laboratory and is only observed in pure electron plasmas.

The most remarkable feature of the 'strongly-magnetized' regime is the sharp decrease in the anisotropic temperature equilibration rate in these plasmas. The theory of the collisional dynamics of such a weakly-correlated plasma was worked out by Hjorth and O'Neil in [41], and a more comprehensive numerical treatment is included in [42]. We describe the basic physics here.

Equilibration between $T_\parallel$ and $T_\perp$ occurs through the energy exchange between these degrees of freedom when electrons collide with each other. The total perpendicular kinetic energy of two colliding electrons is conserved through the magnetic moment adiabatic invariant (the magnetic moment is proportional to $E_\perp/B$). The perpendicular motion must be perturbed at a frequency higher than the cyclotron frequency for the invariant to be broken and for energy exchange to occur between the parallel and perpendicular motions of the colliding electrons. When the plasma is 'weakly-magnetized' i.e. when b is typically smaller than r_c, most collisions between electrons cause a breaking of this adiabatic invariant, and parallel and perpendicular degrees of freedom can equilibrate efficiently. However, when the plasma is strongly-magnetized, this is no longer possible. As shown in Figure 6.1, typical collisions between electrons occur such that $b \gg r_c$ which means that $v_{th}/b \ll v_{th}/r_c$, or $v_{th}/b \ll -_c$, the cyclotron frequency (v_{th} is the electron thermal velocity). The typical collision produces electric fields with characteristic frequencies much smaller than the cyclotron frequency. Thus each (typical) collision causes only an exponentially small breaking of the magnetic moment adiabatic invariant; and only collisions with the (exponentially) small number of electrons in the Maxwellian tail of the velocity distribution can cause a substantial breaking of the magnetic moment invariant. Equilibration, therefore, occurs over an exponentially long time scale.

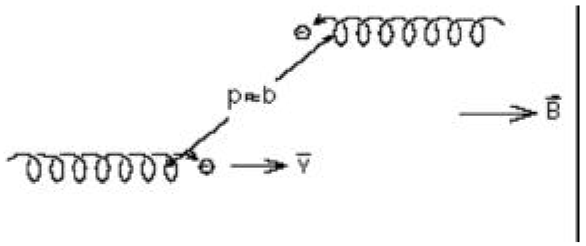

Figure 6.1: Electron-electron collision in a strong B field

The decrease in the equilibration rate was experimentally observed by Beck, Fajans and Malmberg. These measurements agree well with the theory in [41] and [42] and are reported in [1]. The results are reproduced in Figure 6.2

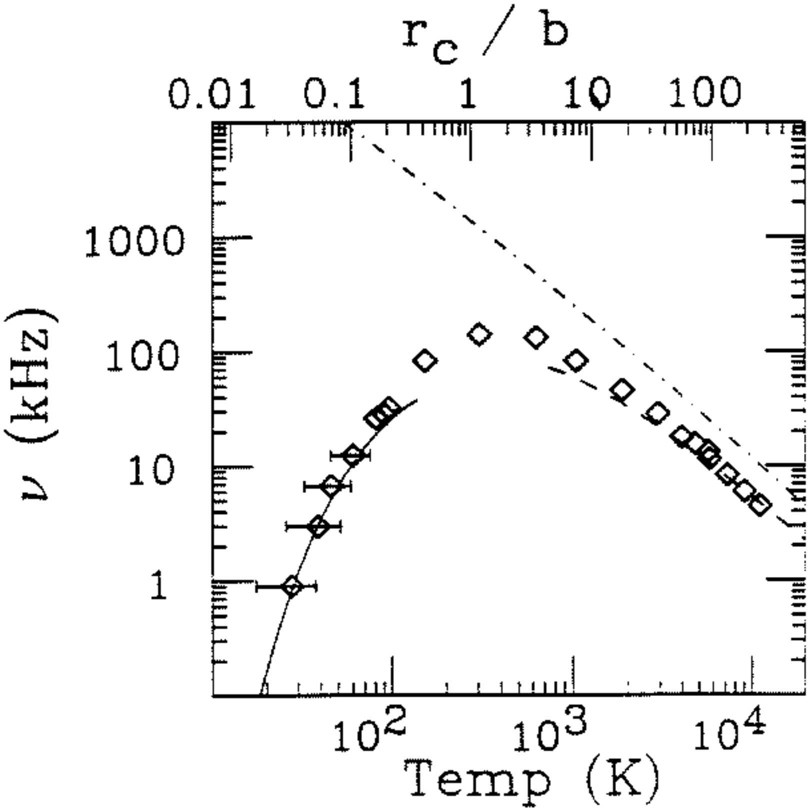

Figure 6.2: The measured anisotropic temperature relaxation rate for B=6.1 Tesla from [1]. The mean density was 8x10^8 cm^{-3}. The strongly magnetized data is on the left. The theory is shown for comparison.

6.3 Electron-spin in cold plasmas

At low trap temperatures and strong magnetic fields the electrons cool to the lowest quantized cyclotron orbits, or Landau levels. The cooling rate, proportional to B^2, is well described by the classical Larmor formula for electric dipole radiation, slightly modified at low temperatures when quantum effects become significant [29].The energy levels are given by

$$E_{n_L} = 2\mu_B B(n_L + \frac{1}{2}) \tag{6.1}$$

where $n_L = 0, 1..$ and μ_B is the Bohr magneton. At $T \approx 4K$ and $B \approx 3$ Tesla the thermal energy kT is comparable to the energy difference between these levels. The intrinsic spin magnetic moment of the electron is $(g/2)\mu_B$, which, since $g = 2.002..$, is very nearly μ_B. The energy of spin-flip in the magnetic field is then very nearly $2\mu_B B$, the energy difference between the Landau levels. Therefore, at low temperatures and strong fields one expects electron spin-dependent effects in the plasma.

At high temperatures the electron spins point parallel or anti-parallel to the magnetic field in equal proportion. As the plasma is cooled, more spin moments will tend to relax to the thermal equilibrium state where more moments are aligned parallel with the external magnetic field. Chen and Dubin calculated the equilibration rate of the spin-temperature, T_s, to the kinetic temperature. This equilibration rate is rather slow, even when compared with the $T_\parallel - T_\perp$ equilibration rate, but for a different reason.

The intrinsic moment of the electron, like any magnetic dipole, precesses about the magnetic field direction. To cause the spin of the electron to flip, it must be perturbed by a *magnetic* field perturbation with a frequency component resonant with the spin-precession frequency Ω_p. This field perturbation must be in the plane perpendicular to the precession axis, defined by local direction of the magnetic field $\mathbf{B}$. The spin-precession frequency $\Omega_p = (g/2)\Omega_c \approx 1.001\,\Omega_c$, where Ω_c is the cyclotron frequency. As an electron gyrates in the magnetic field (See Fig. 6.3) at the cyclotron frequency, an axial variation in the field will produce in the electron's rest frame a perturbation $\delta\mathbf{B}$ which rotates in the perpendicular plane at Ω_c, as shown in Figure 6.4

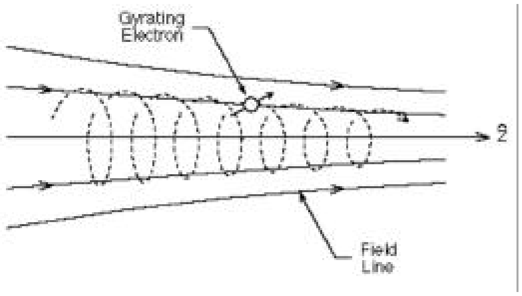

Figure 6.3: Electron gyrating in an axially varying magnetic field

Although $\Omega_c \approx \Omega_p$, the difference between them is still large enough that spontaneous coupling between the perpendicular orbital motion and spin precession remains impossible. However, a close collision with another electron in an non-uniform **B** field can perturb the cyclotron motion enough to produce frequency components which can drive a resonant spin-flip. Therefore, to produce coupling between the perpendicular kinetic temperatures and the spin-temperature of the electrons, we require close collisions between electrons in a non-uniform **B** field.

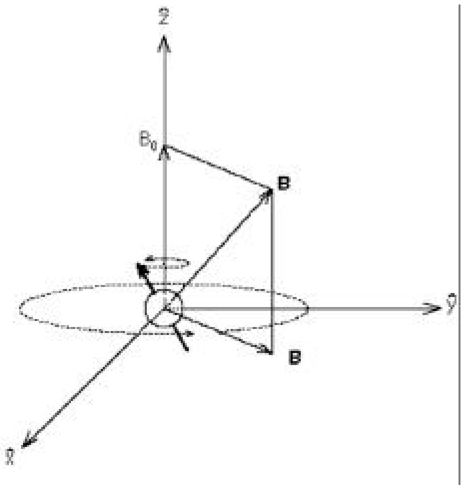

Figure 6.4: The magnetic field perturbation in the electron rest frame

The equilibration rate between the spin-temperature T_s and the kinetic temperature is calculated exactly in [2], using time-dependent perturbation theory. Some of the main points of their calculation are mentioned here.

The electron's gyration in an axially inhomogeneous field produces, in its rest frame, a small time-dependent field $\delta\mathbf{B} \approx \mathbf{r(t)} \cdot \mathbf{B}$, where

$$\mathbf{r}(t) = r_c(\cos(- \;_c t + \theta)\hat{x} + \sin(- \;_c t + \theta)\hat{y}) \tag{6.2}$$

is the radius vector of the electron and $\theta = \theta(t)$ is used to include the time-dependence of a collision. It is this time-dependence that will add to the cyclotron motion to make $\delta\mathbf{B(t)}$ resonant with the the precessional motion at frequency $- \;_p$.

In the transverse (perturbation) field the spin rotates through an angle given by

$$\Delta\Theta \approx \frac{eg}{2m_e c}|\delta B_R|\Delta t \tag{6.3}$$

where δB_R is the resonant component of the rotating magnetic field perturbation in the electron rest frame, and $\Delta t \approx b/v_{th}$ is the duration of the collision. In time-dependent perturbation theory, the probability amplitude for a spin flip $|\Delta C|$ is equal to the angle precessed $\Delta\Theta$, where $\Delta\Theta \ll 1$. We may assume that the spin direction diffuses in a random walk and the spin depolarization rate is estimated as

$$\nu_{spin} \approx \nu_c |\Delta C|^2 \tag{6.4}$$

where $\nu_c = \pi n \bar{v} b^2$ is the 'large-angle' scattering frequency.

The depolarization rate equation

$$\left(\frac{d}{dt} x_-\right)_{coll} = \nu_{spin}(x_+ - x_-) \tag{6.5}$$

where the x's are concentrations of spin-up and spin-down electrons. The exact result is in [2]. We reproduce a plot from this reference showing the depolarization rate as the function of the parameter ϵ, the ratio of the typical Larmor radius r_c to the distance of closest approach b in the plasma, which is less than unity for such 'strongly-magnetized' plasmas. The rates due to other depolarization mechanisms are also shown for comparison in Figure 6.5.

We can estimate from Figure 6.5 that in a typical plasma, say with density 10^7 cm^{-3}, $T = 10K$, in magnetic field 3 Tesla with scale length 10 cm, the typical spin-flip time is about 100 seconds. Since this is less than the typical lifetime of such plasmas, we may be able to conceive of two experiments to observe this spin-flip rate.

If the plasma were cold enough ($T(K)/B(\text{Tesla}) \leq 1$), then a substantial fraction of the spins would tend to align themselves with the magnetic field in thermal equilibrium. By measuring the polarization of an (initially) unpolarized plasma after sucessively longer hold times, we can observe the approach to thermal equilibrium. Alternatively, we can start with a polarized plasma, produced by a polarized electron source, and measure the relaxation to the equilibrium distribution.

The interaction energy of the spin magnetic moment with the external field $-\mu_s \cdot \mathbf{B}$ acts an effective potential for the electrons along a magnetic field line. (By convention, the spin direction of an electron is antiparallel to that of its intrinsic magnetic

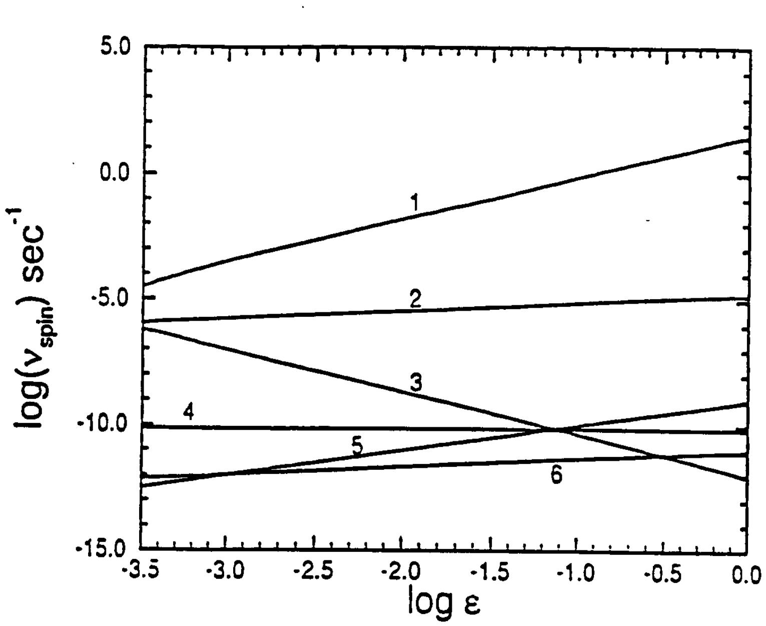

Figure 6.5: The spin depolarization rate as a function of $\epsilon = r_c/b = 10^{-3}T^{3/2}/B$ for different processes. (1)collisional depolarization in a nonuniform magnetic field. (2) spin exchange effect during electron-neutral collisions. (3) Thomas precession (4) spontaneous magnetic dipole radiation (5) spin-flip due to mutually generated magnetic field. (6) spin flip due to electron-neutral collision in a nonuniform magnetic field. The electron density is assumed to be 10^7 cm^{-3}, the neutral density is taken to be 10^4 cm^{-3}; the magnetic field is 1 Tesla and the scale length of magnetic field inhomogeneity is taken to be 10 cm. This plot is reproduced from [2]

moment) It has been suggested in [2] that if there is axial gradient in the field, then as the spatial distribution of electrons thermalizes along each magnetic field line, the 'down'-spins collect in the region of larger magnetic field while the 'up'-spins move to the region of lower field, provided that the parallel kinetic temperature $kT_{\|}$ is less than $\mu_s \Delta B = \hbar\Delta\text{-}_{p}$. Here ΔB is the difference in the field magnitude across the plasma length. This would cause either end of a cold plasma to get polarized, the degree of polarization depending on $T_{\|}$, and ΔB.

The experiments described above may be attempted on the apparatus described in the appendix on the Spin Experiment.

6.4 Extraction of polarized electrons from an unpolarized plasma

The energy levels of cold electrons in a magnetic field are shown in Figure 6.6. We suggest that the magnetic moment of the electrons, associated with the orbital motion in the Landau levels, may be obtained by dividing the energy (given by Eq. 6.1) by B

$$\mu_{n_L} = 2\mu_B(n_L + \frac{1}{2}) \tag{6.6}$$

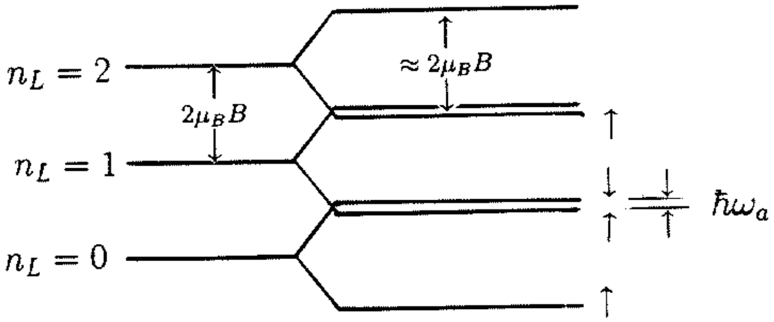

Figure 6.6: Energy levels of an electron in a magnetic field. The orientation of the spin-moment relative to the **B** is shown at right

In the lowest Landau level ($n_L = 0$), the magnetic moment associated with the orbital motion of the electron is then the Bohr magneton μ_B, and is always pointed anti-parallel to the magnetic field. The intrinsic spin magnetic moment of the electron is $g/2\mu_B$, which, since $g = 2.002..$, is very nearly μ_B. Each Landau level is split into two further levels, depending on the orientation of the spin magnetic moment in the external field $\mathbf{B}$, as shown in Figure 6.6. There is a small energy difference, equal to $2\hbar\omega_a = (g-2)\mu_B B$ between the energy split of the spin orientations, and the energy split of the Landau levels. This is shown in Figure 6.6, although not to scale.

We have noticed a remarkable fact about the electrons in the ground state. Since $(g-2)/2 \approx 0.001 \ll 1$ the electrons in the lowest Landau level, with spin moment pointing parallel to the magnetic field, have a (nearly) zero total magnetic moment. These plasma electrons would not be reflected by a magnetic mirror field, and we suggest that this property can be exploited to separate them from the rest of the electrons in the plasma, creating a polarized beam of electrons. All electrons above the ground state have a total magnetic moment that is at least $2\mu_B$, pointed anti-parallel to the field, and will be reflected in a magnetic mirror. We envision having the trap axial magnetic field increasing in the direction away from the plasma in the dump gate region, creating a magnetic mirror there. As the negative potential of the gate is raised to ground, almost all the electrons initially making it out of the plasma through the magnetic mirror will be those with the negligible magnetic moment. These electrons will have a defined spin-orientation, and a beam of polarized electrons is obtained.

This method, of course, works best when $2\mu_B \Delta B \gg kT_{\parallel}$, where ΔB is the field increment in the magnetic mirror(If $\Delta B = 10$ Tesla, easily realized, then $2\mu_B \Delta B$ then is about 10^{-3} eV ≈ 10 K) plasma temperatures well below that would be required for this technique to work well. The temperature of the traps, and consequently of the plasma, may be lowered below 2 K by pumping on the L He reservoir of the trap. The polarized electrons will, of course, be drawn from the radial center of the plasma, where the plasma is most negative, and the number of polarized electrons that can be extracted at a time is limited by the space charge potential of the plasma, which, after a certain point, will tend to eject electrons regardless of their spin-orientation. Since the plasma potential changes by $\approx kT$ in a radial distance of the Debye length, one may usefully extract electrons with a defined polarization only from radii $r < \lambda_D$. A 10 cm long plasma with density 10^7 cm^{-3}, temperature below 10 K, will yield between $10^4 - 10^5$ polarized electrons each time the dump gate potential is lowered. Electrons removed from the plasma's radial center will be replenished by fluid instabilities which will fill in the center of the plasma on a fast time scale $(100 - 1000\mu s)$, and collisions will rethermalize the electron energy distribution on a slower time scale. Since the electrons will exit the plasma in 100 μs or less, it is possible to produce short pulses of highly polarized electrons. The electrons left behind will be initially depleted of electrons in the ground state and will reach a higher equilibrium temperature as they equilibrate; the electron plasmas are subject to 'evaporative' heating. By leaking out only the electrons in the lowest energy level, and trapping them in a separate section at a much lower magnetic field it may be possible to produce separate electron plasmas with much lower temperatures.

While such a source may not be able to compete with the GaAs-based sources of partially polarized electrons used as accelerator sources and in surface science studies, and described in Appendix A, it may be useful in specific cases where a highly polarized target is needed. The principle of the Penning trap has also been sucessfully used to trap positrons [43], and the method we have described makes possible a similar source of polarized positrons, through the modification of such traps. This is significant because there exist no photocathode for producing polarized positrons, and a source based on such traps may be able to compete with sources based on radioactive emitters [44].

This method of producing polarized electrons becomes more effective if there is an efficient way to 'drain' electrons into the ground state. As described earlier, plasma electrons in a cold trap cool by emitting cyclotron photons. The electrons in high-quantum number classical orbits decay to the lowest Landau levels through electric dipole transitions, which occur on a fast time scale. If the trap is cold enough, essentially all electrons, regardless of their initial spin direction, will end up in the lowest Landau level. The ground state of electrons in a magnetic field is in the lowest Landau level ($n_L = 0$), with spin-moment pointed along the magnetic field, as shown in Figure 6.6. Electrons that start with their moments aligned with the field end up in the ground state, but electrons with spins in the opposite direction get stuck in the lowest Landau level with spin pointed down. The spin-flip required to reach the ground state is a magnetic dipole transition, and occurs on a very slow time scale. If, however, the plasma is excited by a radio-frequency signal at the 'anomaly' frequency of $\omega_a = (g - 2)/2$- $_c$, these electrons can be 'drained' out by exciting them to the $n_L = 1$, with spin-up, from which they can decay quickly to the ground state through the emission of a cyclotron photon. This method has been suggested in [45]. However, it is important to keep the plasma cold to make this possible, and it is very likely that the RF excitation will cause heating of the plasma. Further theoretical investigation is needed to determine if this heating will be large enough that the plasma cannot be maintained at a low temperature (< 10 K).

6.5 Spin-flips in astrophysics

It has been suggested that the electrons, protons (and some positrons) on the surfaces of neutron stars may constitute strongly-magnetized non-neutral plasmas. The extreme gravitational field (these stars have a radius $\simeq 10$ km) and rotational velocities can produce a large charge separation in the star's magnetosphere [46]. The temperatures may be very high, $T \sim 10^6 K$, but the magnetic fields in the vicinity of these compact objects are even more extreme and in the range of $10^8 - 10^9$ Tesla, and essentially all the electrons will be in the lowest Landau level. The parameter ϵ could be less than 10^{-3}; these plasmas would be 'very' strongly-magnetized. When ϵ gets down to this level, typical electron-electron collisions only cause an exponentially small breaking of the adiabatic invariant associated with the spin-precession, and the spin-equilibration rate declines exponentially.

Although this regime is difficult to achieve in the laboratory, it may be found in these pulsar magnetospheres. The energy of the photon emitted as an electron flips to align its moment with a 10^8 Tesla field is 1-10 keV, and there is speculation that some of the sharp X-ray emission lines observed in spectra from neutron stars may be due to such spin-flip phenomena [47]. Although the spin-flip rate is greatly reduced as ϵ is likely very small, the densities involved ($10^{10} - 10^{12} cm^{-3}$) may be large enough to produce observable emission from such spin-flips.

Electrons which spin-flip to align their intrinsic moments parallel with the field may no longer be trapped by the magnetic field lines of the star; this may have consequences for the star's plasma magnetosphere.

Appendix A

The Spin Experiment

A.1 Introduction

In Chapter 6 we described the significance of electron-spin dependent effects in plasmas that have been cooled in strong magnetic fields to near liquid He temperature. In this 'strongly-magnetized' regime the energy to flip the electron-spin magnetic moment in the external magnetic field becomes comparable to the energy in the quantized cyclotron orbits, or Landau levels.

We have set up the experiment to study such spin-related effects in these plasmas. Although no new physics results were acquired on these plasmas for this thesis, I have detailed in this appendix the various considerations that have gone into the setup of this spin experiment. Besides the Cryogenic trap, any such experiment must necessarily have two other main components - a calibrated source of polarized electrons, and a means of detecting and measuring the polarization in a given collection of electrons. The GaAs-based photocathode and the Mott polarimeter are devices that have been proven to meet these needs. We have constructed these devices for this experiment from modified designs provided by other groups. Along with the Cryogenic Trap they make up the main parts of the Spin Experiment.

In this chapter I have detailed the numerous experimental considerations that arose in the planning and design of this experiment. I have also described the principles behind the design and operation of the Mott polarimeter. Similarly, the photocathode is described in detail for completeness. Further, I have described how the experiment is put together around these components.

A.2 Vacuum Requirements

In any experiment involving spin-polarized electron plasmas it is important to ensure that the electron spins are not flipped by collisions with neutral gas molecules, that are present in any trap to lesser or greater extent. Such collisions would interfere with observation of the interesting spin-dependent effects, such as the equilibration of the spin temperature through electron-electron collisions in an non-uniform B field. Of course, this is achieved by maintaining a very good vacuum in the trap region. It is clear from the Figure 6.5, that the spin-exchange depolarization rate through electron-neutral collisions will compete with collisional depolarization in a non-uniform field when neutral gas densities are $10^5 cm^{-3}$ or more. This density corresponds to a pressure in the 10^{-14} torr range,if the gas temperature were assumed to be near the temperature of liquid helium, $4K$ but in the 10^{-12} torr range, for the gas temperature of $300K$, assumed near a measuring ion gauge. . However, the vacuum requirement need not be that stringent since not all gas molecules can cause the undesirable depolarization of electron spins. The residual gas in a typical ultra-high vacuum is mostly composed of molecules such as H_2 and N_2, which only have paired electrons in their electronic configurations. Each occupied orbital in these molecules has two electrons, one in each spin direction, as per the Pauli exclusion principle. A molecule with all its electron spins paired off cannot cause spin-depolarization. This is due to the fact that any plasma electron, with defined spin-direction, can only replace an molecular electron which has the same spin-direction. It cannot replace an electron with the opposite spin-direction because to do so would put two electrons in the same spatial wavefunction, but with parallel spins, which is prohibited by Pauli's rule. The electron exchange would be possible if one of the electrons were excited to another spatial state, yet the typical plasma electron will not have the energy required to cause this excitation. As a result, the main residual gas components in a ultra-high vacuum, such as H_2, N_2 and He will not affect the polarization of the plasma.

Paramagnetic molecules such as O_2, however, have unpaired electrons, in different spatial valence orbitals. One of these electrons can easily be replaced by a plasma electron with the opposite spin, affecting the net spin of the electron ensemble over time. In any spin experiment, therefore, it is important to keep the partial pressure of paramagnetic molecules and atoms below 10^{-12} torr. The fraction of such paramagnetic molecules in the residual gas can be less than 0.1 of the total present and we may be able to tolerate total gas pressures of 10^{-11} torr or more. This is usually achieved even in room-temperature UHV systems, where the main residual gas is H_2 (Molecular hydrogen having both electron spins parallel exists only in a negligible fraction at room temperature thermal equilibrium. Similarily, the amount of atomic hydrogen in the residual gas is also negligibly small). When the trap is maintained at liquid He temperature, all gases except He are condensed on the walls [48], and even the Helium is removed by the activated charcoal in the trap which is cooled to liquid He temperature. Thus, keeping the trap cooled by liquid Helium is enough to ensure that the neutrals concentration is low enough not to be a concern in this experiment.

There is also another important reason to keep a very low level of certain molecules in the trap. Gases such as O_2 and CO are oxidizing agents which can degrade the quantum efficiency of the GaAs photocathode, described in Section A.5, over time. When the photocathode chamber is open to the rest of the trap especially, it is important that a good vacuum is maintained therein. It is often suggested that the ion gauge in the system be turned off during photocathode operation, since the tungsten filaments in some gauges can be a source of oxidizing CO. This is not known to be a problem with the iridium filaments that we use commonly [49].

A.3 Measuring the Polarization

A spin-polarized plasma (or electron-beam) has an greater number of electron-spins pointing in a given direction (such as along an external magnetic field) than the number pointing opposite to it. Any experiment that involves such a plasma must have a means of measuring the difference between ‘spin-up’ and ‘spin-down’ populations reliably. The standard technique to measure the ‘polarization’ is to employ ‘Mott scattering’. This measures the left-right asymmetry in the scattering of a beam of transversely polarized electrons off the nuclei of high-Z materials, such as gold. The effect, which comes about through the coupling of the electron spin and angular momentum, becomes significant only at semi-relativistic energies, and is observed through a Mott polarimeter. It requires that the spins of the electrons be perpendicular to the momentum; the electron spins must be rotated to transform a longitudinally polarized beam into a transversely polarized one, and this is achieved by the ‘Spin Rotator’. In the Spin Rotator, a magnetic field is imposed perpendicular to the beam which causes the spins to precess by 90^o, while an electric field compensates for the magnetic force which, taken alone, would tend to deflect the beam. The Mott Polarimeter and Spin Rotator constructed for our experiment are described in the following sections.

A.3.1 The Mott Polarimeter

Mott scattering is used to measure the polarization, the difference between the number pointing up versus the number pointing down, in a beam of electrons. This technique and the apparatus used for it are described in detail in two review articles [3, 50]. Yet I will provide a brief overview here, for completeness.

Mott polarimeters take advantage of the left-right asymmetry in the scattering cross-section when transversely polarized electrons are backscattered at large angles by the nuclei of atoms in a target foil. We are looking at the cross-section for backscattering at angles near 120^o, so we consider scattering of the electron at small impact parameter from a nucleus in the target. The origin of this asymmetry may be understood through the means of a classical picture. As shown in Figure A.1, the electrons incident upon a gold-foil can scatter to the right or left of a gold nucleus.

The motion of the electron in the electric field E of the nucleus results in a magnetic field B in the electron rest frame given by $\mathbf{B} = -\mathbf{v}/c \times \mathbf{E}$, where $\mathbf{v}$ is the electron velocity. If $\mathbf{r}$ is the nucleus-electron radius vector, and Ze the nuclear charge, $\mathbf{E} = (Ze/r^3)\mathbf{r}$ and $\mathbf{B}$ becomes $\mathbf{B} = (Ze/cr^3)\mathbf{r}\times\mathbf{v} = (Ze/mcr^3)\mathbf{L}$. Here $\mathbf{L}$ is the orbital angular momentum of the electron, which would carry opposite sign depending on

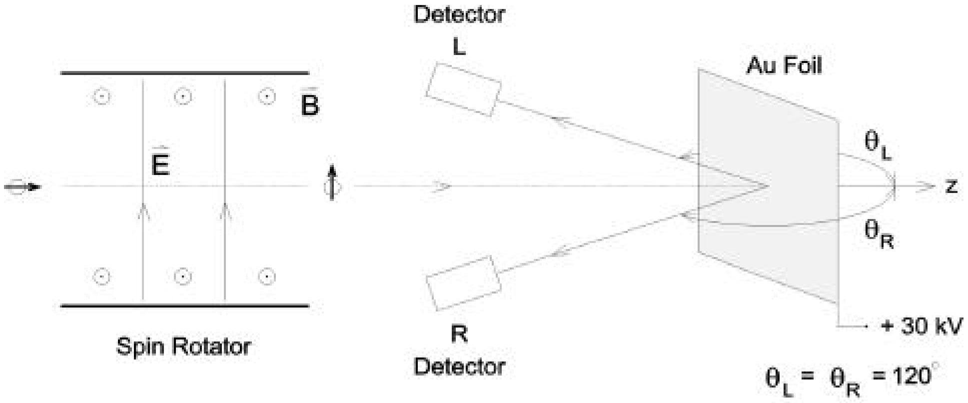

Figure A.1: Schematic of Mott scattering

whether the electron scatters to the left or right of the nucleus. The interaction of the electron-spin magnetic moment $\mu_\mathbf{s}$ with this magnetic field introduces an additional term in the scattering potential $V_{so} = -\mu_\mathbf{s} \cdot \mathbf{B}$. The electron magnetic moment is related to the electron spin S by $\mu_s = -(ge/2mc)S$, where g is the spin-factor ($g = 2.002.. \approx 2$). V_{so} is therefore given by $(Ze^2/2m^2c^2r^3)\mathbf{L} \cdot \mathbf{S}$, where an additional factor of $\frac{1}{2}$ is included to account for Thomas precession.

This spin-orbit term in the scattering potential introduces a spin-dependence in the scattering cross-section $\sigma(\theta)$ which may be written [51]

$$\sigma(\theta) = I(\theta)(1 + S(\theta)\mathbf{P} \cdot \hat{\mathbf{n}}) \tag{A.1}$$

where $S(\theta)$ is the asymmetry function, $I(\theta)$ is the total (including both spins) scattered intensity, and $\mathbf{P}$ is the polarization of the incident electrons. The unit vector $\hat{n}$ is normal to the scattering plane, that is, it points in the direction $\mathbf{k} \times \mathbf{k}'$ where $\mathbf{k}$ and $\mathbf{k}'$ are the wave vectors of the incident and scattered electrons respectively. Thus, the direction of $\hat{n}$, which is parallel to $\mathbf{L}$, depends on whether the scattering proceeds to the right or to the left, and the sign of the second term in Eq. A.1 is affected accordingly.

The component P of the incident electron spin polarization normal to the scattering plane is simply,

$$P = \frac{N_\uparrow - N_\downarrow}{N_\uparrow + N_\downarrow} \tag{A.2}$$

where $N_\uparrow$ and $N_\downarrow$ are the number of incident electrons with spin up and spin down with respect to an axis chosen to be normal to the scattering plane. Scattering produces counts N_L and N_R in the left and right detectors as shown and the scattering asymmetry is

$$A(\theta) = \frac{N_L - N_R}{N_L + N_R} \tag{A.3}$$

Eq. A.1 would suggest that N_L is proportional to $N_\uparrow[1+S(\theta)]+N_\downarrow[1-S(\theta)]$(and vice versa for N_R). Substituting into Eq. A.3 yields,

$$A(\theta) = PS(\theta) \tag{A.4}$$

This expression is the basis of Mott scattering polarimetry. If the asymmetry function $S(\theta)$ is known, measurement of the scattering asymmetry $A(\theta)$ yields the polarization component P normal to the scattering plane being considered. $S(\theta)$, termed the 'Sherman' function, after the person who first undertook the study of relativistic electron scattering in a point Coulomb field. This work, and subsequent experimental measurements, have shown that, for high-Z targets and large scattering angles, $S(\theta)$ can be significant ($\sim$ -0.3 to -0.6) suggesting that under appropriate conditions the left-right asymmetry in the scattering of polarized electrons should be easily detectable. $S(\theta)$ has a broad maximum near 120^o, and the scattered signal is typically measured in a range around this angle.

The effect is most significant at semi-relativistic energies (greater than 20 kVolts), and most polarimeters are operated at this voltage or higher. The scattering asymmetry increases with the square of the atomic number Z, hence gold foils ($Z = 79$) are chosen as the most common scattering target. Generally, the foils need to be thick enough to maximise the scattered-electron signals. Use of thick targets, however, introduces effects due to multiple scattering within the target. This confounds the observation of the scattering asymmetry and results in "effective" Sherman functions,

$S_{eff}(\theta)$, that are below those expected from the theoretical treatment of single nucleus scattering. As a result, it is important to calibrate $S_{eff}(\theta)$ for each polarimeter design, with its particular choice of target and electron detectors. A known source of polarized electrons is used for this purpose, and is described in Section A.5.

An important parameter in comparing polarimeter performance is the efficiency ϵ, defined as [51]

$$\epsilon = \left(\frac{I}{I_0}\right) {S_{eff}}^2 \tag{A.5}$$

where I_0 is the current entering the polarimeter, and I is the total scattered current measured by the left and right detectors. This 'figure of merit', is proportional to the inverse square of the statistical error in an electron counting experiment to measure the polarization of an incident beam. Thus, maximization of ϵ minimizes the error in the measured polarization for a given number of incident electrons.

The 'micro-Mott' design that we have chosen has $\epsilon \sim 2\text{x}10^{-5}$ [3] Although, larger 'conventional' polarimeters have somewhat higher values for ϵ, the small size of this design is a critical advantage for the experiments we would like to undertake.

The Mott polarimeter is designed to cause a focussed electron beam to scatter on a gold foil at high energies ($\approx$ 30 kV), and to measure the left-right asymmetry in the scattered signal near 120^o. The effective value of this constant is usually experimentally determined for each type of Mott polarimeter to calibrate it. Our polarimeter is a slightly modified version of the 'Micro-Mott' design, provided to us by the Spin-Physics group at Rice University [3]. A cutaway schematic of this polarimeter is shown in Fig. A.2 This 'retarded-potential' polarimeters consist of two concentric hemispheres; the inner one holds the gold foil and is at high voltage of $\sim$ 30 kV, while the outer is near ground. The electrons are accelerated by the strong field between the hemispheres, which also strongly focusses the beam at the center of the foil. One or more lens elements situated before the large hemisphere provide initial focussing; the voltages on the elements are chosen to optimise the beam focus, as determined by a charged-particle optics program SIMION provided by DOE, and are usually between 1 and 3 kV. The focussed electron beam is scattered by the nuclei in the target and the backscattered signal is measured by channeltron detectors (from Galileo Electro-Optics)symmetrically placed in the outer hemisphere, at an angle near 120^o.

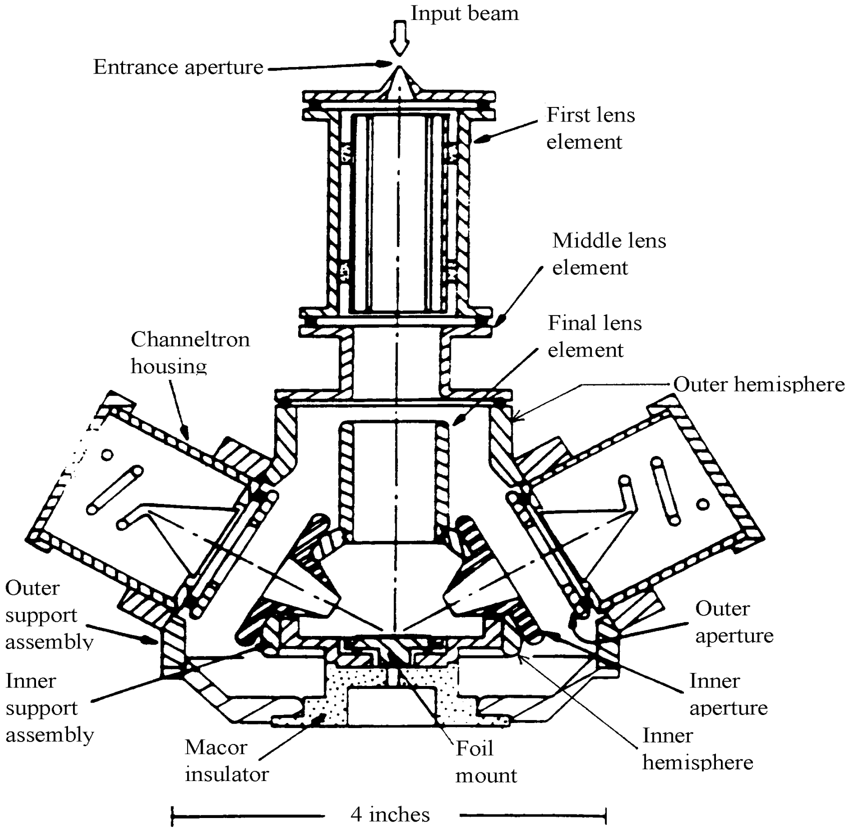

Figure A.2: Cutaway of a Micro-Mott polarimeter, from [3]

Most of the polarimeter components are machined from 316 non-magnetic stainless steel. The inner hemisphere is held by a Macor (machineable ceramic) insulator, which isolates it from the outer hemisphere. The lens elements are insulated through the means of sapphire beads, which also provide precise alignment of these parts in the polarimeter. The 0.005" thick gold foil we used was held in place by a SS ring which was press fit into the center of the inner hemisphere. The entrance apertures to the channeltrons are held at the potential of the outer hemisphere, i.e., a few hundred volts above ground. This essentially eliminates the secondary electron emission from the gold foil from entering the channeltrons, while still providing enough energy to the scattered electrons that they excite the channeltron detector. We use the Galileo model 4716 channeltron which has a gain of about 10^6 near an operating bias of 2000 V. We require the detector to be always operated in the linear regime, when a pulse of electrons is incident on it, and a larger bias may drive this electron multiplier into saturation. A channeltron is essentially a hollow glass tube with a semiconductor resistive layer on the inside. An incident electron at the entrance excites secondary electrons which drift toward the positive bias end of the tube, exciting more secondaries along the way. The tube is curved to provide a higher gain, as almost all secondaries are trapped within the tube and do not exit through the opening in front. So as not to damage the delicate glass we held these channeltrons firmly in place by caps made of Teflon.

Although we operate both left and right channeltrons at the same voltages, it is very likely they do not provide exactly the same gain, at any given time. We also noticed that the gain of these detectors varies slowly with time. It is important therefore to eliminate such systematic effects from the measurement of an actual scattering asymmetry. Further, it is always likely that there are other instrumental asymmetries which affect the measurement of the actual electron signals in the right and left detectors. If the incident electron beam is slight misaligned with respect to the polarimeter axis, or if the beam gets focussed slightly away from the center of the gold foil, both would result in an apparent scattering asymmetry, which would interfere with any effect related to the polarization of the incoming beam. It is important to eliminate these systematic errors from any polarization measurement. This is done by using a calibrated source of polarized electrons, whose polarization can be reversed easily, without affecting any other beam conditions. The part of the asymmetry between the left and right signals that remains unchanged when the polarization is reversed is the part that is due to the instrumental errors, since the scattering asymmetry due to polarization reversal will change sign while retaining the same magnitude. We have built such a standard source, to be described in Section A.5.

A.3.2 The Spin Rotator

The electrons from a photocathode source or electron trap are usually extracted as longitudinally polarized beams; the spins are defined in the direction of the electron beam momentum. The spins must be rotated by 90^o to make them transversely polarized. Like a top in a (transverse) gravitational field, an electron spin magnetic moment precesses about the direction of a transverse magnetic field, so this rotation is effected by applying a perpendicular magnetic field to the beam. If the (angular) precession frequency is - $_p$ and time the electron is in the field is Δt, the electron precesses through angle - $_p\Delta t$. The precession frequency is very nearly the cyclotron frequency (since $g \approx 2$) and $\Delta t = v/l$, where v is the electron velocity and l is the extent of the applied field B. The angle of precession is then $(eB/mc)(v/l)$; the electron energy and the applied field should be set such that this equals 90^o.

Since the Lorentz force from the transverse field will tend to bend the beam, it must be compensated for by a crossed electric field. Hence the design of the Spin Rotator is similar to that of an $E \times B$ filter, used for mass or velocity selection of charged particles. In our device a magnet, supplied with a current of few amps, maintains a nearly uniform field of about 20 gauss (for electron energies of 500V-1kV) over about 3". The yoke (constructed from magnet iron recovered from the Berkeley Bevatron) provides a good magnetic circuit. A pair of copper plates placed perpendicular provide the compensating electric field; voltages of 200-300 V are applied between the plates about 1.5" apart. Copper strips, placed on the edge between these plates, and connected to a string of high vacuum compatible resistors, make sure the voltage drop is linear between the plates, and ensure that the electric field is uniform. (A similar scheme using high-vacuum resistors is now used in the plasma imaging system in another trap at Berkeley to ensure that the voltage drop is linear and that there non-axial electric fields in the acceleration region are negligible). Another such set of plates, placed along the other axis, provides steering in that direction. These steering plates were placed inside a SS square tube which was attached to the vacuum chamber housing the Mott polarimeter.

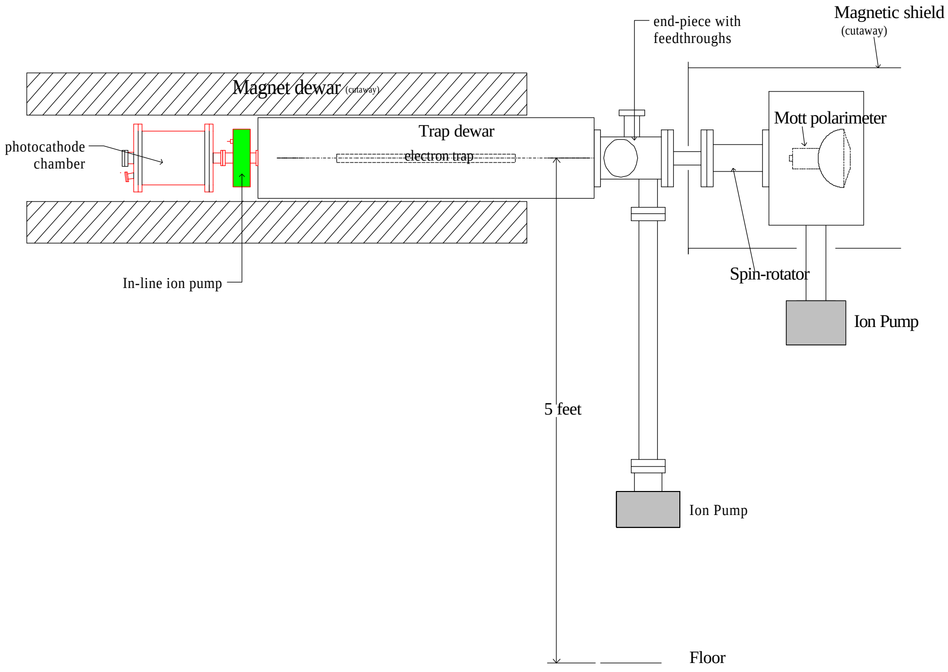

Figure A.3: Scheme for the Spin Experiment

A.4 Extraction of Trap Electrons

As seen in Fig. A.3, electrons leaving the trap to enter the polarimeter will tend to follow the divergent magnetic field lines at the edge of the solenoid. As we move away from the trap then, the electrons would be collected over a wider and wider area, with less and less being captured by the narrow optics of the Polarimeter. The efficiency of measuring the polarization P of a number of electrons N is determined by P^2N, and it is important to capture enough trap electrons into the polarimeter to measure this efficiently. For this reason, (and also to keep the vacuum chamber as compact as possible) it is very necessary to situate the Spin Rotator and Mott Polarimeter as close as possible to the Electron Trap.

A.4.1 The Magnetic Shield

We want the Spin Rotator and Mott Polarimeter to be as close as possible to the Electron Trap. This means that they would need to be placed in a region where the axial component of the magnetic field, due to the the trap solenoid, would normally be a few kilogauss. A smaller radial component of the field would naturally also be present. The Spin Rotator works by imposing a field of ~ 20 gauss perpendicular to the beam direction. Since electron spins precess about the local direction of the magnetic field, the axial component of the magnetic field (i.e. along the beam direction) must be much less than this for the Rotator to work effectively. Therefore, a means must be found to shield the Rotator and Polarimeter from the very strong field of the solenoid, i.e. reduce it to a few gauss or below. This is achieved through the Magnetic Shield, which keeps the polarization detection apparatus in a nearly field-free region, yet physically proximate to the electron trap.

Typically, magnetic shielding is provided by materials with very high magnetic permeability. Magnetic field lines tend to prefer 'flowing' through high-permeability materials in much the same way that a region of high electrical conductivity draws away electric current from a nearby region of much lower conductivity. Nickel alloys such as mu-metal have very high permeability, and multiple layers of these can be to attenuate ambient fields to very low levels. Such materials provide a 'low-impedance' path for magnetic field lines and draw them away from the region that needs to be field-free. However, these materials are also expensive, and only thin sheets (less than a mm thick) are easily affordable. As they sweep up the field lines, the field density in their bulk becomes very high and they can be saturated easily even with relatively small values for ambient magnetic fields, a few tens of gauss. Therefore, an effective approach is to use thick layers of cheaper magnetic materials such as steel to reduce the ambient field from the kilogauss range to well below 100 gauss, and then use a layer (or two) of mu-metal to reduce it further to tolerable levels. We used cylindrical shells of cold-rolled steel, closed at the end facing the magnet, to enclose the Spin-Rotator and the Mott Polarimeter. It was important that the flanges that closed off the shield at the magnet end were welded to the rest of the shield. This ensured that a continuous high-permeability path was available for the magnetic field lines which were diverted from the polarization detector; even a very thin air gap between the flanges and the body of the shield would have rendered it ineffective. The steel shield is made of two coaxial layers, 3/8" and 1/4" thick, each split into two halves for ease of assembly. Each layer was also annealed to make it magnetically soft. A 1" hole was provided in the front flange, to admit the electrons from the trap. The magnetic permeability of steel is not constant, i.e. $\mu = \mu(H)$, and it is important to try to design the shield so that the flux density in the bulk material is close to the region where the permeability is the greatest, and the shielding efficacy of the material is at its maximum. Fig. A.4 shows the magnetization curve of a typical cold-rolled steel alloy. The $\mu(H)$ is, of course, a maximum in the sloping region of the graphs, corresponding to a flux density in the bulk material of 2-12 kilogauss and we designed the shield thickness to make sure that the shield was operated in that range. In this regime, the shielding ratios in the center of the shield were ~ 50, close to the theoretical expectation, and reduced ambient fields from a few kilogauss to below 100 gauss. This was further reduced by two coaxial cylinders of mu-metal, each 0.010" thick. The 1" hole at the front of the shield allowed a small amount of flux to leak in, but this was attenuated toward the interior of the shield. The mu-metal is always necessary because steel does not have the very high permeability, and may have some remanent magnetization. We managed to reduce the ambient field at the position of the Spin Rotator to below 5 gauss. We may have to use another layer of mu-metal sheet to reduce to this further. More effective shielding is achieved by using multiple sheets of thin material than a single thick layer, as pointed out in [52] and references therein.

The shield is composed of nearly 70 lbs of magnetic steel. When it is placed near the superconducting solenoid magnet, there will be a strong attractive force between them. We have measured the strength of this force, and it was about 85 lbs when the central field of the solenoid was 3 Tesla. This force is much less than the maximum strain that can be sustained by the supports of the superconducting coil. However, it is quite likely that the coils were being slightly shifted along its axis, as the shield was brought into its proximity, affecting the charged-particle optics through the trap and detector. However, once the optics was tuned for efficient transmission of electrons through the experiment it remained stable.

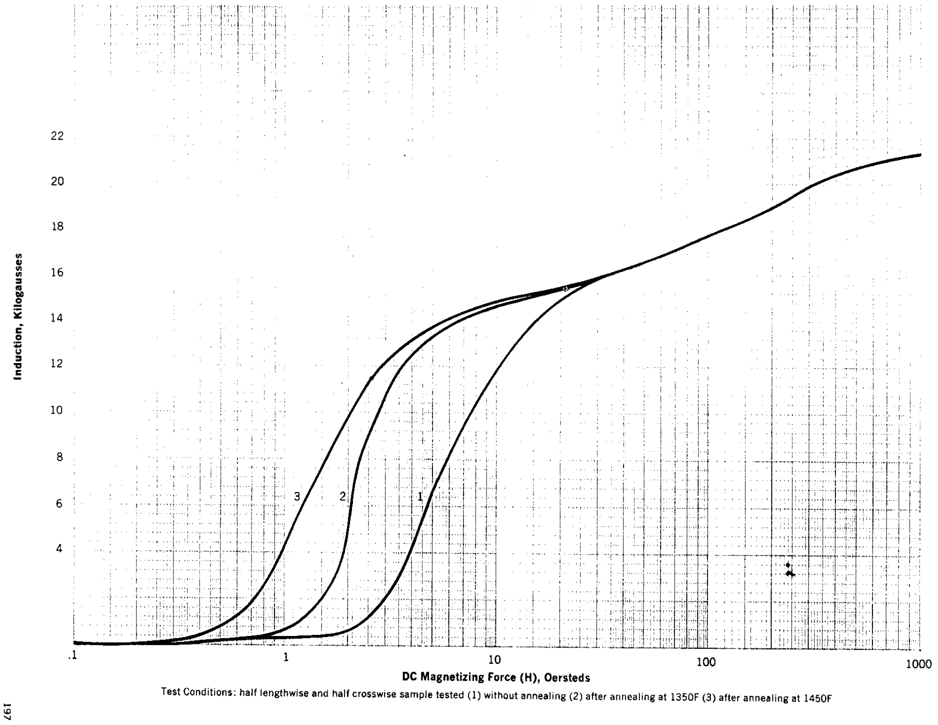

Figure A.4: The magnetization curve - B versus H, in Cold Rolled Commercial Quality Steel - 24 Gage [4]

A.4.2 Transmission of Electrons through the Shield

As the magnetic field lines are swept away from the axis of the spin-detection apparatus, it is , of course, important that the electrons which would tend to follow the field lines not be lost to the walls. We have been able to alleviate this problem by placing a narrow tube, biased at a high voltage, in the part of the vacuum chamber that passes through the entrance aperture of the magnetic shield. As the electrons from the trap are accelerated to a high axial velocity, we expected that they will be able to traverse the region of rapidly changing magnetic field strength in a time comparable to the cyclotron orbit period in that region. As this happens we expected that the electrons may be coaxed off the magnetic field lines and enter the spin-detection region with only a small radial component of the velocity.

We have used this method effectively to capture up to 20% of the electrons that exit the trap. In principle, the transmission is most efficient when this tube is biased at a high-voltage of 10-20 kV. However, we found capture efficiencies of a few percent even at voltages as low as ~ 1 kV.

A.5 The GaAs Polarized Electron Gun

An electron source of known polarization is needed to calibrate the instrumental asymmetries of the Mott Polarimeter. As described in Chapter 6 using an polarized electron source we may also create a plasma of known initial polarization and observe the depolarization rate in this plasma. The most sucessful technology to produce large currents of polarized electrons are photocathodes made from Gallium Arsenide crystals. This technology has been developed over the past 20 years and has been used for two main purposes. Beams of polarized electrons are used to probe the properties of surfaces through polarized low energy electron diffraction (PLEED) [53]. GaAs cathodes are also used to produce polarized beams for electron accelerators, such as the Stanford Linear Accelerator, where spin-dependent high-energy scattering physics is studied. The design we use for this our own experiment is a modified version of the SLAC design, provided to us by Greg Mulhollan of SLAC [54]. In the following sections, I will describe the construction and operation of our polarized electron source.

A.5.1 GaAs as a photocathode

The source mainly consists of a GaAs-based photocathode: when excited by circularly polarized light, the electron emission from the photocathode is partially polarized, along the axis of the incident light beam. Gallium Arsenide is used to make reliable polarized electron sources for two prominent reasons:

1. The band structure of this direct band gap III-V semiconductor permits a given electron spin state to be preferentially pumped from the valence band into the conduction band, when excited by photons of a given polarization.

2. Its surface can be treated to lower its work function, to permit efficient emission of photoelectrons. The band structure of GaAs at the energy maximum of the

valence band and energy minimum of the conduction band is shown in the left-side of Fig. A.5. The band energy versus momentum is shown in this figure. The band gap of the material is E_g=1.52eV; photon energies in the near infra-red or greater produce photoemission. The electron wavefunctions at the minimum of the conduction band have S symmetry, while the wavefunctions at the maximum of the valence band have P symmetry. Spin-orbit splitting causes the $P_{3/2}$ to be above the $P_{1/2}$ state by Δ=0.34 eV. The selection rules for the absorption of right- and left- circularly polarized photons are $\Delta m_j = +1$ and $\Delta m_j = -1$, respectively, indicated by the solid and dashed arrows in the drawing on the right-side of Fig. A.5. Photon absorption proceeds through an electric dipole transition, and the orbital angular momentum changes by one unit, leaving the electron spin unchanged.

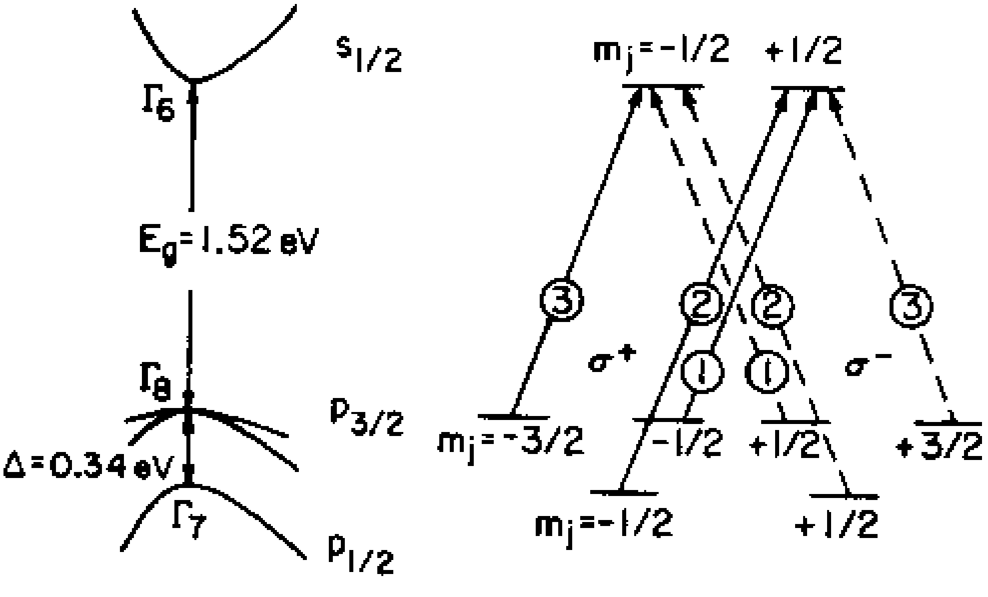

Figure A.5: Band structure of GaAs, from [5]

When a photon, say right-circularly polarized, is incident upon a GaAs crystal, the photon momentum direction defines the axis of the system. All projections of vectors refer to this axis. For photon energies E_γ such that $E_g \leq E_\gamma \leq E_g + \Delta$ transitions can only occur from the $P_{3/2}$ states to the $S_{1/2}$ states. Two transitions are possible: the P state with $m_j = -3/2$ can make a transition to the S state with

$m_= -1/2$, and the P state with $m_j = -1/2$ can make a transition to the S state with $m_j = +1/2$. In the first case, the emitted photoelectron has spin anti-parallel to the incident photon (and parallel to its momentum direction); in the second case, the electron spin is parallel to the incident photon momentum (and anti-parallel to its own momentum). The P state with $m_j = -3/2$ is a pure spin state while the state with $m_j = -1/2$ is not; the Clebsch-Gordon coefficients make the first transition three times more likely than the second. The circled numbers in Fig. A.5 indicate the relative transition rates. Right circularly polarized light incident on a GaAs crystal, will then ideally produce right-handed electrons with polarization

$$\mathbf{P} = \frac{N_\uparrow - N_\downarrow}{N_\uparrow + N_\downarrow} = \frac{3-1}{3+1} = 50\% \tag{A.6}$$

Absorption of polarized photons excites polarized electrons into the conduction band, and to make an effective photocathode source, these electrons must make it out of the crystal with sufficient energy. In normal GaAs, electrons at the bottom of the conduction band need 4 eV to reach the free electron state. Even with a large applied electric field, GaAs is a poor photoemitter. However, addition of cesium to the surface reduces this energy gap; and the further addition of Oxygen produces the negative electron affinity (NEA) required for efficient photoemission. This is shown schematically in Fig. A.6. The effective electron affinity, defined as the energy difference between the vacuum level and the conduction band minimum *in the bulk* becomes negative with the creation of a layer of Cs_2O on top of the bulk GaAs. (The vacuum level remains above the conduction band minimum at the surface). NEA surfaces are very efficient photoemitters because the depth from which electrons can be emitted is not limited by the hot electron mean free path ($\sim$ 10 Å) but rather by the diffusion length ($\sim 1\mu$m) for electron thermalized to the conduction band minimum. Quantum efficiencies (the probability that an electron is emitted when a photon is incident upon the photocathode surface) can be as high as 10% when the GaAs surface has been treated with Cs_2O. At the near infrared photon energies (800-950 nm) appropriate for polarized electron production, quantum efficiencies in the range 0.1%-0.5% are typical. The quantum effiency typically increases with incident photon energy, but usually the polarization of emitted electrons is much less than

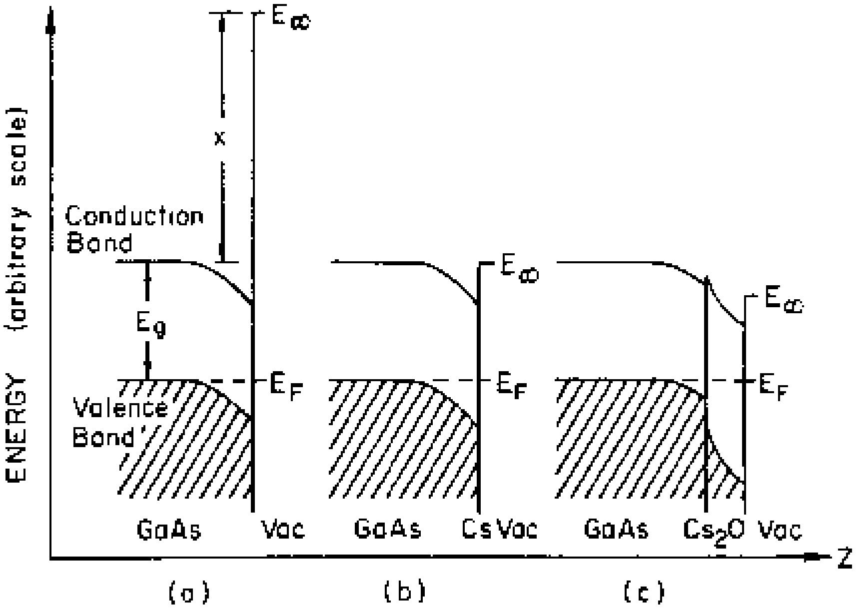

Figure A.6: Energy levels in GaAs, from [5]

the theoretical 50% when the crystal is excited by visible (or higher energy) photons. [54].

In practice, even with photons tuned to the band-gap, polarizations below the theoretical best of 50% are observed. This is because the polarized photoelectrons undergo depolarizing spin-flip scattering processes in the crystal before they leave the bulk material. Typically, polarization in the range 40%-45% are common, with the theoretical 50% degraded somewhat. The crystal has been known to produce polarizations of 43+/-2% [53], when processed as per instructions from the SLAC group, and we assume this number for our calibration purposes. The maximum observed quantum efficiency (photoelectrons per incident infrared photon) is 10%, but typically a few percent is easily attainable. More recently, [54], photocathodes based on 'strained' crystals of GaAs have been developed with polarizations in the range 60-80%. Yet, greater care has to be taken in the treatment of these crystals, and their quantum yield is much smaller, so we have decided to use the simpler 'unstrained' versions.

As depicted in Figure A.3 the cathode crystal in the photocathode chamber will be in a strong magnetic field. Since these GaAs cathodes have never been operated in such field before there is an issue if they will remain unaffected by it. We have not tested our cathode in the strong field region, but expect that the magnetic field should have no significant effect [55]. A heuristic argument for this is that the spin-interaction energy $2\mu_B B \approx 4 \times 10^{-4}$ eV is much less than the 1.6 eV band gap of GaAs.

A.5.2 The Construction of the Cathode

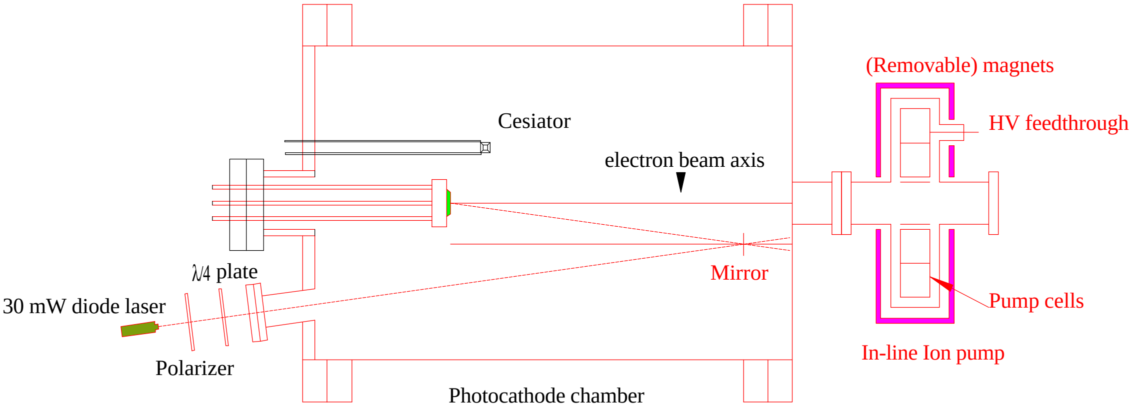

Figure A.7: The photocathode chamber and the in-line ion pump

Cleaning, activating and maintaining the photocathode requires ultra-high vacuum, which stays in the high-10^{-11} to low-10^{-10} torr range. We have achieved this by placing the cathode tower, which holds the GaAs crystal, in a stainless steel chamber 8" in diameter. It is was pumped by a 30 l/s ion pump, and had St707 Gettering strips for additional pumping of CO and other oxidizing gases. The gettering material provides pumping when the pumping efficiency of the ion pump is reduced in the UHV range. The scheme for this is shown in Fig. A.7.

We used the standard 30 l/s ion pump for testing purposes. When we want to operate our photocathode in the magnet as shown in Figure A.3, this ion pump will not fit into the magnet bore along with the photocathode chamber. Although not yet constructed we have designed an in-line ion pump to provide adequate pumping between the Cryogenic trap and the photocathode chamber. This design, based on a similar apparatus developed for beam experiments at SLAC [56], has pump cells arranged in a circular ion pump chamber that is enclosed by removable magnets which provide the ~ 1 kGauss field needed for efficient ion pump operation. When the experiment is moved into the axial magnetic field of the solenoid, the magnets are removed, and the ion pump operates efficiently by means of the external solenoid field (This field is typically much greater than 1 kGauss, yet this does not seem to affect the pumping speed of a similar pump demonstrated in our lab).

Figure A.8 shows the 'cathode heater tower' which holds the assembly that is used to heat-clean and activate the crystal. The GaAs crystal is clamped down on to the Ta holder bottom (3), with the Mo ring (4). Three Moly screws (7) are tightened against Moly nuts on the other side of the Heater block (1). A Type K thermocouple (Chromel-Alumel) is attached to the base of (1) with the help of one of these screws. This thermocouple allows us to monitor the temperature of the heater block during the heat cleaning procedure. The tungsten filament (10) provides the heating. The filament is supplied by (a pair) of Mo conductor rods (6). The filament passes through alumina tubes in the heater block which insulate it, and is attached to the filament conductor rods by screw pads. The heater block is held in place by the hollow cathode biasing tube (Mo), to which it is tack welded. The entire assembly is held in place on the flange with a SS ring (with alumina spacers provide the insulation). It is placed on the Tantalum base of the cathode heater tower shown in Fig. A.8. The Molybdenum ring on top holds down the crystal onto this Tantalum base. We use only refractory metals in the construction of the cathode tower because they have little oxide contamination and can withstand the high-temperatures of the heat cleaning. The cathode should only be in contact or close to refractory materials , especially if those parts are going to get hot. GaAs is very reactive at high temperatures and should not be in contact with any stainless steel or copper. The heating is done by a tungsten filament located underneath the Ta base. The Ta base provides good thermal contact to maintain a uniform temperature over the area of the crystal.

A leak-valve is used to introduce oxygen into the chamber. The leak-valve is at-

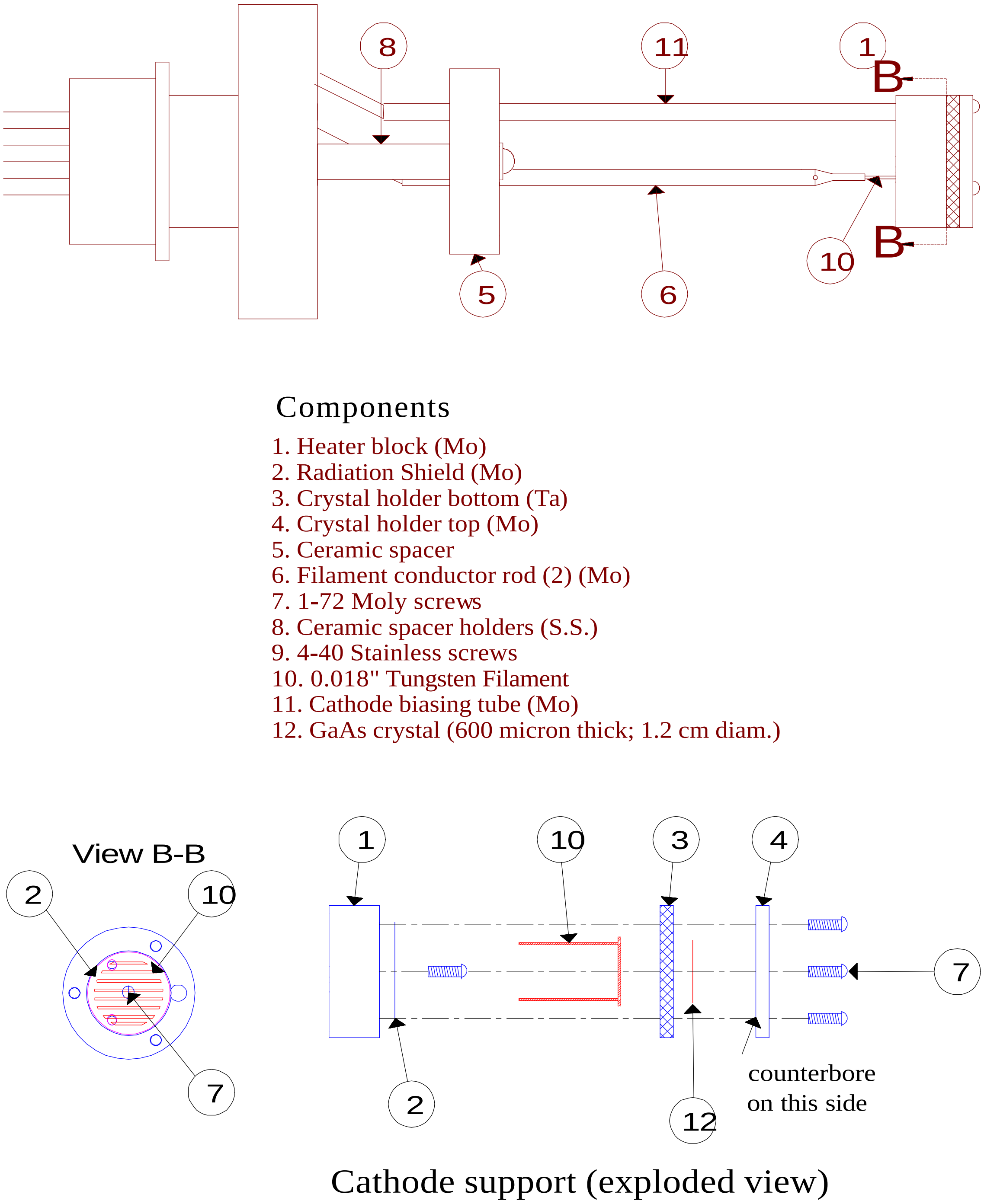

Components

1. Heater block (Mo)
2. Radiation Shield (Mo)
3. Crystal holder bottom (Ta)
4. Crystal holder top (Mo)
5. Ceramic spacer
6. Filament conductor rod (2) (Mo)
7. 1-72 Moly screws
8. Ceramic spacer holders (S.S.)
9. 4-40 Stainless screws
10. 0.018" Tungsten Filament
11. Cathode biasing tube (Mo)
12. GaAs crystal (600 micron thick; 1.2 cm diam.)

Figure A.8: The cathode heater tower assembly tached to the chamber, and the other end is attached through a needle valve to the oxygen bottle. The needle valve remains closed, with the leak valve all the way open during the bakeout. We use stainless steel tubing everywhere. It is highly recommended that all tubes and other apparatus are flushed with the flow of dry oxygen before the valves are closed off. Use of plastic hose here may bring in undesirable hydrocarbons which may accumulate in the chamber over time. While UHP - ultra-high purity oxygen (99.994%) is recommended, we had good results with commercial products which are better than 99% pure.

The cesiator we used was a standard 0.5" SAES Cesium evaporator source, which was attached to vacuum current feedthroughs, and placed about 1" away from the GaAs crystal, with the emitting edge pointed towards it. We were able to achieve adequate cesiation of the cathode by passing currents ~ 4 A through the cesiator. It is recommended to pass nearly this much current through the cesiator during the tail end of the vacuum bakeout to degas it. Since we use a very small heating current, releasing only a small fraction of the Cesium contained in the evaporator at any given time, a single evaporator source may be used in the photocathode chamber essentially forever.

A.5.3 Preparing the GaAs crystal

As described in the previous section, the GaAs crystal must be treated with Cesium and Oxygen to lower its effective work-function and increase its quantum efficiency. This processing increases the photoemission of the GaAs crystal substantially. While the production method for such photocathodes is well-documented in [53], I will describe some of the main steps below, along with special precautions that we took.

The technique of cathode activation requires the preparation of an oxide- and carbon-free surface in an ultra-high vacuum system. The clean surface is then coated with an alkali, Cs being the most effective, while monitoring the photoemission with a light source such as a laser until the photocurrent peaks. A tremendous further improvement in yield is accomplished by adding an oxidizer (both O_2 and NF_3 have been used with similar results) at low pressure. The Cs and O_2 may be applied simultaneously, or alternating the two, until the maximum photocurrent is achieved.

Before activation, the crystal must be cleaned to eliminate any oxides or carbon traces, and to expose a fresh layer of GaAs for activation with Cs and O. The 600 μm crystals are fragile and are typically bonded with paraffin to a thicker glass substrate which protects them during transport and storage. The crystal is separated from the glass by dissolving away the wax in a beaker of boiling trichloroethane. The 0.5” diameter crystal was then etched in a solution of concentrated sulfuric acid and hydrogen peroxide, as per the steps described in [54], to eliminate oxides and carbon contamination. It is then rinsed in high-purity methanol and dried with filtered nitrogen gas.

The etched crystal, now dry, is now ready for the heat-cleaning procedure in the ultra-high vacuum cathode chamber, which is pumped down as soon as possible. While initial rough-pumping is performed by cryo-sorption pumps, the ion pump produces a higher vacuum. We bake the chamber at a minimum of 250^oC for two-three days. During the bakeout the leakvalve is kept open all the way. A high-pressure of oxygen on one side of the valve may cause unacceptable oxidation. During the cooldown after the bakeout, the St707 getter is activated by passing a 35-50 A heating current through it. It is best to activate the getter when the ambient pressures are lower than 10^{-8} torr, to keep from saturating it at higher pressure. During the bakeout, and cool down, we typically keep the heater block (and GaAs crystal) warmer than the rest of the chamber by 40-50^oC. The cesiator may be degassed by passing about 4 A through it for 2 minutes (when the pressure begins to decline) during the tail end of the bakeout, after the getter has been activated. (A repeat of this degassing procedure just before reaching chamber base pressure is sometimes helpful) When the chamber temperature has fallen below about 70^oC, the leak valve may be closed and it is safe to introduce Oxygen gas to the other side. Heat-cleaning of the cathode is done to create a fresh surface of GaAs for activation to make a photocathode. We typically increase the filament current until we read a temperature of about 600^oC through the thermocouple at the bottom of the heater block. The basic idea is to heat the crystal to the range of temperature where the Ga and As evaporate congruently, that is, in equal proportions. Above the maximum congruent evaporation temperature, which is about 660^oC, the As evaporates preferentially as As_2, leaving behind small Ga droplets on the surface. This creates a frosty appearance on the crystal. It is important to go as close as possible to this point, without crossing it. We established the operating point by sacrificing a crystal to ascertain the amount of heating current which got us into the right temperature range, about 620^oC as measured by the thermocouple. When the heater block is at temperature it glows a dull red. However, an IR pyrometer is ineffective in determining the temperature because the emissivity is not very well-known.

It is important to keep the chamber pressure below 10^{-8} torr as much as possible during this time. The heat-cleaning is completed by maintaining the heating current through the filament for a few minutes.

A.5.4 Making the Cathode

When the heat-cleaning concludes, the block is allowed to cool to room temperature. We get the cesium going by passing about 4 A through the cesiator. We monitor the photocurrent. The light source we used to the make the cathode was a simple 5mW He-Ne red laser. (Although the quantum efficiency is essentially the same between the red and infrared lasers, the red laser does not produce polarized electrons since it is not tuned to the band gap). When the photocurrent begins to saturate, open the leak valve and let the oxygen pressure rise to the mid-10^{-9} torr range while leaving the Cesium on. We watch the photocurrent rise sharply and keep it going till it appears to saturate. Once the photocurrent appears to have leveled off, close the valve. The photocurrent will begin to drop and we turn off the Cs when the current has dropped by 10-20%. This ensures a surplus of cesium which is beneficial in the long run because the cathode tends to become deficient in cesium over time. Depending on the residual pressure in the chamber, the photoemission will slowly decline over time. The emission may be recovered by turning on the Cesium briefly to recesiate the cathode. This procedure may be repeated several times, until no improvements are seen. It is easy to get about $10\mu A$ from the 5mW red laser. If the cathode is not up to expectations , it may be best to heat clean over again and make another cathode. It is not unreasonable to expect about $100\mu A$ with a 10mW laser (at 830 nm) shining on it; dirty vaccums and poorly cleaned cathodes may yield less.

We used a 30 mW (at 830 nm) diode laser from Melles Griot to excite our cathode. The light was incident through a quartz port into the trap through a linear polarizer and quarter-wave plate, which render the beam circularly polarized (having photons of definite helicity). The polarizer reduces the incident intensity of the laser light to 15 mW.

With a reasonably clean cathode and good vacuums we should be able to generate a few hundred μA of photocurrent. Based on our experience with similar current densities from tungsten filaments, we can expect produce 10^7 cm^{-3} density plasmas from such cathodes. These densities should be adequate for the experiments we have described earlier.

Appendix B

Magnetic Pumping

B.1 Rotational Pumping

The $m = 1$ diocotron oscillations of an electron plasma have been observed to damp out due to 'rotational-pumping' in the CV trap at UCSD [38]. Due to the shape of the end-gate equipotential surfaces, the end shape of the plasma in a $m = 1$ mode is such that the plasma end radially closer to the trap gates extends further axially into the confining gate than the side of plasma closer to the trap center. As the plasma rotates about its own axis, through the self $E \times B$ rotation, the length of a fluid flux tube is modulated at this rotation frequency ω_R, which is typically much faster than the diocotron frequency ω_D, as shown in Figure B.1 Due to the longitudinal motion adiabatic invariant $J = \ell v_{\|}$, the parallel temperature of the electrons $T_{\|}$ is modulated. Since $\ell v_{\|}$ =constant $T_{\|}$ is modulated at the rotation frequency according to,

$$\frac{d}{dt} T_{\|} = -\frac{2}{\ell} \frac{d\ell}{dt} T_{\|} \tag{B.1}$$

Since the frequency of modulation is typically much faster that the collisional equilibration rate $\nu_{\perp\|}$ between $T_{\perp}$ and $T_{\|}$, the two temperatures can diverge substantially from thermal equilibrium. This leads to irreversible heating of the plasma. Since energy is conserved, the temperature rise of the plasma must be accompanied by an radial expansion of the plasma, which lowers its electrostatic potential energy. As the plasma radius expands, it must reduce its diocotron orbit radius, in order to conserve

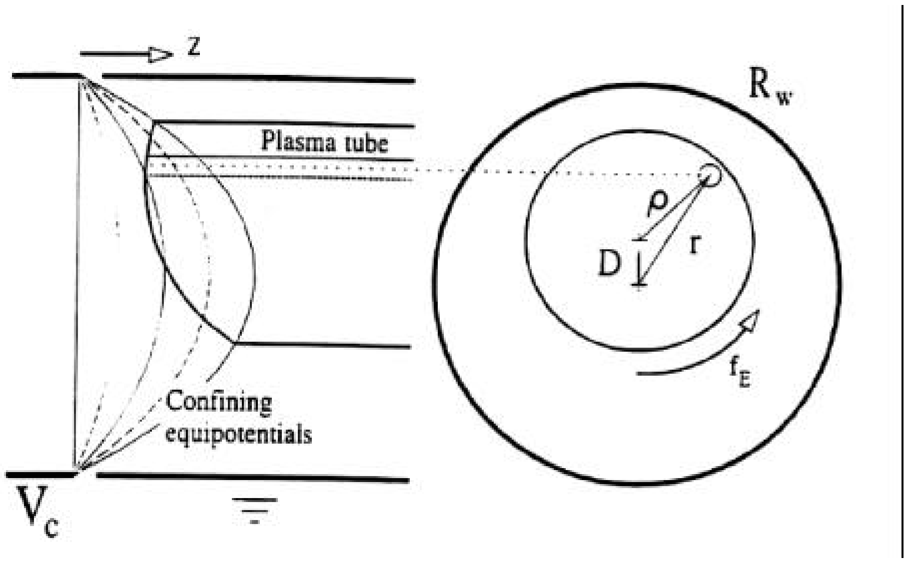

Figure B.1: Length of a plasma tube in an off-axis column is pumped by the $\mathbf{E} \times \mathbf{B}$ rotation. The curvature of the confining equipotentials makes the tube longer near the trap wall than near the trap axis. Figure reproduced from [6].

total angular momentum. Thus, this 'rotational-pumping' causes diocotron oscillations to damp out, the damping-rate being proportional to the $T_{\|} - T_{\perp}$ equilibration rate. These observations are reported in [38].

B.2 Magnetic Pumping

When a plasma undergoes a diocotron-like oscillation in a trap with a axial gradient in the magnetic field, we suggest that the analogous phenomenon of 'magnetic pumping' must also occur. When the magnetic field strength varies along the axis, the field strength at a given axial position must also vary as a function of radius. We may make an estimate of the magnitude of this variation using the Maxwell equations in the vacuum. From $\nabla \cdot \mathbf{B}$, ignoring signs, we have,

$$B_r \approx -\frac{r}{2}\frac{\partial B_z}{\partial z} \tag{B.2}$$

and from $\nabla \times \mathbf{B}$,

$$\frac{\partial B_z}{\partial r} = \frac{\partial B_r}{\partial z} \approx \frac{r}{2}\frac{\partial^2 B_z}{\partial z^2} \tag{B.3}$$

Taking $B_z \approx B$, the magnetic field magnitude, the magnitude of the fractional variation in the magnetic field with radius is

$$\frac{\delta B}{B} \approx \frac{\delta B_z}{B_z} \approx r^2 \frac{1}{B_z} \frac{\partial^2 B_z}{\partial z^2} \approx \frac{r^2}{L^2} \tag{B.4}$$

where L is the scale length of the magnetic field in the axial direction. Taking a typical value $L \approx 10cm$ and a plasma off-axis plasma with radial extent of $\approx 1cm$, gives a fractional variation of 1%.

An off-axis plasma will rotate about its own 'axis' at a faster rate than the 'diocotron oscillation' about the trap axis. If we consider the case where the axial bounce motion is slower than the rotational frequency of the plasma (this happens at low temperatures, and low magnetic fields) we may ignore the bounce motion of the electrons along the plasma length and this means that electron plasma fluid will be advected radially through regions with a slightly varying magnetic field strength. Since the magnetic moment $\mu = \frac{1}{2}m{v_\perp}^2/B$ of the electrons is an adiabatic invariant, we may expect the perpendicular temperature $k_B T_\perp =< \frac{1}{2}m{v_\perp}^2 >$, to be modulated at the frequency of the self-rotation of the plasma about its own axis ω_R.The μ invariant relates the perpendicular temperature to a changing magnetic field, leading to modulation of $T_\perp$ according to,

$$\frac{d}{dt}T_\perp = \frac{2}{B}\frac{dB}{dt}T_\perp \tag{B.5}$$

Since this frequency is typically faster than the equilibration rate $\nu_{\perp\|}$, irreversible heating must occur, as in the rotational pumping case, and the plasma expands as total energy is conserved. Since the total angular momentum must also be conserved, the plasma must move towards the axis. Although we have not made an estimate of the strength of this effect in our plasma diocotrons in axial gradient fields, it is expected to be a real effect.

B.3 The Ideal Gas Analogy

Both equations B.1 and B.5 resemble the equation relating the temperature to volume changes in an ideal gas of volume V given by $TV^{\gamma-1}$=const, where γ is the ratio of specific heats,

$$\frac{dT}{dt} = -\frac{(\gamma - 1)}{V}\frac{dV}{dt}T \tag{B.6}$$

We may then imagine the two temperatures in the plasma as an ideal gas, each confined separately, with a movable piston on one side of each compartment. The compartments are thermally insulated, but we may imagine that the wall separating the two gases is a weak conductor of heat. Then, if any one piston is moved at a rate faster than the thermal equilibration rate between the two gases, heat is transferred irreversibly between the two gases leading to heating of both the confined gases over time. This analogy may help in understanding why phenomena such as rotational pumping or 'magnetic pumping' can only lead to heating of the plasma, and can never cool it. Imagine that one complete cycle of pumping the parallel or perpendicular temperatures has led to the entire plasma being cooled by ΔT. In these pumping mechanisms only work is performed on the plasma (or performed by it). Therefore, because energy must be conserved, at the end of this cycle a net amount of work $\Delta W = \frac{3}{2}Nk\Delta T$ would be done by the plasma. Then, it appears that an amount of heat Q, which initially would have been used to heat the plasma by the amount ΔT, would have been completely converted into work. This would be a violation of the Second Law of Thermodynamics, and therefore we can assume that all such mechanisms can only cause the plasma temperature to rise. The only way to cool the plasma through a cyclic process which mechanical work is transferred to and from it is through the presence of an external low-temperature reservoir. No such heat sink is present in this scheme.

Appendix C

Feedthrough scheme for the Cryogenic Electron Trap & Dewar

This section records the feedthrough connections on the Dewar and Cryogenic Trap as of July 15, 1998.

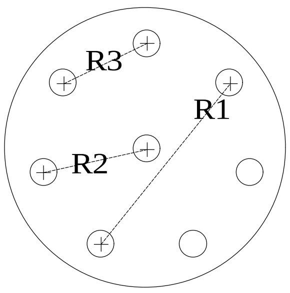

Figure C.1: Connection scheme for the dewar temperature sensor resistors: R1- LN_2 tank; R2 - LHe vapor shield and R3 - exit pt. of LHe tank. All resistances are nominally 120k- at room temperature.

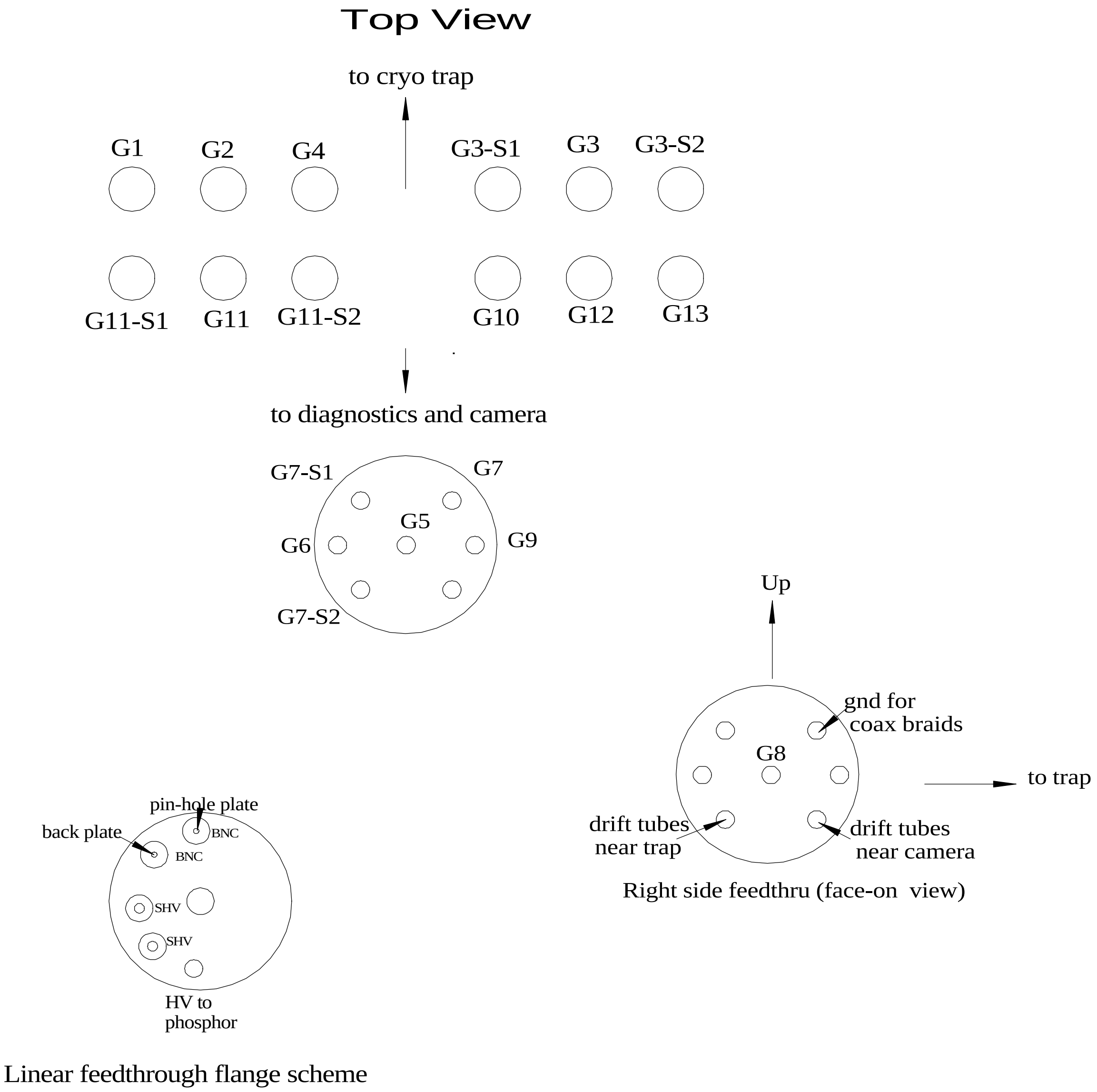

Figure C.2: Connection scheme for the trap gates and drift tubes

Bibliography

[1] B. R. Beck, J. Fajans, and J. H. Malmberg. Measurement of collisional anisotropic temperature relaxation in a strongly magnetized pure electron plasma. *Phys. Rev. Lett.*, 68:317, 1992.

[2] S. J. Chen and D. H. E. Dubin. Equilibration rate of spin temperature in a strongly magnetized pure electron plasma. *Phys. Fluids B*, 5:691, 1993.

[3] T. J. Gay and F. B. Dunning. Mott electron polarimetry. *Rev. Sci. Instrum.*, 63:1635, 1992.

[4] US Steel Technical Data Sheet for 'DC magnetization of 'ColdRolled Commercial Quality -24 Gage' Steel.

[5] M. L. Swartz, SLAC publication no. 4656, June 1988.

[6] B. P. Cluggish. *Experiments on Asymmetry-Induced Particle Transport in Magnetized, Pure Electron Plasma Columns.* PhD thesis, University of California, San Diego, 1995.

[7] R. M. Kulsrud, E. J. Valeo, and S. C. Cowley. Physics of spin-polarized plasmas. *Nuclear Fusion*, 26:1443, 1986.

[8] T. M. O'Neil. A confinement theorem for nonneutral plasmas. *Phys. Fluids*, 23:2216, 1980.

[9] R. C. Davidson, A. Drobot, and C. A. Kapetanakos. Equilibrium and stability of mirror-confined nonneutral plasmas. *Phys. Fluids*, 16:2199, 1973.

[10] C. P. Chen, R. Pakter, and R. C. Davidson. Rigid-rotor vlasov equilibrium for an intense charged-particle beam propagating through a periodic solenoidal magnetic field. *Phys. Rev. Lett.*, page 225, 1997.

[11] Francis F. Chen. *Plasma Physics and Controlled Fusion.* Plenum Press, New York, 1984.

[12] S. A. Prasad and T. M. O'Neil. Finite length equilibria of a pure electron plasma column. *Phys. Fluids*, 22:278, 1979.

[13] T. M. O'Neil and C. F. Driscoll. Transport to thermal equilibrium of a pure electorn plasma. *Phys. Fluids*, 22:266, 1979.

[14] C. F. Driscoll, J. H. Malmberg, and K. S. Fine. Observation of transport to thermal equilibrium in pure electron plasmas. *Phys. Rev. Lett.*, 60:1290, 1988.

[15] R. C. Davidson and N. A. Krall. Vlasov equilibria and stability of an electron gas. *Phys. Fluids*, 13:1543, 1970.

[16] L. D. Landau and E. M. Lifshitz. *Statistical Physics.* Addison Wesley, Reading, Mass., 1974.

[17] R. C. Davidson. *Theory of Nonneutral Plasmas.* W. A. Benjamin, Inc., Reading, Mass., 1974.

[18] J. R. Pierce. *Theory and Design of Electron Beams.* Van Nostrand, New York, 1954.

[19] A. J. Peurrung and J. Fajans. Non-neutral plasma shapes and edge profiles. *Phys. Fluids B*, 2:693, 1990.

[20] R. C. Davidson. *Physics of Nonneutral Plasmas.* Addison-Wesley, Redwood City, 1990.

[21] J. H. Malmberg and T. M. O'Neil. The pure electron plasma, liquid, and crystal. *Phys. Rev. Lett.*, 39:1333, 1977.

[22] J. S. deGrassie and J. H. Malmberg. Waves and transport in the pure electron plasma. *Phys. Fluids*, 23:60, 1980.

[23] A. J. Peurrung. *Imaging of Instabilities in a Pure Electron Plasma.* PhD thesis, University of California, Berkeley, 1992.

[24] C. F. Driscoll, K. S. Fine, and J. H. Malmberg. Reduction of radial losses in a pure electron plasma. *Phys. Fluids*, 29:2015, 1986.

[25] X. P. Huang, K. S. Fine, and C. F. Driscoll. Steady-state confinement of non-neutral plasmas by rotating electric fields. *Phys. Rev. Lett.*, 78:875, 1997.

[26] A. W. Hyatt. *Measurement of the Anisotropic Temperature Relaxation Rate in a Magnetized Pure Electron Plasma.* PhD thesis, University of California, San Diego, 1988.

[27] R. B. Scott. *Cryogenic Engineering.* Van Nostrand, Princeton, N. J., 1959.

[28] D. S. Hall and G. Gabrielse. Electron cooling of protons in a nesting penning trap. *Phys. Rev. Lett.*, 77:1962, 1996.

[29] B. R. Beck. *Measurement of the Magnetic and Temperature Dependence of the Electron-Electron Anisotropic Temperature Relaxation Rate.* PhD thesis, University of California, San Diego, 1990.

[30] F. S. Pobell. *Matter and methods at low temperatures, 2 ed.* Springer Verlag, New York, 1996.

[31] R. A. Haefer. *Cryopumping: theory and practice.* Oxford University Press, New York, 1989.

[32] A.J. Peurrung and J. Fajans. Experimental dynamics of 2-d vorticity rings. In *1992 International Conference on Plasma Physics*, pages III–1899. European Physical Society, 1992.

[33] Grant W. Hart. The effect of a tilted magnetic field on the equilibrium of a pure electron plasma. *Phys. Fluids B*, 3:2987, 1991.

[34] F. Anderegg, X. P. Huang, E. Sarid, and C. F. Driscoll. New pure ion plasma device with laser induced fluorescence diagnostic. *Rev. Sci. Instrum.*, 68:2367, 1997.

[35] G. W. Hart, Brigham Young University, Utah, private communication.

[36] K. S. Fine. *Experiments with the l=1 Diocotron Mode.* PhD thesis, University of California, San Diego, 1988.

[37] K. S. Fine and C. F. Driscoll. The finite length diocotron mode. *Phys. Plasmas*, 5:601, 1998.

[38] B. P. Cluggish and C. F. Driscoll. Transport and damping from rotational pumping in magnetized electron plasma. *Phys. Rev. Lett.*, 74:4213, 1995.

[39] T. M. O'Neil. Cooling of a pure electron plasma by cyclotron radiation. *Phys. Fluids*, 23:725, 1980.

[40] T. M. O'Neil. Collision operator for a strongly magnetized pure electron plasma. *Phys. Fluids*, 26:2128, 1983.

[41] T. M. O'Neil and P. G. Hjorth. Collisional dynamics of a strongly magnetized pure electron plasma. *Phys. Fluids*, 28:3241, 1985.

[42] M. E. Glinsky, T. M. O'Neil, M. N. Rosenbluth, K. Tsuruta, and S. Ichimaru. Collisional equipartition rate for a magnetized pure electron plasma. *Phys. Fluids B*, 4:1156, 1992.

[43] C. M. Surko, R. G. Greaves, and M. Charlton. Stored positrons for antihydrogen production. *Hyperfine Interactions*, 109:181, 1997.

[44] A. Rich, J. Van House, D. W. Gidley, R. S. Conti, and P. W. Zitzewitz. Spin-polarized low-energy positron beams and their applications. *Applied Physics A*, 43:275, 1987.

[45] T. E. Cowan, B. R. Beck, J.H. Hartley, R. H. Howell, R. R. Rohatgi, J. Fajans, and R. Gopalan. Development of a pure cryogenic positron plasma using a linac positron source. *Hyperfine Interactions*, 172:1, 1993.

[46] F. C. Michel. Theory of pulsar magnetospheres. *Rev. Modern Phys.*, 54:1, 1982.

[47] Robert Lin, U. C. Berkeley, private communication.

[48] L. H. Haarsma, K. Abdullah, and G. Gabrielse. Extremely cold positrons accumulated electronically in ultrahigh vacuum. *Phys. Rev. Lett.*, 75:806, 1995.

[49] Greg Mulhollan, SLAC, private communication.

[50] F. B. Dunning. Mott electron polarimetry. *Nucl. Instrum. and Methods A*, 347:152, 1994.

[51] J. Kessler. *Polarized Electrons 2nd ed.* Springer, Berlin, 1985.

[52] T. Rikitake. *Magnetic & Electromagnetic Shielding.* D. Reidel, Boston, 1987.

[53] D. T. Pierce, R. J. Celotta, G. C. Wang, W. N. Unertl, A. Galejs, C. E. Kuyatt, and S. R. Mielczarek. Gaas spin polarized electron source. *Rev. Sci. Instrum.*, 51:478, 1980.

[54] R. Alley et al. The stanford linear accelerator polarized electron source. *Nucl. Instrum. and Methods A*, 365:1, 1995.

[55] D. T. Pierce, NIST, Gaithersburg, private communication.

[56] Phillip Kirkeby, Advanced Vacuum Technology, Mountain View, CA, private communication.